STUDY OF THE CHEMICAL FABRICATION PROCESS OF NSOM PROBES AND THE MODIFICATION OF THE PROBE SURFACE

by

Muhammad Nazmul Hussain

A Dissertation Submitted in

Partial Fulfillment of the

Requirements for the Degree of

Doctor of Philosophy

in Chemistry

at

The University of Wisconsin-Milwaukee

May 2022

ABSTRACT

STUDY OF THE CHEMICAL FABRICATION PROCESS OF NSOM PROBES AND THE MODIFICATION OF THE PROBE SURFACE

by

Muhammad Nazmul Hussain

The University of Wisconsin-Milwaukee, 2022
Under the Supervision of Professor Jörg C. Woehl

Near-field scanning optical microscopy (NSOM) merges scanning probe technology with the power of high-resolution optical microscopy and provides a natural view into the nanoworld. NSOM requires tapered probes with subwavelength optical apertures and wide cone angles to efficiently channel the illumination light to the tip apex so that it can acquire optical images beyond the diffraction limit. Tapered probes with a range of cone angles can be fabricated through chemical etching of optical fibers using hydrofluoric acid (HF) by varying the etching time. Apart from their use for NSOM imaging, such optical probes can also be transformed into nanosensors by attaching sensing elements to the NSOM probe surface.

This work seeks to identify the maximum obtainable cone angle in an NSOM probe fabricated by chemical etching of an optical fiber and to create a nanosensor using this kind of probe. We investigate the progression of cone angles with etching time and

propose a model of the etching process. We find that the variation of cone angle as a function of etching time does not follow the expected exponential plateau curve and we compare the experimental result to simulations with multiphysics models of the etching process of an optical fiber. Additionally, functionalization of NSOM probes with different fluorescent molecules is investigated and a fluorescent nanosensor is developed. We observe that the nanosensor is able to detect concentration changes of Cu^{2+} and Fe^{3+} ions in a droplet of sample solution.

This thesis is dedicated to my parents who nurtured the thirst for knowledge in me,

to my wife who supported me during the difficult times,

and

especially to my beautiful daughter, a little angelic princess, who has a radiant smile and an infectious laughter that turns despair into inspiration and brings joy to the heart.

TABLE OF CONTENTS

LIST OF FIGURES

LIST OF TABLES

LIST OF ABBREVIATIONS

NSOM	near-field scanning optical microscopy
HF	hydrofluoric acid
FSNC	fluid-solid non-catalytic
PCM	progressive conversion model
SCM	shrinking core model
L-W	Lucas-Washburn
MeOH	methanol
EtOH	ethanol
APTES	(3-aminopropyl)triethoxysilane
FITC	fluorescein 5-isothiocyanate
EDC	1-ethyl-3-(3-dimethylaminopropyl)carbodiimide
DMAP	4-dimethylaminopyridine
DCM	dichloromethane
RO	reverse-osmosis
SEM	scanning electron microscopy
MST	modified sealed-tube
PDE	partial differential equation
TDS	transport of diluted species

DG	deformed geometry
DL	Darcy’s law
PCF	photonic crystal fiber
UV	ultra-violet
IR	infra-red
NA	numerical aperture
EMCCD	electron multiplying charge coupled device
FEM	finite element method
LF	laminar flow
PTPM	phase transport in the porous media
AFM	atomic force microscopy
SNOM	scanning near-field optical microscopy
TF	tuning fork
SPM	shrinking particle model

LIST OF SYMBOLS

λ	wavelength
k	wavevector
ω	angular frequency
c	speed of light
n_{core}	refractive index of optical fiber core
n_{clad}	refractive index of optical fiber cladding
θ_c	critical angle
θ_{acc}	acceptance angle of optical fiber
R	etch rate of SiO_2
k	reaction rate constant
R_c or r	capillary tube radius
p_c	capillary pressure
γ or σ	surface tension
$h(t)$	liquid imbibition height
μ	viscosity
a	diameter of a subwavelength hole
ε_{alu}	dielectric constant of aluminum
ε_{core}	dielectric constant of optical fiber core

α	cone angle of tapered probe
$\mathbf{J}$	flux
c	HF concentration
D	diffusion coefficient
$\mathbf{u}$	fluid velocity
k	etching rate constant
ρ	fluid density
p	fluid pressure
v_{n}	normal mesh velocity
R_{s}	etching rate at the optical fiber interface
$\mathrm{K_D}$	diffusion model constant
$\mathrm{n_F}$	number of HF molecules consumed per SiO_2 unit
ε_{p}	porosity
κ	permeability

ACKNOWLEDGEMENTS

Foremost, I would like to express my sincere gratitude to my research advisor Dr. Jörg Woehl for his continuous support of my PhD studies and research. Thank you so much for guiding and advising me with my research, thesis writing, and future career. I would not have made it through the hard times in research and in life if you had not been exceptionally patient and considerate with me, so I give my heartfelt thanks to you. Thank you for believing in me, in my work, and in my ideas, and treating me as a colleague. I could not have asked for a better mentor than you, so I thank you.

Besides my advisor, I would like to thank the rest of my thesis committee: Dr. Mark Dietz, Dr. Arsenio Andrew Pacheco, Dr. Heather Owen, and Dr. Paul Henning, for their insightful comments, hard questions, and encouragement. Thank you, Dr. Owen, for your guidance and help with the use of Scanning Electron Microscope.

I would like to thank Michael Condon, Instrument Maker for L&S Instrument Shop, for his cordial support and willingness to make challenging tools according to my project's requirements. I wish to thank departmental glassblower Neal Korfhage for his innovative custom-made glass tools. I thank my fellow group members, both current and former, who I had the pleasure of working with. Thank you, Quintus Owen, for providing new perspective with your novel ideas. Thank you, Dr. Xavier Udad, for assisting me repeatedly with my project work. And thank you, Dr. Bradley Moran, for demonstrating one of the initial projects.

And my biggest thanks to my family for all the support you have shown me through this research. For my wife, thank you for your moral support and delicious meals, without which I would have stopped these studies a long time ago.

CHAPTER 1

Introduction

1.1 Objectives and Organization

Analytical chemistry has become indispensable in many fields such as forensic analysis, clinical research, biological analysis, environmental investigation, material study, etc., with the help of advanced technologies and new techniques. However, the currently available analytical techniques have at least one of the following characteristics:

1. only *in vitro* analysis possible,
2. invasive in nature,
3. destructive to the sample,
4. global analysis,
5. local analysis in a non-selective way.

Near-field scanning optical microscopy (NSOM) is a new microscopy technique for nanoscale imaging that combines scanning probe technology with high-resolution optical microscopy. The probe used in NSOM resembles microinjection needles that inject genetic material into the cell's nucleus (Figure 1.1). Therefore, an analytical method using NSOM has the potential to be non-destructive, localized, selective, have pinpoint accuracy, and could be used *in situ* or even, possibly, *in vivo*.

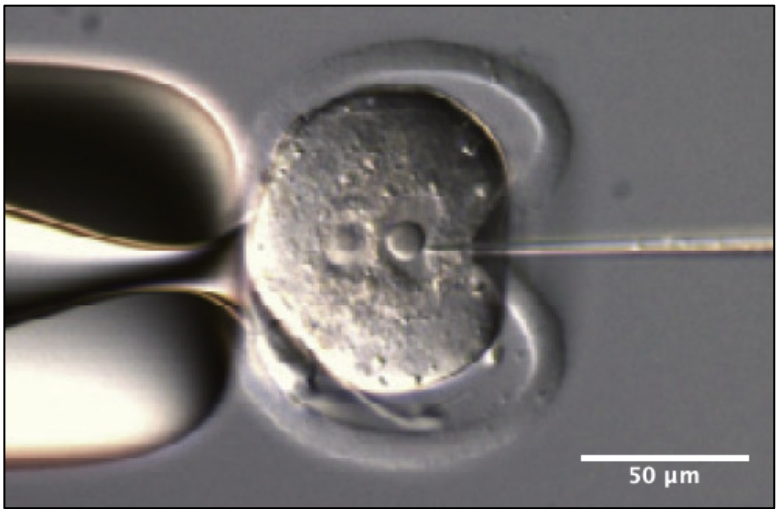

(a)

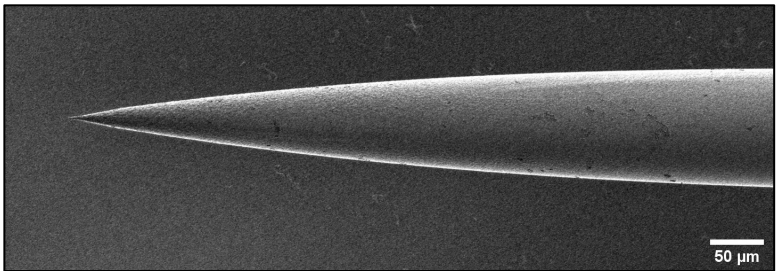

(b)

Figure 1.1: (a) Snapshot optical image taken by Abe of injecting genetic material into the cell's nucleus using a microinjection needle. Adapted from Ref. 1. (b) Scanning Electron Microscopy (SEM) image of an NSOM probe.

We embarked on this research project to develop an analytical method using NSOM because we had both the NSOM system as well as the operational expertise in NSOM. The framework of this thesis is based on the following three main objectives:

1. To determine the cone angle of the near-field scanning optical microscopy (NSOM) probe during the chemical fabrication process by conducting a time-dependent study.

2. To develop a multiphysics simulation model for the chemical fabrication process of the NSOM probes.
3. To develop fluorescence nanosensors based on NSOM probes for *in situ* sensing applications.

This manuscript has been organized in such a fashion that illustrates the works completed in this research in the same order as the objectives listed above. Chapter 1 gives a brief introduction to the core theoretical concepts and historical background of the topics related to this work including NSOM and optical sensors, so that the readers can have a good understanding of the basics of the subject matter before delving into more in-depth analyses in the later chapters. Thereafter, Chapter 2 provides a literature review of the following theories relevant to this research: wet etching of silica, wicking in porous media and non-catalytic solid-fluid reaction. A description of the experimental materials and methods including instruments, setups, and procedures used for this work is detailed in Chapter 3.

The four subsequent chapters each start with a theoretical explanation followed by experimental results and discussions. Chapter 4 illustrates NSOM, NSOM probe fabrication and the time-dependent study of the fabrication process. Chapter 5 explains the physics and chemistry involved in the NSOM probe fabrication process and develops a multiphysics simulation model. Chapter 6 demonstrates the development of *in situ* fluorescent nano sensors using NSOM probes. Chapter 7 offers conclusions and the future directions of this work to wrap up the manuscript.

1.2 Overview

This introductory chapter starts with the historical background of classical optical microscopy and its limitations. After this, it discusses the gradual and decades long development of NSOM theory and technology. Then, a brief description of NSOM design and its working principle is given. This includes operational modes of NSOM, optical fibers and their use as probes, and the fabrication of NSOM probes. Lastly, sensors and different types of sensors such as chemical, optical, and fluorescent sensors are discussed at the end of this chapter.

1.3 Optical Microscopy

Microscopy is the study of tiny things using microscopes. The term “microscope”, coined by Giovanni Faber in 1625, is derived from the Greek words “mikrós” meaning “small” and “skopeîn” meaning “see”.[2,3] Development of modern microscopes can be attributed to the discovery of the lens. Although 4th century B.C. comedy writer Aristophenes described in a passage that globules of glass called “burning spheres” were sold in Athens, the unearthed plano-convex rock crystal called the “Nimrud lens” (Figure 1.2(a)) is the oldest known lens dating back to 700 B.C. that still exists.[4] It was Seneca who was first to describe that a globe of water can be used for magnification. In the 1st century A.D. Seneca discovered that small and dim letters looked large and distinct if looked through a clear spherical flask filled with clear water.[4,5] In 1011-21 A.D. Arabian scholar Abu Ali Al-Hasan Ibn al-Haytham (famously known by his Latinized name *Alhazen*) wrote the “Book of Optics” where he described the anatomy of the eye and how

the lens focuses images.[4,6] Clear mineral spheres had been used for eyeglasses until silicate glass was produced in Italy in the late 1200s.[5] It is believed that around 1595, the Janssens made the first compound optical microscope by placing multiple lenses in a tube (Figure 1.2(b)).

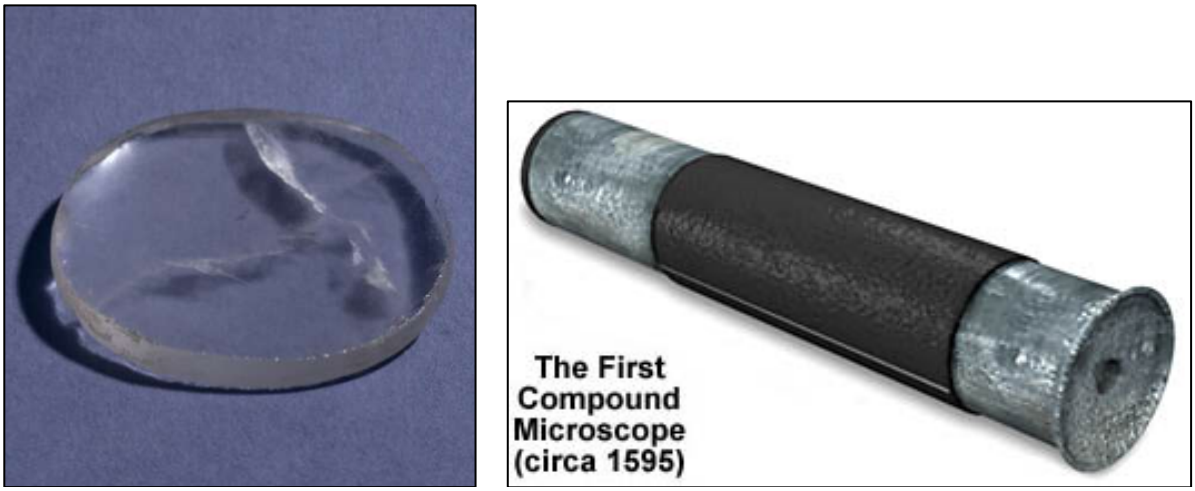

(a) **(b)**

Figure 1.2: (a) Nimrud lens. Reprinted from Ref. 7. (b) First compound microscope made by the Janssens. Reprinted from Ref. 8.

1.3.1 Classical Microscopy

The working medium in classical microscopy is visible light, so these instruments are also known as light microscopes. In modern days, the conventional compound light microscopes used in research usually have either an upright design (Figure 1.3(a)) or an inverted design (Figure 1.3(b)) with a lamp that emits visible light. They use a set of lenses to project a magnified image of an object onto the retina of the eye or onto the image sensor of the camera.[9]

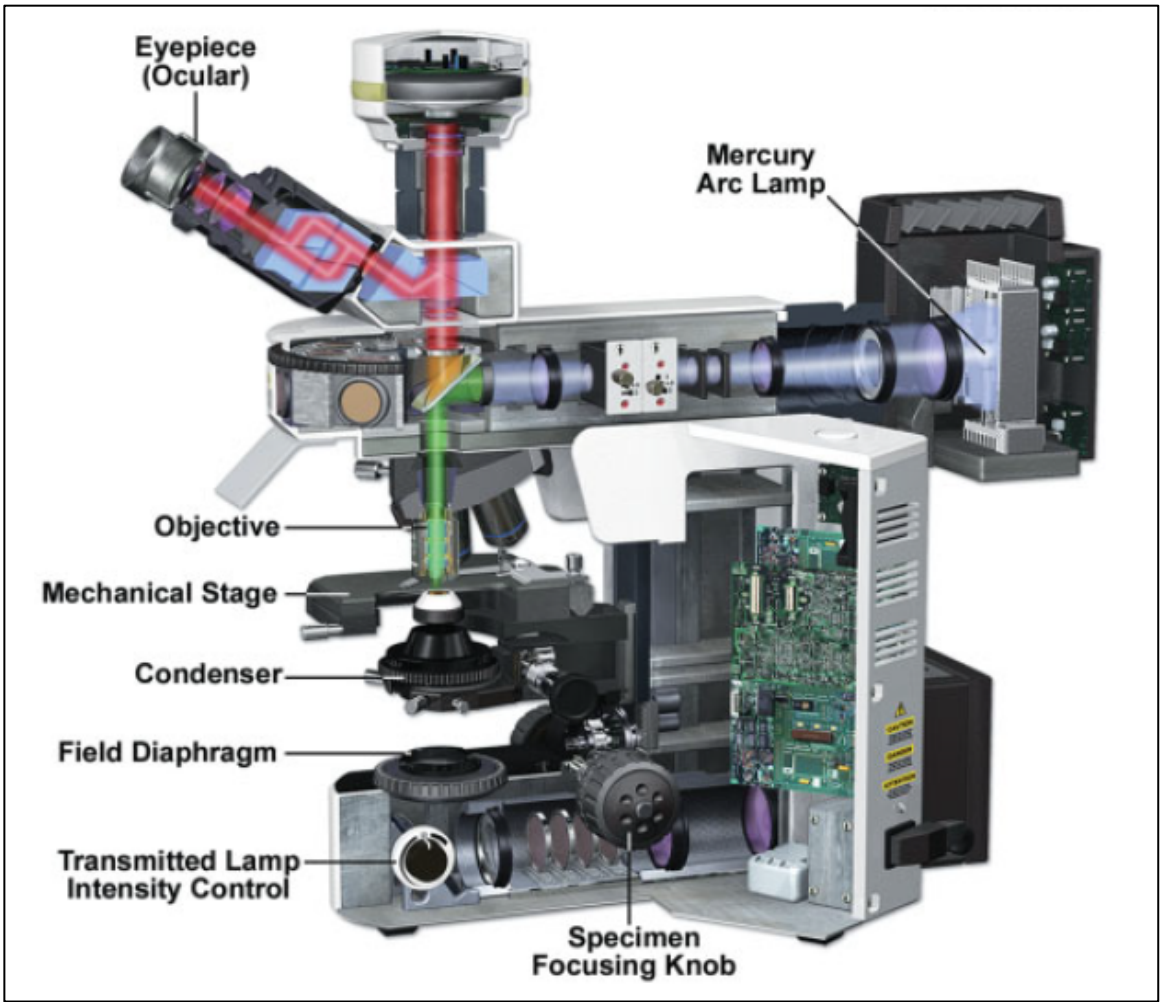
Eyepiece
(Ocular)
Mercury
Arc Lamp
Objective
Mechanical Stage
Condenser
Field Diaphragm
Transmitted Lamp
Intensity Control
Specimen
Focusing Knob

(a)

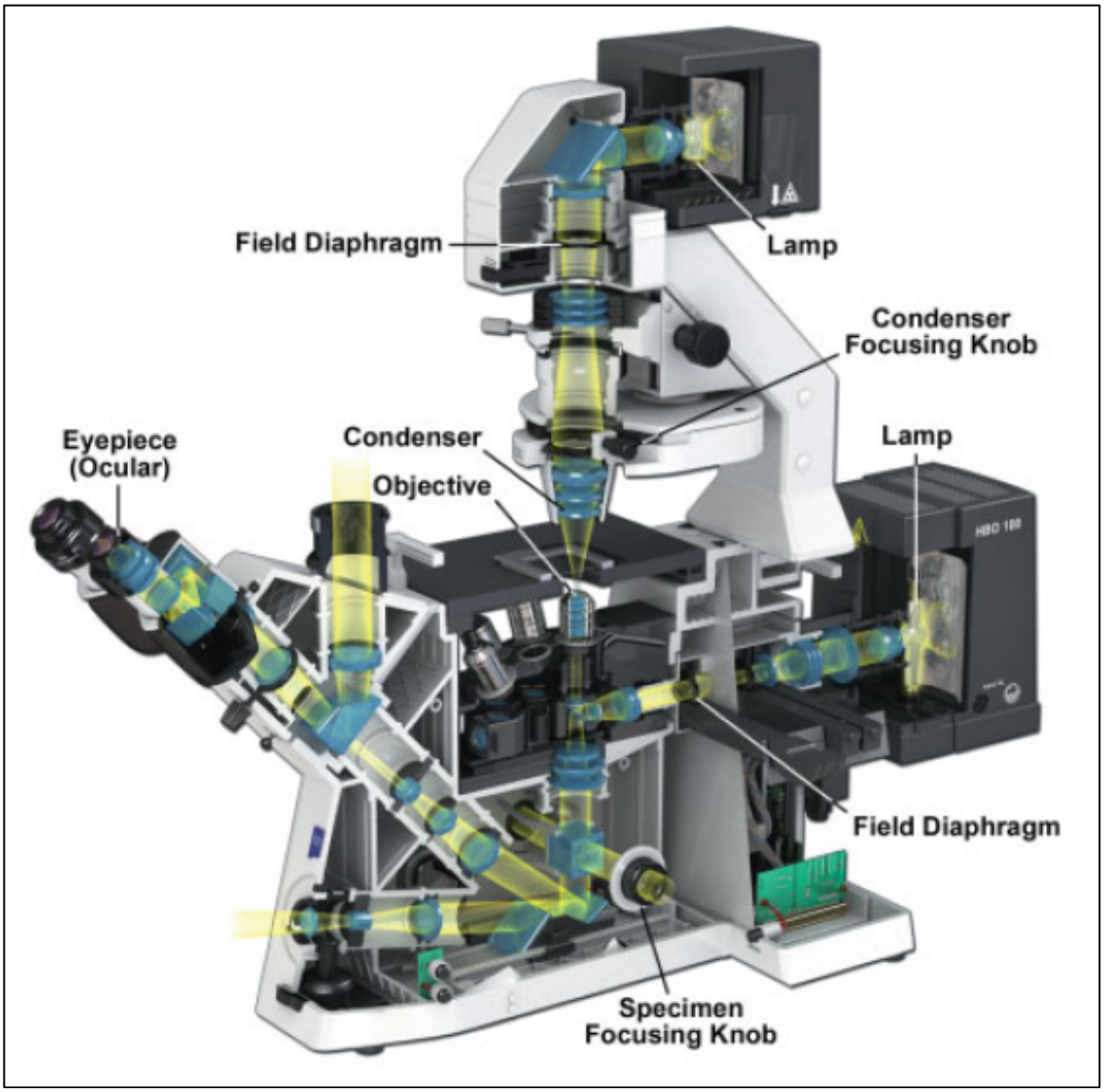

(b)

Figure 1.3: Modern compound light microscopes used in research (a) upright design and (b) inverted design illustrated by Murphy and Davidson. Adapted with permission from Ref. 9. Copyright 2013 Wiley-Blackwell.

An inverted light microscope has been used for the research work done in this thesis. To a viewer looking through the eyepiece of a compound microscope, the final magnification depends on the magnification of the lenses on the objective and on the eyepiece (or ocular) (Figure 1.4), but forming of a clear image depends on the objective

and the condenser that focuses the illumination light onto the specimen. The distance between the lens and the object in a compound microscope is greater than several wavelengths of the illuminating light; thus, the term “far-field” is also used for classical microscopy.

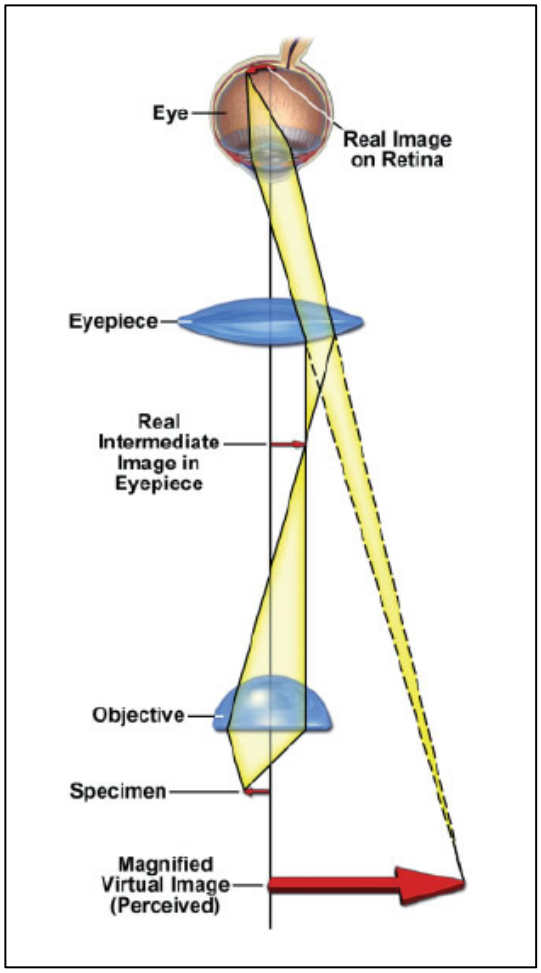

Figure 1.4: Schematic of an object being magnified in the microscope perceived by an observer illustrated by Murphy and Davidson. Adapted with permission from Ref. 9. Copyright 2013 Wiley-Blackwell.

1.3.2 Limitations

Although the discovery of the lens led to the invention of microscopes, there are inherent limitations with its use. When the freely propagating light wave from a point source passes through the (finite) circular aperture of a lens, the light gets diffracted and forms an image at the focal plane of the focusing lens with a bright circular region in the center surrounded by a series of concentric rings of decreasing intensity (called the "Airy disk") instead of forming a point image (Figure 1.5(a)). Both the Abbe criterion (diffraction of lines) described by the German physicist Ernst Abbe in 1873 and the Rayleigh criterion (diffraction of point objects) (Figure 1.5(b)) described by the English physicist Lord Rayleigh in 1896 define the resolution limit of optical imaging instruments such as microscopes and telescopes.[10,11] The resolving power of a microscope is limited by the wavelength (λ) of the illuminating light and the numerical aperture (the sine of half the angle subtended by the aperture at an object point times the index of refraction of the medium between the object and the objective lens) of the lens, and the minimum resolvable distance (Δx) between two point objects is given by the Equation 1.1.

$$\Delta x = 0.61 \frac{\lambda}{\mathrm{NA}} \qquad (1.1)$$

The numerical aperture (NA) can be as high 1.3-1.4 for modern objectives working in high-index mediums such as water or oil, and so Equation 1.1 is usually simplified to $\Delta x = \lambda/2$. Therefore, the maximal resolution is then approximately equal to half the wavelength of the radiation used, which for visible light applications results in a spatial resolution of $200 - 300\ \mathrm{nm}$.[12]

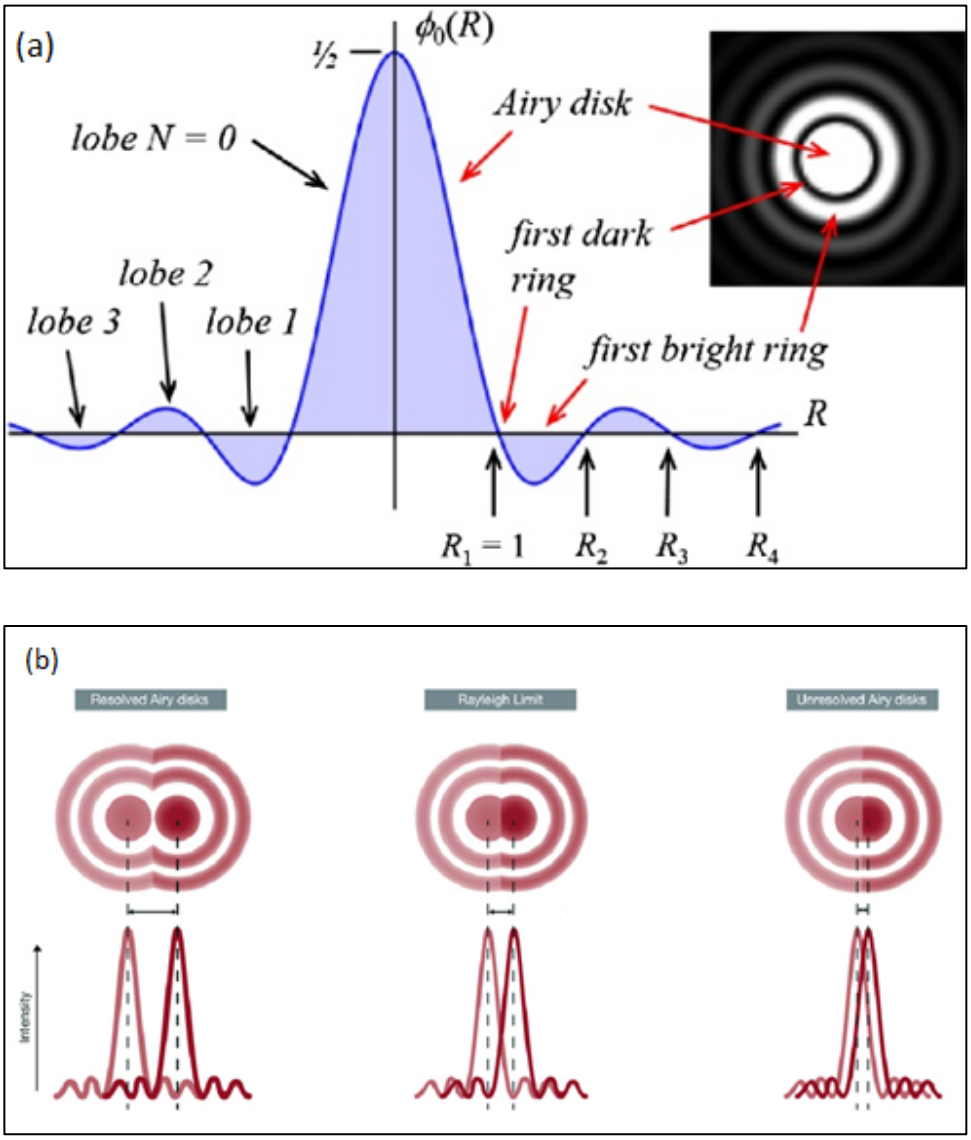

Figure 1.5: (a) Airy disk illustrated by Gris-Sánchez et al. Reprinted from Ref. 13. (b) Schematic representation of the resolving power of a microscope illustrated by Dunst and Tomancak. Adapted with permission from Ref. 11. Copyright 2019 Oxford University Press.

1.4 Near-field Scanning Optical Microscopy

Near-field scanning optical microscopy (NSOM) is also known as SNOM (scanning near-field optical microscopy) because two different researchers independently developed the same near-field optics technology at about the same time.[14] Near-field optics can be explained from the dispersion relation of freely propagating light. The propagation of light in free space is determined by the dispersion relation:

$$k^2 = k_x^2 + k_y^2 + k_z^2 = \frac{\omega^2}{c^2} \qquad (1.2)$$

where k is the wavevector, ω is the angular frequency and c is the speed of light. Positive values of the Fourier component ($e^{ik_z z}$) of the wavevector results in radiative (or propagative) waves along z reaching the far-field. On the other hand, negative values ($e^{-|k_z|z}$) result in non-radiative *evanescent waves* in the near-field zone that decay exponentially, preventing these waves from reaching the far-field.[15,16]

1.4.1 Historical Background

The idea of NSOM was first proposed by the Irish scientist E.H. Synge in a paper in 1928. Synge proposed that to overcome the diffraction limit, the particles need to be illuminated through an aperture of subwavelength diameter created on a thin opaque metal screen placed at the subwavelength distance from the particles (Figure 1.6).[12,17,18] He also came up with another way of creating subwavelength apertures which later

became the most common standard for producing aperture NSOM probes, and wrote to Einstein in a letter:

> *A better way could be, if one could construct a little cone or pyramid of quartz glass having its point P brought to a sharpness of order 10^{-6} cm. One could then coat the sides and point with some suitable metal (e.g., in a vacuum tube) and then remove the metal from the point, until P was just exposed. I do not think such a thing would be beyond the capacities of a clever experimentalist*.[19]

His proposal could not be demonstrated experimentally because at that time the technology was not available to create a subwavelength aperture. More than 50 years later, after optical fibers and the scanning tunneling microscope had already been invented, Pohl's laboratory at IBM and Lewis's laboratory at Cornell University independently developed the NSOM technology in 1984. Pohl used the term "SNOM" for this technology whereas Lewis coined it "NSOM" in their respective published articles.[14]

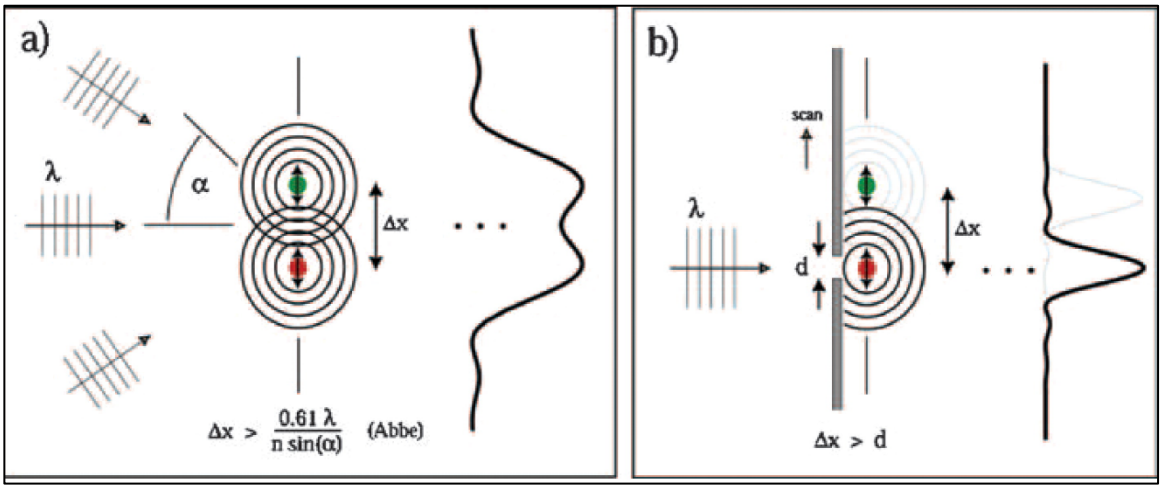

Figure 1.6: Schematic representation of (a) two spots that are not resolved by far-field microscopy due to the diffraction limit, but that (b) can be resolved with aperture near-field microscopy illustrated by Novotny and Stranick. Reprinted with permission from Ref. 17. Copyright 2006 Annual Reviews.

1.4.2 Aperture NSOM

The primary components of an NSOM setup (Figure 1.7) are the light source (lasers), the probe (also called the scanning tip), the detector, and the feedback mechanism. The probe and the feedback mechanism are the most critical parts of the NSOM setup. Based on the type of probe used, NSOM can be divided into two main categories: aperture NSOM and apertureless NSOM.

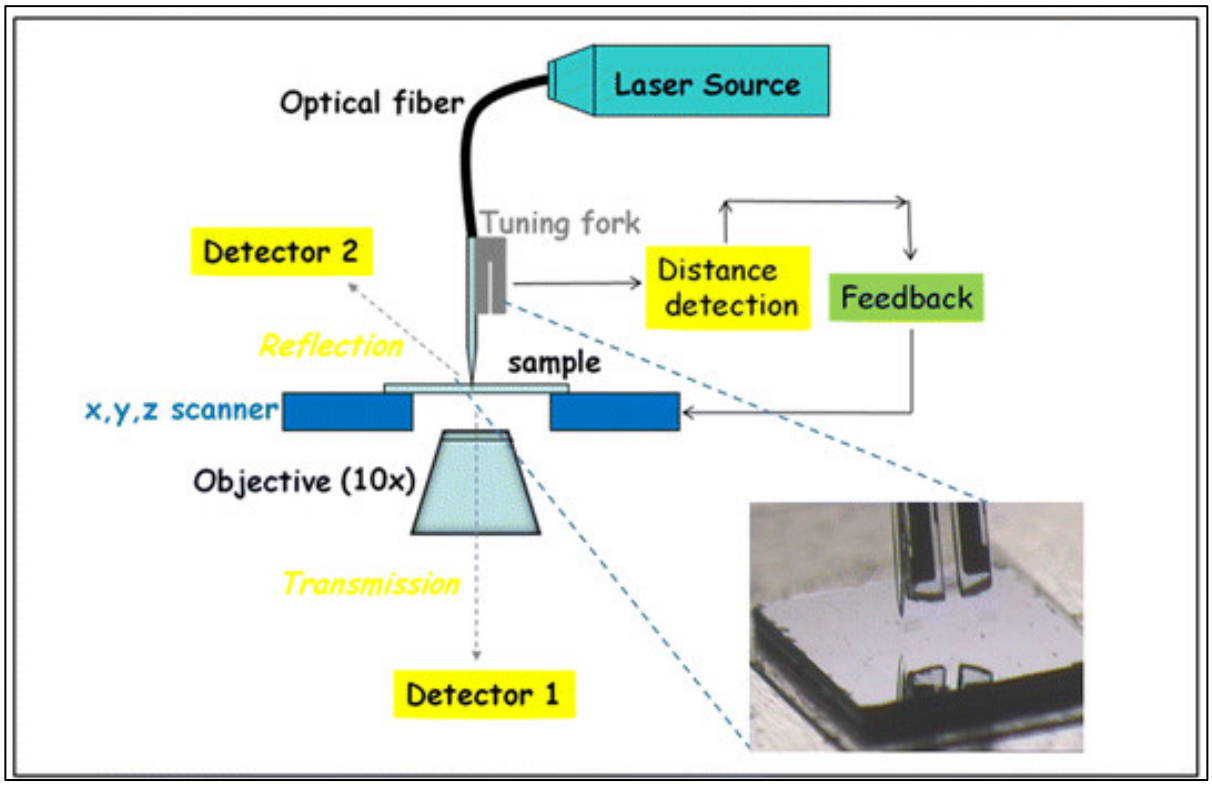

Figure 1.7: Schematic representation of NSOM setup illustrated by Andolfi et al. Adapted from Ref. 20.

In the aperture NSOM design, the probe is either an aluminum-coated tapered glass tip or an atomic force microscopy (AFM) cantilever with an aperture hole. On the other hand, the apertureless NSOM design uses a very sharp dielectric or metallic tip as the probe

(Figure 1.8).[21] This thesis only focuses on the configuration, the modification, and the application for imaging and sensing of the aperture-type NSOM.

A tapered single-mode optical fiber, which has 1000 times higher collection and transmission efficiencies than an etched quartz crystal or pulled micropipette, has become the standard for creating probes for aperture NSOM.[3,12]

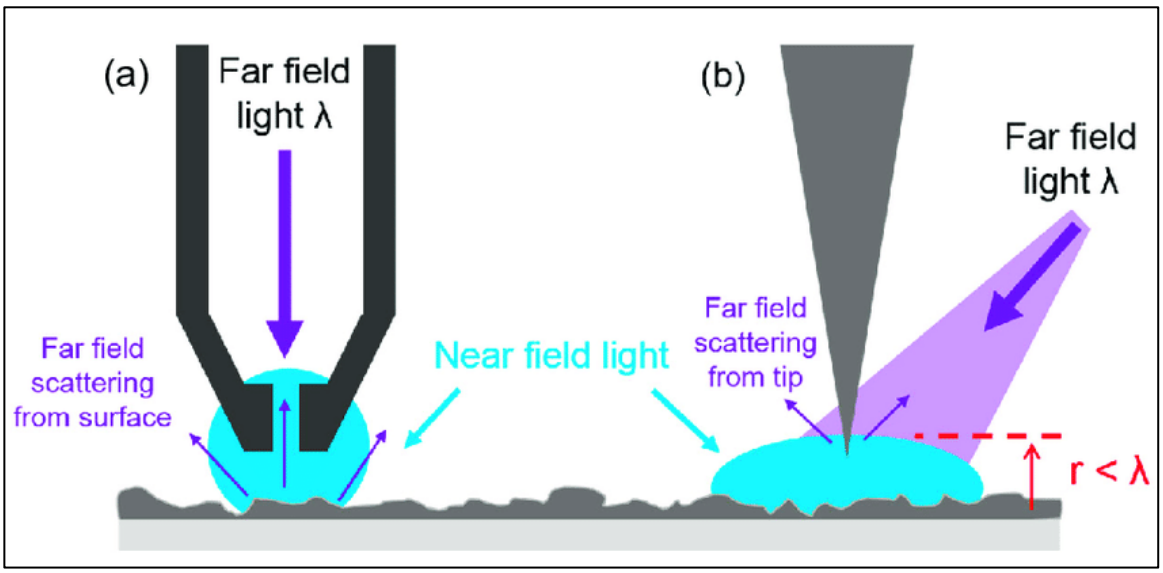

Figure 1.8: Schematic representation of NSOM probes (a) aperture (b) apertureless illustrated by Bazylewski et al. Adapted from Ref. 22.

The aperture at the apex of the tapered single-mode optical fiber is created by coating the sides of the tapered fiber with an opaque metal such as aluminum. Metal coating prevents leaking of the light from the sides at the apex of the probe and helps to form a well-defined aperture.

The aperture NSOM can have five different operational modes depending on how the sample is illuminated and how the scattered light is collected or detected. As shown in Figure 1.9, the first two operational modes, Illumination and Collection, require a

transparent sample whereas the last three modes, namely Reflection, Reflection Collection, and Illumination Collection, do not require a transparent sample. In the Illumination mode, the sample is illuminated through the probe and scattered light is collected by objective lens from underneath the sample. The Collection mode is the opposite of the Illumination mode – the sample is illuminated by far-field light from underneath sample and scattered light is collected by the probe.

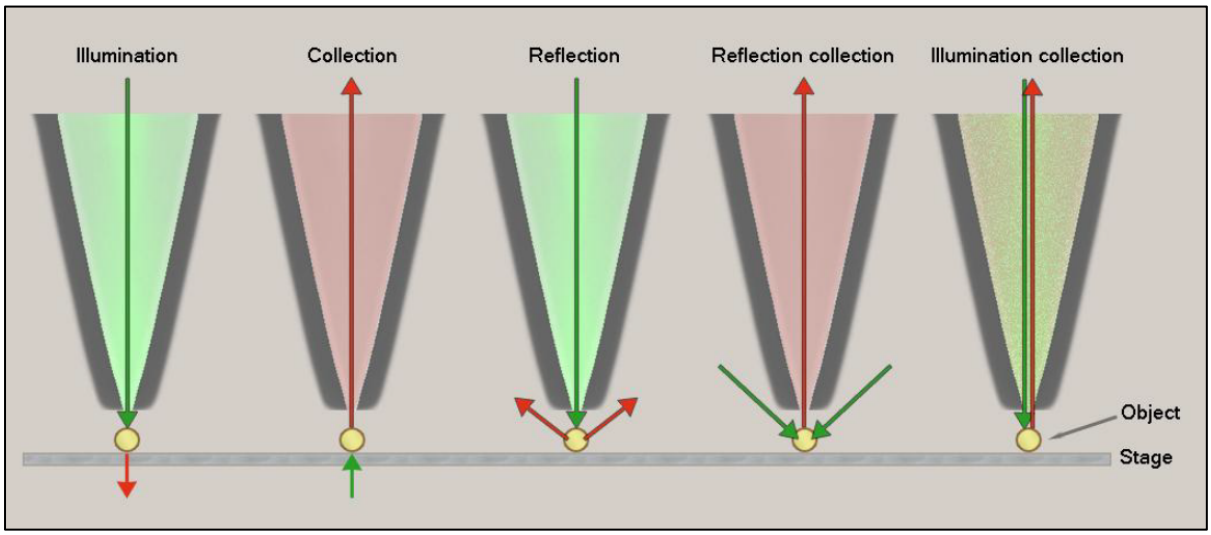

Figure 1.9: Schematic representation of NSOM operational modes illustrated by Ababneh. Reprinted from Ref. 3.

The Reflection mode illuminates the sample through the probe as in the Illumination mode, but the reflected light from the sample is collected from the side because the sample is opaque. When the illumination of sample and collection of scattered light is reversed compared to the Reflection mode, it is referred to as the Reflection Collection mode. The Illumination Collection mode both illuminates the sample and collects the scattered light from the sample through the probe. Only this operational mode requires

probes made from multimode optical fiber, which can transmit a range of wavelengths, whereas all other operational modes can use probes made from single mode optical fiber.

NSOM requires not only a subwavelength aperture at the apex of the probe for high resolution imaging, but the apex of the probe also needs to be held at a subwavelength distance from the sample. When an NSOM probe is fixed on a Z-piezoelectric scanner combined with a stepper motor, the scanning tip can be brought to within a few nanometers from the sample surface. If the sample is mounted on a separate XY-piezoelectric scanner, the sample can be raster scanned by moving the sample in X and Y directions while keeping the NSOM probe fixed as shown in Figure 1.6. To avoid the scanning tip being damaged during the initial approach or during raster scanning of the sample surface, the Z-piezoelectric scanner is controlled by an electronic feedback system based on shear-force detection using a quartz crystal tuning fork (TF). The NSOM probe is firmly glued along the side of one of the prongs (Figure 1.10) of a commercially available quartz crystal tuning fork having resonance frequency of $32{,}768\ \mathrm{Hz}$.

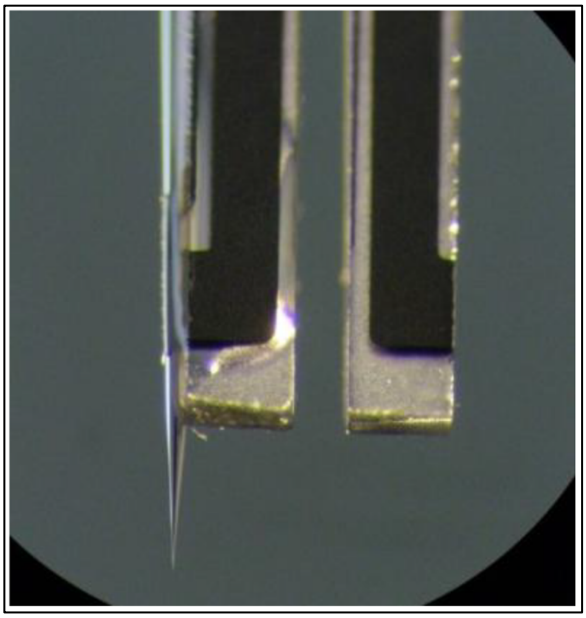

Figure 1.10: Optical image of NSOM probe glued to tuning fork taken by Ababneh. Reprinted from Ref. 3.

When the fork is mechanically excited by a piezoelectric dither to its resonance frequency (at which the bending amplitude of the prongs is maximum), it causes the fork and the tip to vibrate parallel to the sample surface. When the approaching tip comes within tens of nanometers of the sample surface, the tuning fork signal amplitude starts to reduce significantly because of a dampening of the tip oscillation by shear-force interaction with the surface. An electronic feedback system gathers the damping signal and uses it to keep a constant distance between the tip and the sample surface for topographic mapping (Figure 1.11).[3,23–26]

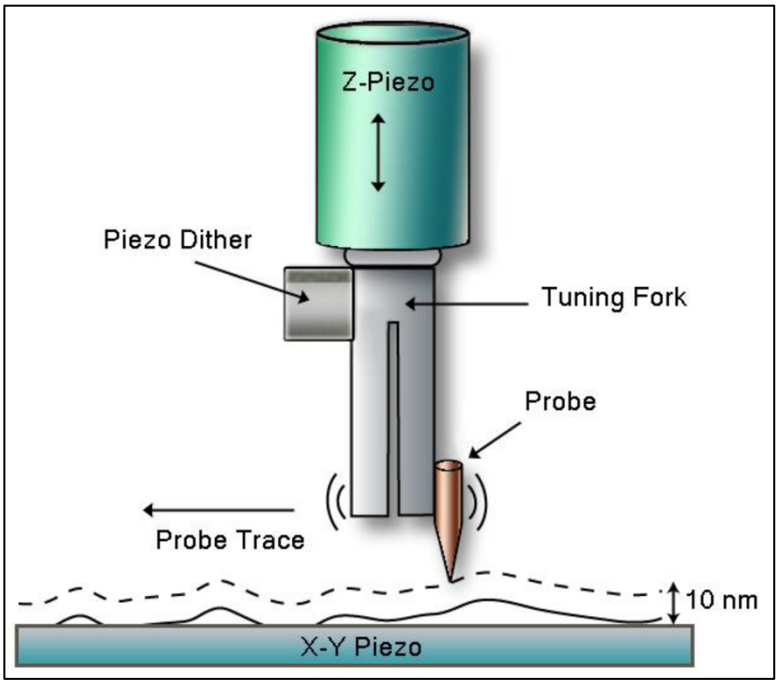

Figure 1.11: Schematic representation of raster scanning of a sample with NSOM probe illustrated by Ababneh. Reprinted from Ref. 3.

1.4.3 Optical Fiber NSOM Probes

Optical fiber has several advantages over other materials, making it the best candidate for fabricating NSOM Probes. These include guiding light with low loss, flexibility, immunity to electromagnetic interference, and affordability.[27] Single-mode optical fibers that are used for fabricating NSOM probes usually have three layers: the core, the cladding, and the polymer jacket. Light is guided through the core which is the innermost part of the optical fiber with a typical diameter of 3-9 μm. The cladding, which surrounds the core and brings the diameter of the optical fiber to $125\ \mu\mathrm{m}$, reflects light back into the core because it is made from material with a lower refractive index than the core material. The outermost layer in a single-mode optical fiber is the polymer jacket

(also called buffer coating), which is a polymer coating to protect the core and the cladding from external damage and typically has a thickness of $125\ \mu m$ (Figure 1.12).

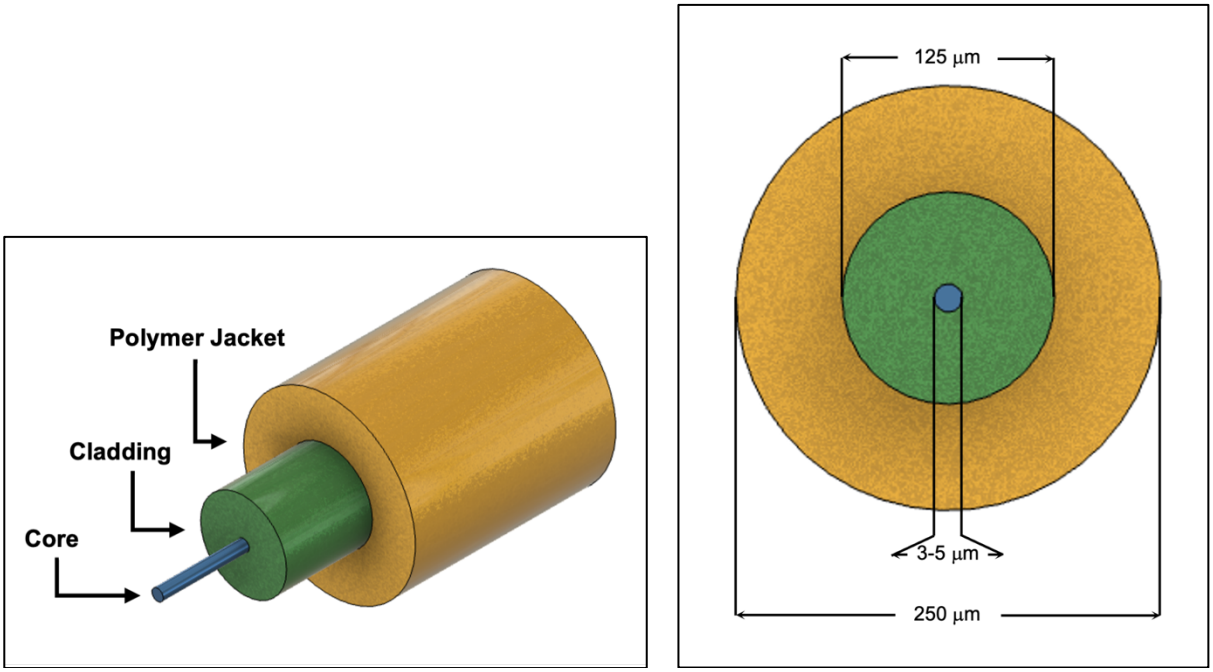

Figure 1.12: Schematic representation of the different layers of a single-mode optical fiber: (a) angled view showing the component layers, and (b) cross-sectional front view with the dimensions shown.

Light rays inside the core (with refractive index n_{core}) undergo total internal reflection at the interface between the core and the cladding (with refractive index n_{clad}) and are guided through the core because it is optically denser than the cladding (i.e., $n_{core} > n_{clad}$) as shown in Figure 1.13. After entering the core, incident rays that make an angle of refraction (θ_t) smaller than $90° - \theta_c$ (where θ_c is the critical angle between the core and the cladding), will undergo total internal reflection and will form guided rays in the fiber. Critical angle, θ_c, is the angle of the incident light that is calculated from Snell's

law of refraction ($n_1 Sin\theta_1 = n_2 Sin\theta_2$) (although some researchers give credit to Ibn Sahl for discovering the law of refraction first[28]) when the angle of the refracted light is $90°$. The largest angle an incident ray can have for total internal reflection in the core is called the acceptance angle (θ_{acc}). $2\theta_{acc}$ is called the acceptance cone, and sine of θ_{acc} is defined as the numerical aperture (NA) of the optical fiber.

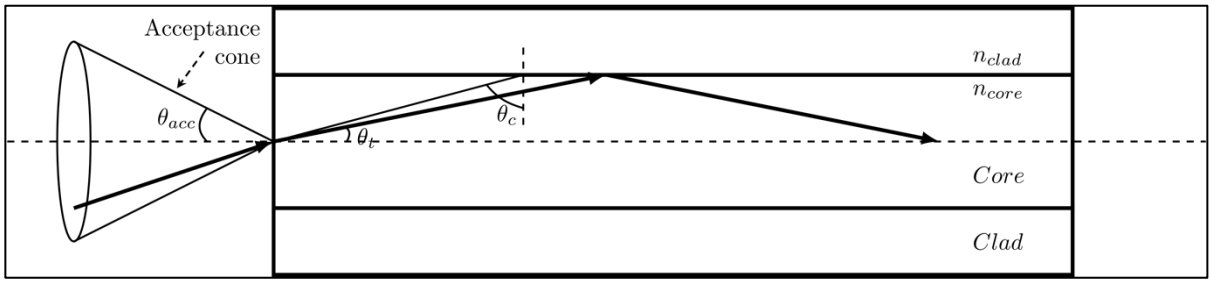

Figure 1.13: Schematic representation of guided light by total internal reflection inside an optical fiber.

There are two main steps in fabricating NSOM probes from optical fibers. The first step (a) is tapering the fiber so that a sharp apex is formed, then the second step (b) is coating the cone walls of the tapered fiber with opaque material such as aluminum to form a transmissive aperture at the apex.[18] A tapered optical fiber with a sharp tip can be forged in two ways: (i) the mechanical "heating and pulling" method, and (ii) chemical etching. In the mechanical "heating and pulling" method, the optical fiber is locally heated with a CO_2 laser and the fiber pulled from both ends with a commercial micropipette puller at a specific speed (Figure 1.14). This process results in two tapered ends with tip shapes that vary depending on the temperature, the timing of heating and pulling, as well as on the dimensions of the heated area .[3,18]

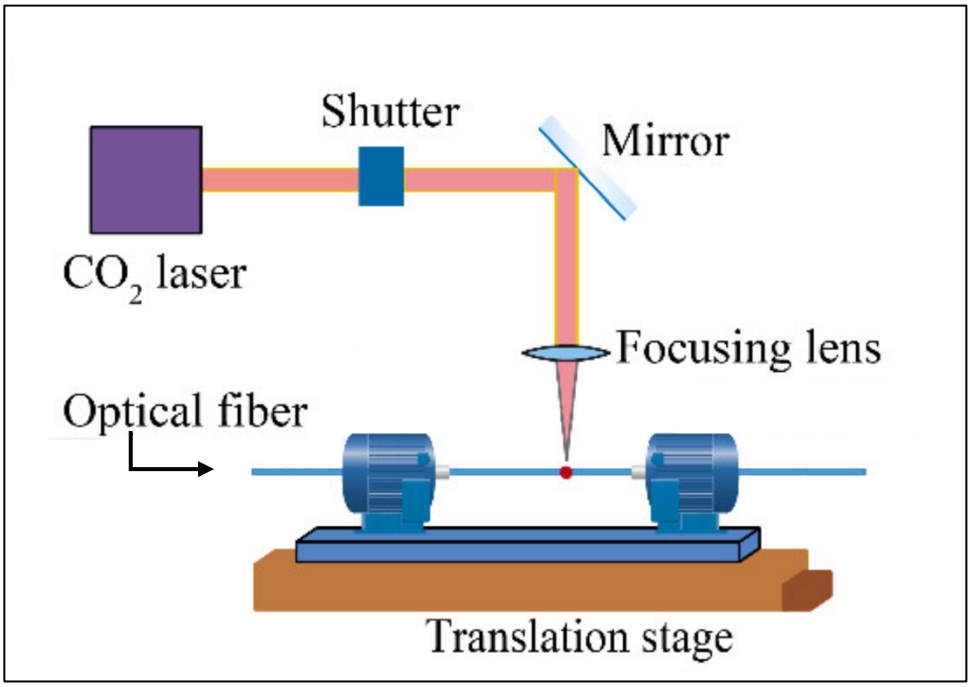

Figure 1.14: Schematic representation of creating tapered optical fiber by "heating and pulling" method illustrated by Ma et al. Adapted from Ref. 29.

Chemical etching of optical fibers to fabricate NSOM probes was popularized following development of the Turner method (also known as meniscus etching) where a bare optical fiber is immersed in a two-phase liquid usually consisting of hydrofluoric acid as the etching solution at the bottom and an organic oil as the protective layer at the top (Figure 1.15).[18,30] NSOM probe fabrication is completed by evaporating aluminum on the cone walls of the tapered optical fiber to create the aperture at the apex.

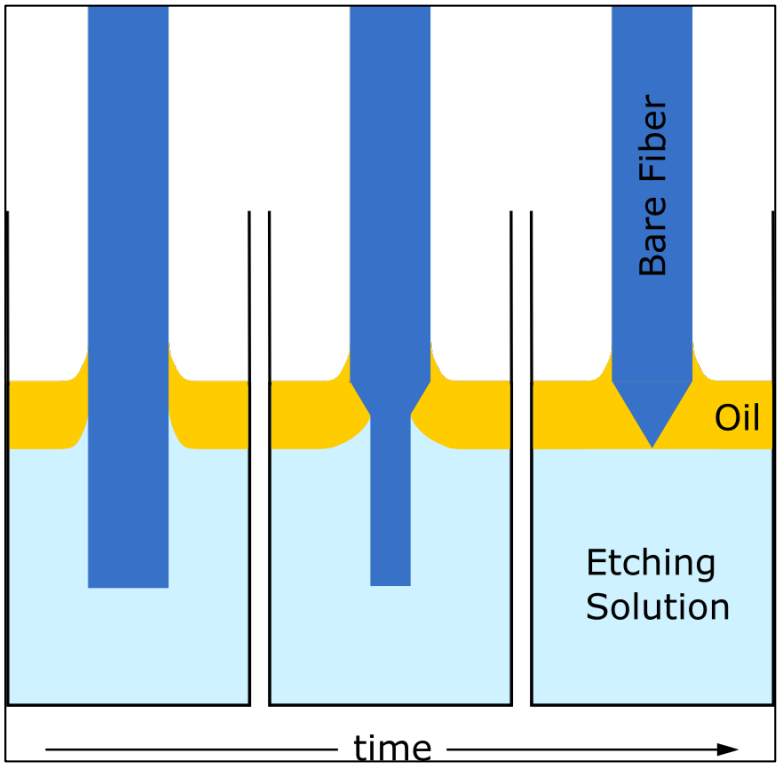

Figure 1.15: Schematic representation of fabricating tapered optical fiber by Turner method of chemical etching.

The tapered optical fiber is placed at a slight angle away from the aluminum evaporation source, and the fiber is rotated during the evaporation process so that aluminum is deposited on the walls of the cone but not on the apex of the tapered fiber because of the geometrical shadowing effect, causing the formation of a transparent aperture at the apex (Figure 1.16).[18]

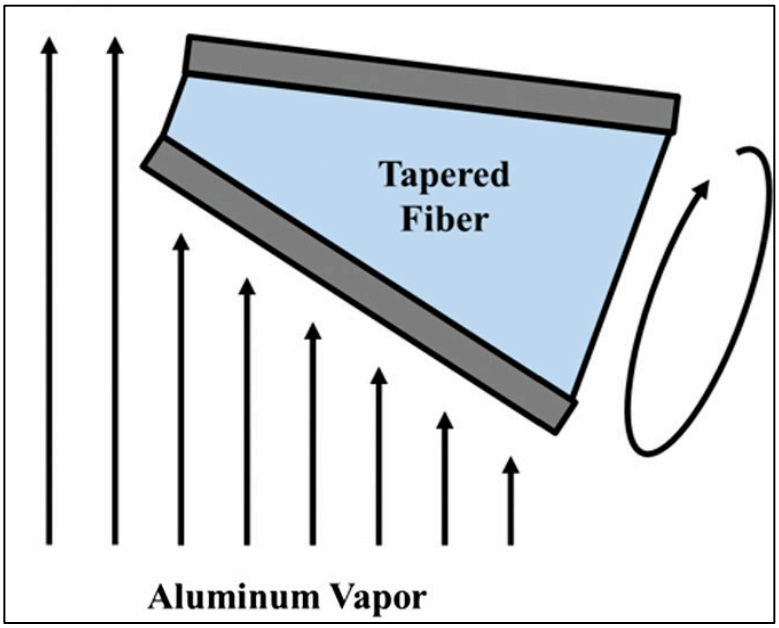

Figure 1.16: Schematic representation of metal evaporation on tapered optical fiber to create a transparent aperture at the apex illustrated by Adams et al. Adapted from Ref. 31.

1.5 Sensors

With the advancement of modern technologies, the use of sensors in everyday life has become a common phenomenon. Yet there is no single definition of a sensor that is accepted by all. One such definition is:

> *A sensor generally refers to a device that converts a physical measure into a signal that is read by an observer or by an instrument.* [32]

Sensors can be categorized into various classes (Figure 1.17) but are usually divided into (a) physical sensors, (b) chemical sensors, and (c) biosensors based on the type of attributes being measured.

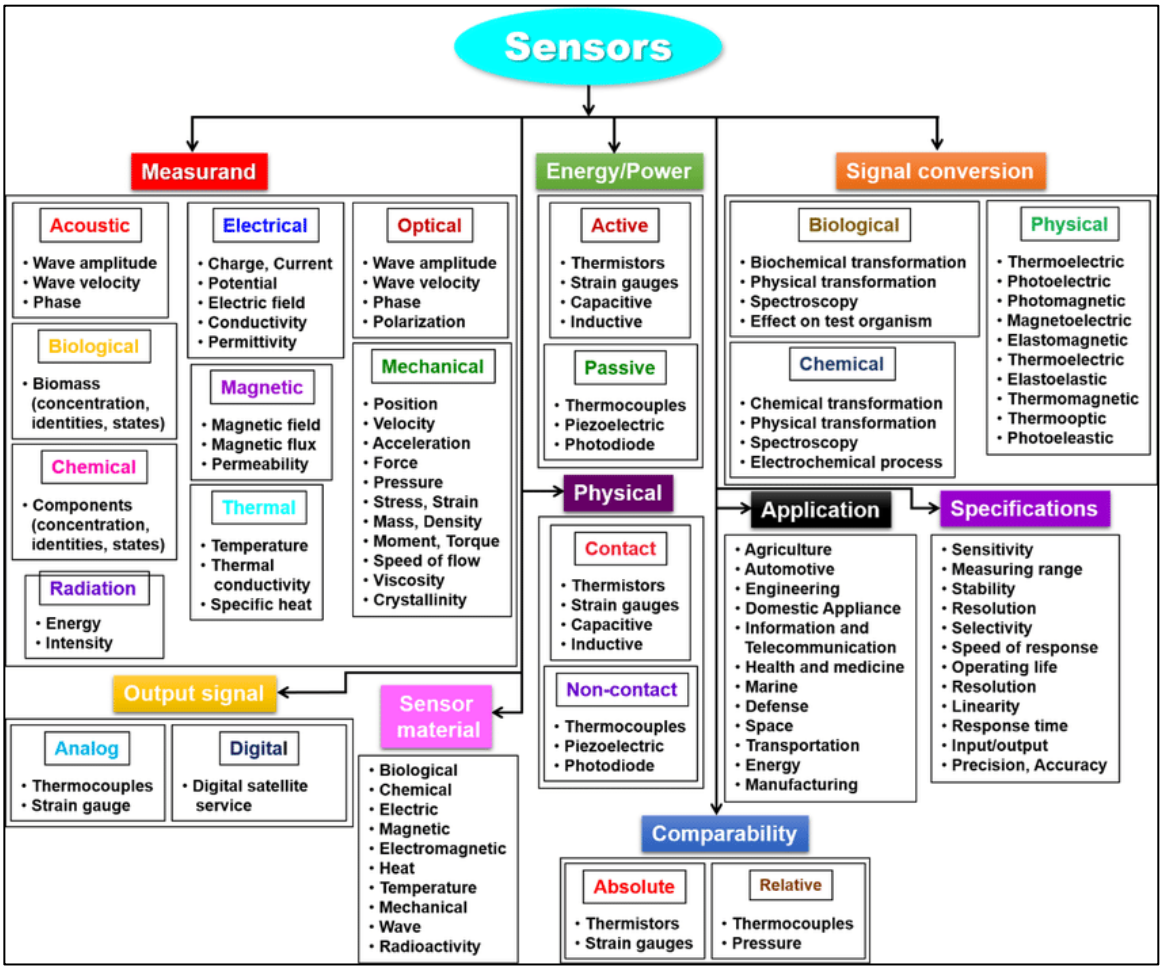

Figure 1.17: Classification of sensors illustrated by Naresh and Lee. Reprinted from Ref. 33.

1.5.1 Chemical Sensors

The International Union of Pure and Applied Chemistry (IUPAC) has defined chemical sensors as:

> *A chemical sensor is a device that transforms chemical information, ranging from the concentration of a specific sample component to total composition analysis, into an analytically useful signal.* [34]

The classification of chemical sensors according to IUPAC is shown by the following graphical representation (Figure 1.18):

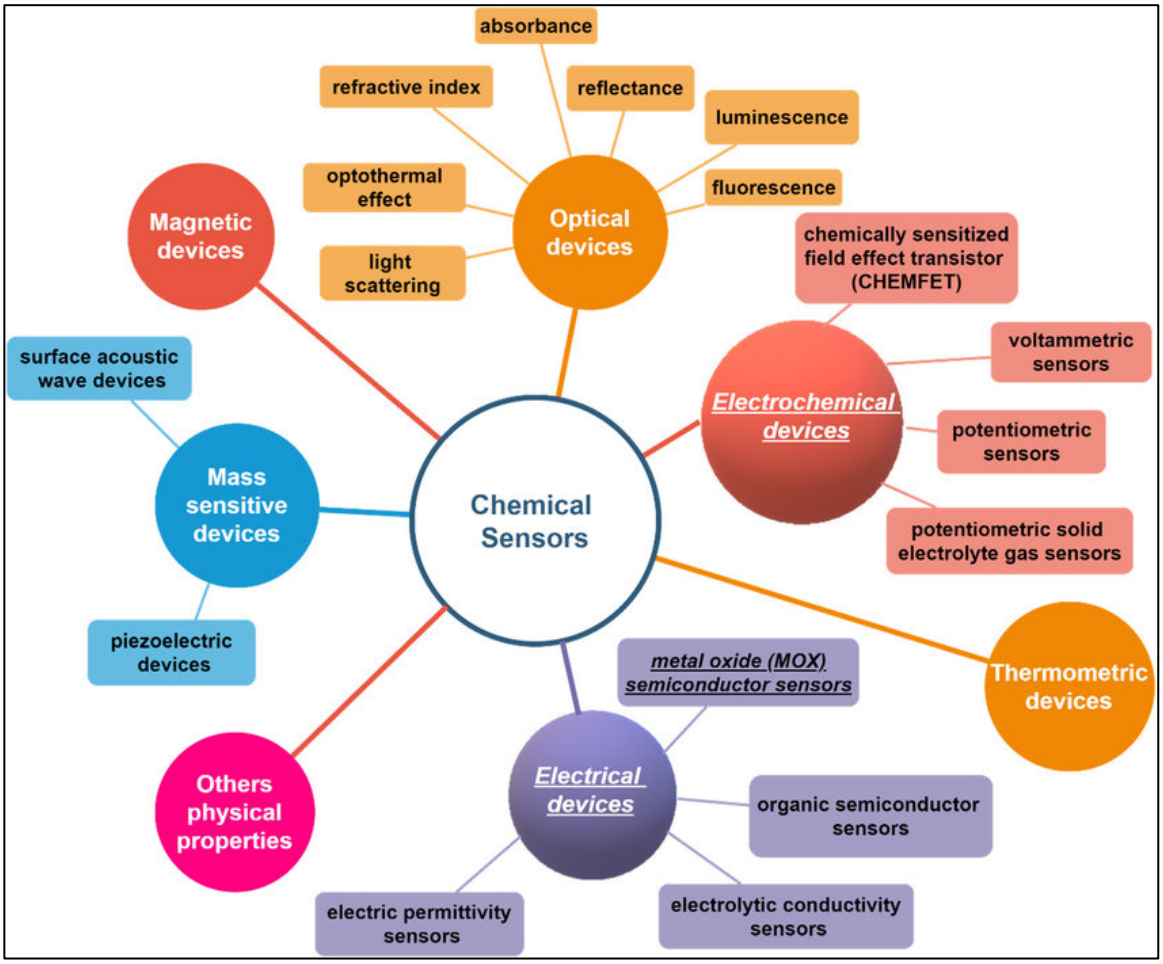

Figure 1.18: Classification of chemical sensors illustrated by Fazio et al. Reprinted from Ref. 35.

1.5.2 Optical Chemical Sensors

Optical chemical sensors are classified as a particular group of chemical sensors where the analytical signal in the transduction element is generated by electromagnetic (EM) radiation.[36] The advantages of using the optical chemical sensing technique over other sensing methods are that it is immune to electromagnetic interference, durable

under severe pressures and temperatures, and has high sensitivity.[37] A typical optical chemical sensor will have a chemical recognition phase (sensing element or receptor) coupled with a transduction element (Figure 1.19).

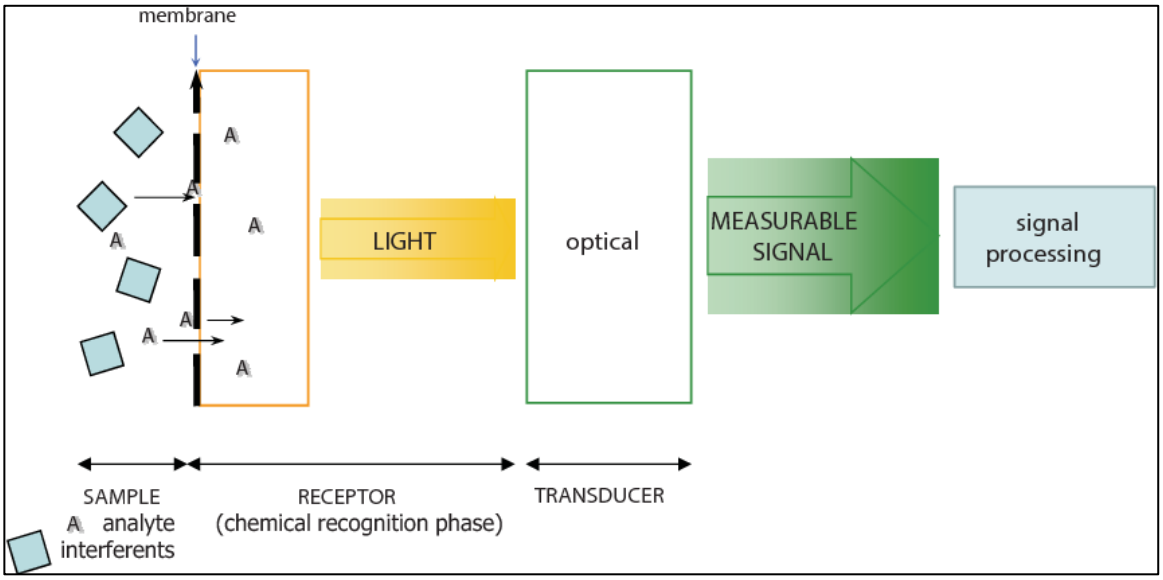

Figure 1.19: Schematic representation of an optical chemical sensor setup and process of sensing illustrated by Lobnik et al. Reprinted from Ref. 36.

The receptor detects a chemical parameter, e.g., pH, concentration of an ion, or a compound, etc., and generates an optical signal proportional to the magnitude of this parameter. The transducer converts the optical signal generated by the receptor into a measurable signal by amplifying and filtering the signal that is processed to record or display.[36] There are several types of optical chemical sensors based on the types of optical transduction techniques being used as shown in Figure 1.18. Amongst all of the different types of optical chemical sensors, fluorescent sensors are highly sought after due to their high sensitivity, and accuracy in practical applications compared to the other sensors types.[37]

References

(1) Abe, T.; Inoue, K.; Furuta, Y.; Kiyonari, H. Pronuclear Microinjection during S-Phase Increases the Efficiency of CRISPR-Cas9-Assisted Knockin of Large DNA Donors in Mouse Zygotes. *Cell Rep.* **2020**, *31* (7), 107653. https://doi.org/10.1016/j.celrep.2020.107653.

(2) Carpenter, W. B.; Dallinger, W. H. *The Microscope and Its Revelations*, 8th ed.; P. Blakiston's Son & Co.: Philadelphia, 1901.

(3) Ababneh, T. S. Design and Implementation of a Near-Field Scanning Optical Module for Inverted Microscopes. Ph.D. Dissertation, University of Wisconsin-Milwaukee, Milwaukee, WI, 2014.

(4) Croft, W. J. *Under The Microscope: A Brief History Of Microscopy*; World Scientific Publishing Company: Singapore, 1999.

(5) Rochow, T. G.; Tucker, P. A. *Introduction to Microscopy by Means of Light, Electrons, X Rays, or Acoustics*, 2nd ed.; Plenum Press: New York, 1994.

(6) Al-Khalili, J. In Retrospect: Book of Optics. *Nature* **2015**, *518* (7538), 164–165. https://doi.org/10.1038/518164a.

(7) *Inlay: British museum.* The British Museum. https://www.britishmuseum.org/collection/object/W_-90959 (accessed 2022-01-15).

(8) *This Month in Physics History*. http://www.aps.org/publications/apsnews/200403/history.cfm (accessed 2022-01-15).

(9) Murphy, D. B.; Davidson, M. W. *Fundamentals of Light Microscopy and Electronic Imaging*, 2nd ed.; Wiley-Blackwell: Hoboken, N.J, 2013.

(10) Beyond the Diffraction Limit. *Nat. Photonics* **2009**, *3* (7), 361–361. https://doi.org/10/fc2tm7.

(11) Dunst, S.; Tomancak, P. Imaging Flies by Fluorescence Microscopy: Principles, Technologies, and Applications. *Genetics* **2019**, *211* (1), 15–34. https://doi.org/10/gftg5n.

(12) Dunn, R. C. Near-Field Scanning Optical Microscopy. *Chem. Rev.* **1999**, *99* (10), 2891–2928. https://doi.org/10/dcr69v.

(13) Gris-Sánchez, I.; Van Ras, D.; Birks, T. A. The Airy Fiber: An Optical Fiber That Guides Light Diffracted by a Circular Aperture. *Optica* **2016**, *3* (3), 270. https://doi.org/10/gmr4n2.

(14) Kawata, S. *Near-Field Optics and Surface Plasmon Polaritons*; Topics in applied physics, v. 81.; Springer: Berlin ;, 2001.

(15) Girard, C.; Dereux, A. Near-Field Optics Theories. *Rep. Prog. Phys.* **1996**, *59* (5), 657–699. https://doi.org/10/cd36f7.

(16) Novotny, L.; Hecht, B. Principles of Nano-Optics.

(17) Novotny, L.; Stranick, S. J. NEAR-FIELD OPTICAL MICROSCOPY AND SPECTROSCOPY WITH POINTED PROBES. *Annu. Rev. Phys. Chem.* **2006**, *57* (1), 303–331. https://doi.org/10.1146/annurev.physchem.56.092503.141236.

(18) Hecht, B.; Sick, B.; Wild, U. P.; Deckert, V.; Zenobi, R.; Martin, O. J. F.; Pohl, D. W. Scanning Near-Field Optical Microscopy with Aperture Probes: Fundamentals and Applications. *J. Chem. Phys.* **2000**, *112* (18), 7761–7774. https://doi.org/10/bttvp3.

(19) Novotny, L. The History of Near-FIeld Optics. *Prog. Opt.* 47.

(20) Andolfi, L.; Trevisan, E.; Troian, B.; Prato, S.; Boscolo, R.; Giolo, E.; Luppi, S.; Martinelli, M.; Ricci, G.; Zweyer, M. The Application of Scanning near Field Optical Imaging to the Study of Human Sperm Morphology. *J. Nanobiotechnology* **2015**, *13* (1), 2. https://doi.org/10.1186/s12951-014-0061-5.

(21) Kim, J.; Song, K.-B. Recent Progress of Nano-Technology with NSOM. *Micron* **2007**, *38* (4), 409–426. https://doi.org/10/bqxvpq.

(22) Bazylewski, P.; Ezugwu, S.; Fanchini, G. A Review of Three-Dimensional Scanning Near-Field Optical Microscopy (3D-SNOM) and Its Applications in Nanoscale Light Management. *Appl. Sci.* **2017**, *7* (10), 973. https://doi.org/10/ggkps8.

(23) Betzig, E.; Finn, P. L.; Weiner, J. S. Combined Shear Force and Near-field Scanning Optical Microscopy. *Appl. Phys. Lett.* **1992**, *60* (20), 2484–2486. https://doi.org/10.1063/1.106940.

(24) Toledo-Crow, R.; Yang, P. C.; Chen, Y.; Vaez-Iravani, M. Near-field Differential Scanning Optical Microscope with Atomic Force Regulation. *Appl. Phys. Lett.* **1992**, *60* (24), 2957–2959. https://doi.org/10.1063/1.106801.

(25) Karrai, K.; Grober, R. D. Piezoelectric Tip-sample Distance Control for near Field Optical Microscopes. *Appl. Phys. Lett.* **1995**, *66* (14), 1842–1844. https://doi.org/10.1063/1.113340.

(26) Cady, W. G. The Piezo-Electric Resonator. *Proc. Inst. Radio Eng.* **1922**, *10* (2), 83–114. https://doi.org/10.1109/JRPROC.1922.219800.

(27) Berneschi, S.; Barucci, A.; Baldini, F.; Cosi, F.; Quercioli, F.; Pelli, S.; Righini, G. C.; Tiribilli, B.; Tombelli, S.; Trono, C.; Giannetti, A. Optical Fibre Micro/Nano Tips as Fluorescence-Based Sensors and Interrogation Probes. *Optics* **2020**, *1* (2), 213–242. https://doi.org/10.3390/opt1020017.

(28) Rashed, R. A Pioneer in Anaclastics: Ibn Sahl on Burning Mirrors and Lenses. *Isis* **1990**, *81* (3), 464–491.

(29) Ma, C.; Wang, J.; Yuan, L. Review of Helical Long-Period Fiber Gratings. *Photonics* **2021**, *8* (6), 193. https://doi.org/10.3390/photonics8060193.

(30) Nikbakht, H.; Latifi, H.; Oraie, M.; Amini, T. Fabrication of Tapered Tip Fibers With a Controllable Cone Angle Using Dynamical Etching. *J. Light. Technol.* **2015**, *33* (23), 4707–4711. https://doi.org/10/gmzqf4.

(31) Adams, W.; Sadatgol, M.; Güney, D. Ö. Review of Near-Field Optics and Superlenses for Sub-Diffraction-Limited Nano-Imaging. *AIP Adv.* **2016**, *6* (10), 100701. https://doi.org/10.1063/1.4964498.

(32) Chen, K. Y.; Janz, K. F.; Zhu, W.; Brychta, R. J. Redefining the Roles of Sensors in Objective Physical Activity Monitoring. *Med. Sci. Sports Exerc.* **2012**, *44* (1S), S13–S23. https://doi.org/10.1249/MSS.0b013e3182399bc8.

(33) Naresh, Varnakavi.; Lee, N. A Review on Biosensors and Recent Development of Nanostructured Materials-Enabled Biosensors. *Sensors* **2021**, *21* (4), 1109. https://doi.org/10.3390/s21041109.

(34) Hulanicki', A.; Geab, S.; Ingman, F. CHEMICAL SENSORS DEFINITIONS AND CLASSIFICATION. 4.

(35) Fazio, E.; Spadaro, S.; Corsaro, C.; Neri, G.; Leonardi, S. G.; Neri, F.; Lavanya, N.; Sekar, C.; Donato, N.; Neri, G. Metal-Oxide Based Nanomaterials: Synthesis, Characterization and Their Applications in Electrical and Electrochemical Sensors. *Sensors* **2021**, *21* (7), 2494. https://doi.org/10.3390/s21072494.

(36) Lobnik, A.; Turel, M.; Korent, pela. Optical Chemical Sensors:Design and Applications. In *Advances in Chemical Sensors*; Wang, W., Ed.; InTech, 2012. https://doi.org/10.5772/31534.

(37) Shin, Y.-H.; Teresa Gutierrez-Wing, M.; Choi, J.-W. Review—Recent Progress in Portable Fluorescence Sensors. *J. Electrochem. Soc.* **2021**, *168* (1), 017502. https://doi.org/10.1149/1945-7111/abd494.

CHAPTER 2

Theoretical Literature Review

2.1 Overview

This chapter discusses some of the theoretical postulations from published literature that are relevant to this research work. The chapter begins with the examination of the work of other researchers in studying the etching of silicon dioxide (SiO_2) by hydrofluoric acid (HF) solution and plausible mechanisms behind the etching process. Then it moves on to discuss the heterogeneous reactions, specifically the fluid-solid non-catalytic reactions and their established chemical kinetic models. Lastly, the chapter ends with the exploration of the wicking process in porous media and the mathematical models used to describe such a process.

2.2 SiO_2 Etching with HF Solution

Hydrofluoric acid (HF) is widely used in the glass industry to etch silicate glasses.[1] Although more than 200 years have passed since the discovery of glass etching by HF, the actual mechanism of SiO_2 etching in HF solution is yet to be fully understood. Even the generally accepted overall etch reaction of SiO_2 in HF solution given by Equation 2.1 is overgeneralized and not well established.[2,3]

$$SiO_2 + 6HF \rightleftharpoons H_2SiF_6 + 2H_2O \qquad (2.1)$$

The disagreement stems from the opinions that the solely produced hexafluorosilicate ion can dissolve up to $20\ mol\%$ more SiO_2 than the original HF solution. Other studies have

suggested that the final etch product contains at least two silicon atoms, i.e., decafluorodisilicic acid, according to Equation 2.2.[3]

$$4H^+(aq) + 5SiF_6^{2-}(aq) + SiO_2(s) \rightleftharpoons 3F_4SiSiF_6^{2-}(aq) + 2H_2O \qquad (2.2)$$

This indicates the overall etch reaction should look like Equation 2.3.[3]

$$10HF(aq) + 2SiO_2(s) \rightleftharpoons 2H^+(aq) + F_4SiSiF_6^{2-}(aq) + 4H_2O \qquad (2.3)$$

2.2.1 HF Solution Chemistry

It is well known that a fluoride ion (F^-) is formed when the weak acid HF partially dissociates. However, depending on the concentration of the HF solution, various forms of fluorine may exist. The chemical equilibria and their published equilibrium constants at $25°C$ for the major fluorine species found in HF solutions with concentrations < 1 M are expressed in the Equations 2.4-2.6.[1,4]

$$HF \rightleftharpoons H^+ + F^- \qquad [H^+][F^-]/[HF] = 6.85\times 10^{-4}\ mol{\cdot}L^{-1} \qquad (2.4)$$

$$HF + F^- \rightleftharpoons HF_2^- \qquad [HF_2^-]/[HF][F^-] = 3.963\ L{\cdot}mol^{-1} \qquad (2.5)$$

$$2HF \rightleftharpoons H_2F_2 \qquad [H_2F_2]/[HF]^2 = 6.85\times 10^{-4}\ L{\cdot}mol^{-1} \qquad (2.6)$$

Judge reported a linear correlation between the SiO_2 etch rate (R) and the concentrations of HF and HF_2^-, but independent of the F^- concentration which is given by the Equation 2.7.[1,3]

$$R = \mathrm{A}[\mathrm{HF}] + \mathrm{B}[\mathrm{HF}_2^-] + \mathrm{C} \quad (2.7)$$

However, this rate equation was only valid for low HF concentrations and low pH (< 2) values. At higher HF concentrations, polymeric species of HF such as $(\mathrm{HF})_\mathrm{n}$ and $\mathrm{F}(\mathrm{HF})_\mathrm{n}^-$ were suggested to play an important role. Several other chemical equilibria have been proposed including the generation of high order oligofluorohydrogenates shown by Equation 2.9.[3,4]

$$\mathrm{H_2O} + \mathrm{HF} \rightleftharpoons [\mathrm{H_3O^+ \cdot F^-}] \rightleftharpoons \mathrm{H_3O^+} + \mathrm{F^-} \quad (2.8)$$

$$\mathrm{HF_2^-} + \mathrm{HF} \rightleftharpoons \mathrm{H_2F_3^-} \quad (2.9)$$

Some researchers used a non-first order kinetics approach to express the $\mathrm{SiO_2}$ etch rate (R) as shown in Equations 2.10.[2,5,6]

$$R = \mathrm{k}[\mathrm{HF}]^\mathrm{n} \quad (2.10)$$

Other researchers introduced Langmuir-Hinshelwood kinetics in the rate equation (Equation 2.11) to describe the concentrations of reactive surface sites on the glass surface.[1,2,7]

$$R = \frac{\mathrm{k_1}[\mathrm{HF}]}{1 + \mathrm{k_2}[\mathrm{HF}]} \quad (2.11)$$

No one rate equation has yet explained the $\mathrm{SiO_2}$ etch rates for all HF concentrations.

2.2.2 SiO_2 Etching Mechanisms

Many mechanisms for the dissolution of SiO_2 by HF molecules have been postulated by various researchers since the 1940s using the kinetics data available at the time. Three such possible mechanisms are shown in Figure 2.1. The first mechanism called the chemical replacement of the hydroxyl groups (Figure 2.1(a)) can be discounted because increasing the HF_2^- concentration (and consequently that of the F^- species) does not increase the etching rate. In the case of the second mechanism, the hydrogen bonding of the HF species to the silanol groups on the silica surface (Figure 2.1(b)) may play a role in attracting the HF species to the surface but is most likely not strong enough to break a silicon-oxygen bond. A plausible mechanism, nucleophilic chemisorption at the lattice bonds (Figure 2.1(c)), proposes that the absorption of the attacking species increases the coordination of the surface silicon and consequently weakens the lattice bonds. The surface bonds by the attachment of HF protons to the adjacent lattice oxygens when HF molecules are absorbed at the silica surface.[7,8]

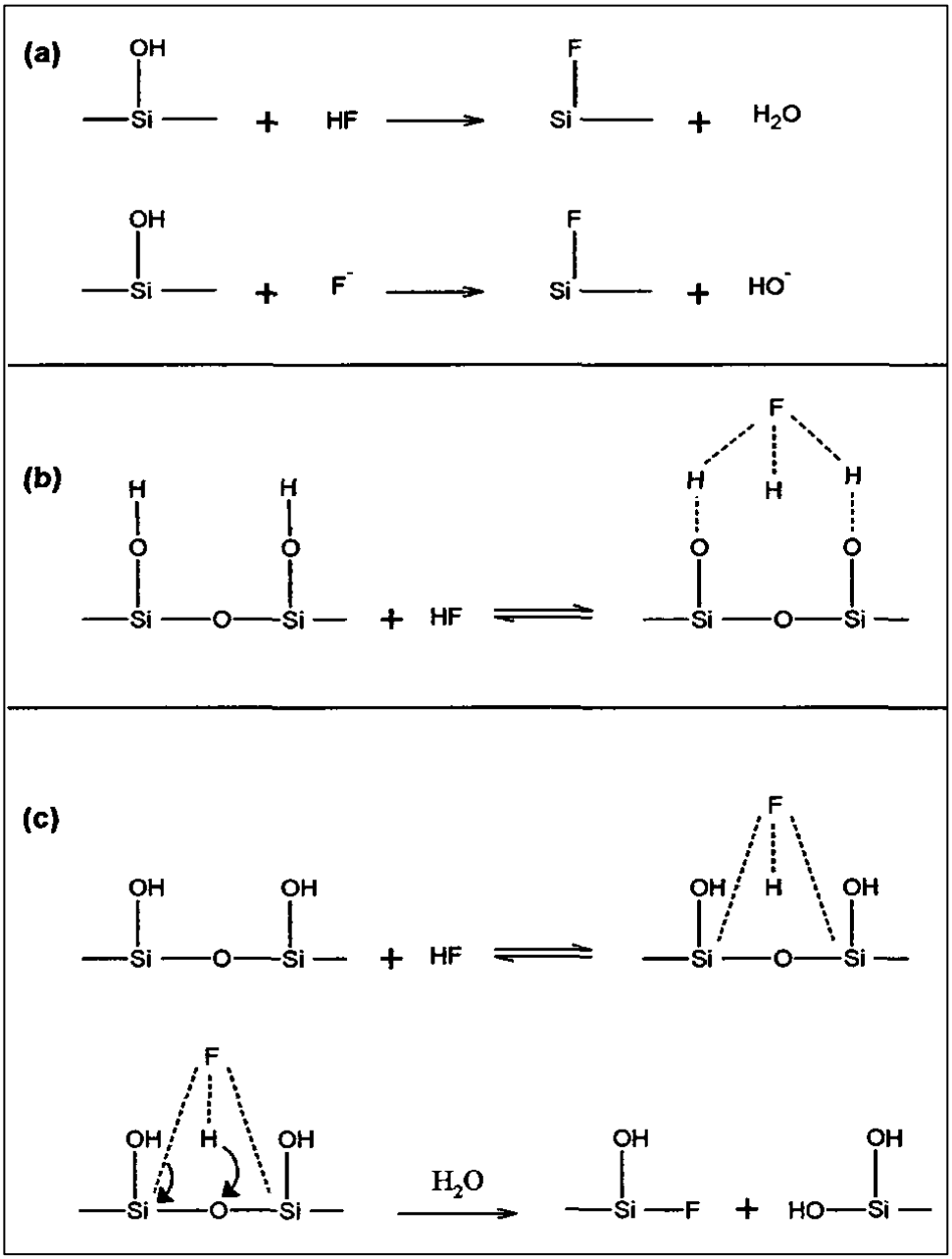

Figure 2.1: Three possible mechanisms for the chemical etching of silicon dioxide by hydrofluoric acid illustrated by Carlson: (a) Chemical replacement of surface hydroxyl groups, (b) Hydrogen bonding at lattice groups, and (c) Nucleophilic chemisorption at the lattice bonds. Reprinted from Ref. 8.

In a quartz crystal microbalance study, it was reported that the rate-determining step involved protonation and deprotonation of the reactive surface sites and it was

assumed that HF_2^- and $(HF)_2$ species were the primary etchant because their concentrations showed the same trends as that of the SiO_2 etch rate.[1,3] It was proposed that a reactive intermediate D is formed first by the elimination of OH^- or H_2O from the silica surface followed by the nucleophiles H_2F_2 and HF_2^- reacting with D to form the product E, the SiF unit (Figure 2.2).

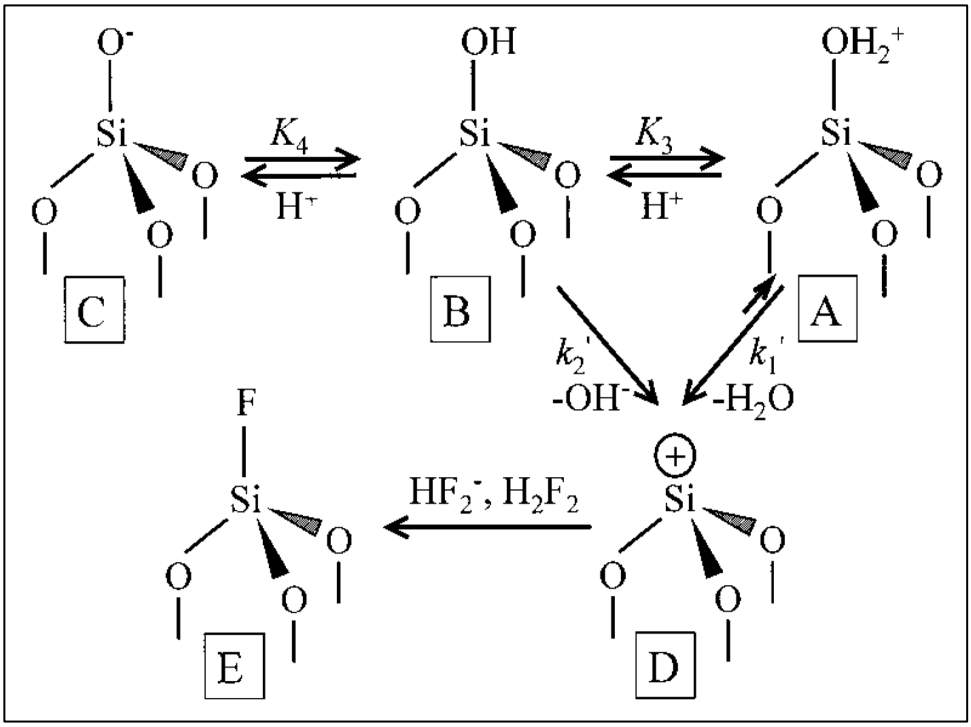

Figure 2.2: Reaction mechanism proposed by Knotter for the rate-determining reaction step of the dissolution of SiO_2 in HF solutions: replacement of the $SiOH$ unit by the SiF unit. Reprinted with permission from Ref. 1. Copyright 1999 American Chemical Society.

The resulting SiF unit breaks out of the SiO_2 matrix by three subsequent nucleophilic substitution reactions (Figure 2.3(a)). It was also proposed that elimination of OH^- and addition of F^- can take place consecutively when the FH part of H_2F_2 and HF_2^- lines up parallel to the HO side of the silanol group (Figure 2.3(b)).[1]

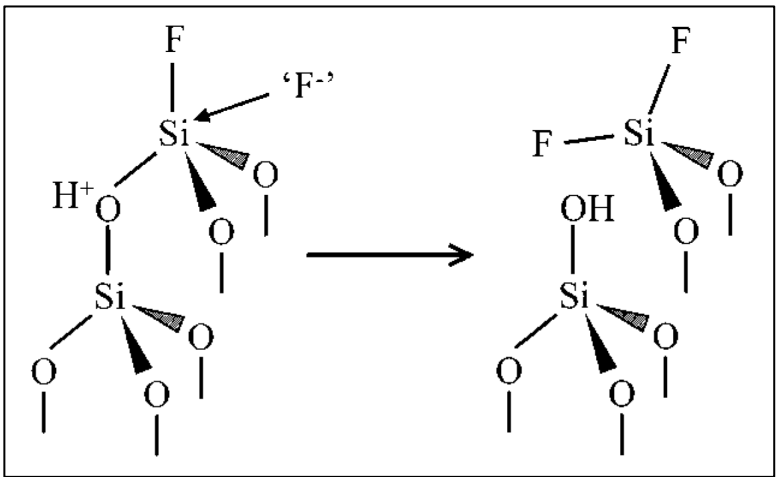

(a)

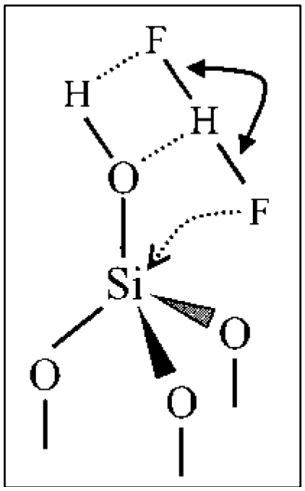

(b)

Figure 2.3: Schematic representation of (a) removal of the SiF unit from the SiO_2 matrix through nucleophilic substitution reactions, and (b) HF_2^- assisted OH^- elimination reaction with a consecutive F^- addition proposed by Knotter. Reprinted with permission from Ref. 1. Copyright 1999 American Chemical Society.

2.3 Heterogeneous Reaction

Chemical reactions are classified either as homogeneous or heterogeneous reactions. Heterogeneous reactions are those chemical reactions in which the reactants are components of two or more phases (e.g. gas and solid, liquid and solid, liquid and gas, two immiscible liquids) or in which one or more reactants undergo chemical change at the interface, e.g., on the surface of a solid catalyst.[9] If the heterogeneous reaction involves a solid catalyst for the reaction to happen then it is labeled as a catalytic reaction, otherwise it is called a non-catalytic reaction.[10]

2.3.1 Fluid-Solid Non-Catalytic Reaction

Fluid-Solid Non-Catalytic (FSNC) heterogeneous reaction systems such as fluidized solid processing of minerals, biomass, medicines, and fossil fuels are widely used in chemical metallurgical industries. FSNC reactions have been extensively studied due to their importance in these industries.[11–13] FSNC reactions can be represented by the general form shown in Equation 2.12.

$$\mathrm{A}_{(\mathrm{fluid})} + \mathrm{B}_{(\mathrm{solid})} \rightarrow \mathrm{C}_{(\mathrm{fluid\ or\ solid})} + \mathrm{D}_{(\mathrm{fluid\ or\ solid})} \qquad (2.12)$$

Examples of FSNC reactions are the reduction, roasting and chlorination of ores, decomposition reactions, carbonyl formation, gasification reactions, and causticizing reactions.[10] Although there are few extended models, the two basic models, the progressive-conversion model and the shrinking-core model, are the most common models to describe the FSNC reactions.[10,11,14,15] In the Progressive-Conversion Model

(PCM), also known as the homogeneous reaction model or the volume reaction model, the fluid penetrates deeply into the solid and the reaction will take place throughout the solid because the solid is porous and the rate of diffusion of the reactant fluid is high.[10] SiO_2 core and cladding in optical fibers are non-porous; so, PCM model can be ruled out as possible mechanistic pathway for the etching of optical fiber by HF. Therefore, the shrinking core model is explored next.

2.3.2 Shrinking Core Model

Shrinking Core Model (SCM), also known as the sharp interface model (SIM), assumes that reaction occurs at a sharp interface between a growing layer of solid product and a shrinking unreacted solid core.[10] This model was originally proposed by Yagi and Kunii (1955), who conceptualized the following five steps occurring in succession during a gas-solid non-catalytic reaction (Figure 2.4).[10,14]

Step 1. Diffusion of gaseous reactant A through the film surrounding the solid.

Step 2. Penetration and diffusion of A through the blanket of ash (the porous solid product) to the surface of the unreacted core.

Step 3. Reaction of gaseous reactant A with unreacted solid core B at the interface.

Step 4. Diffusion of gaseous products through the ash back to outer solid surface.

Step 5. Diffusion of gaseous products through the gas film back into the bulk fluid.

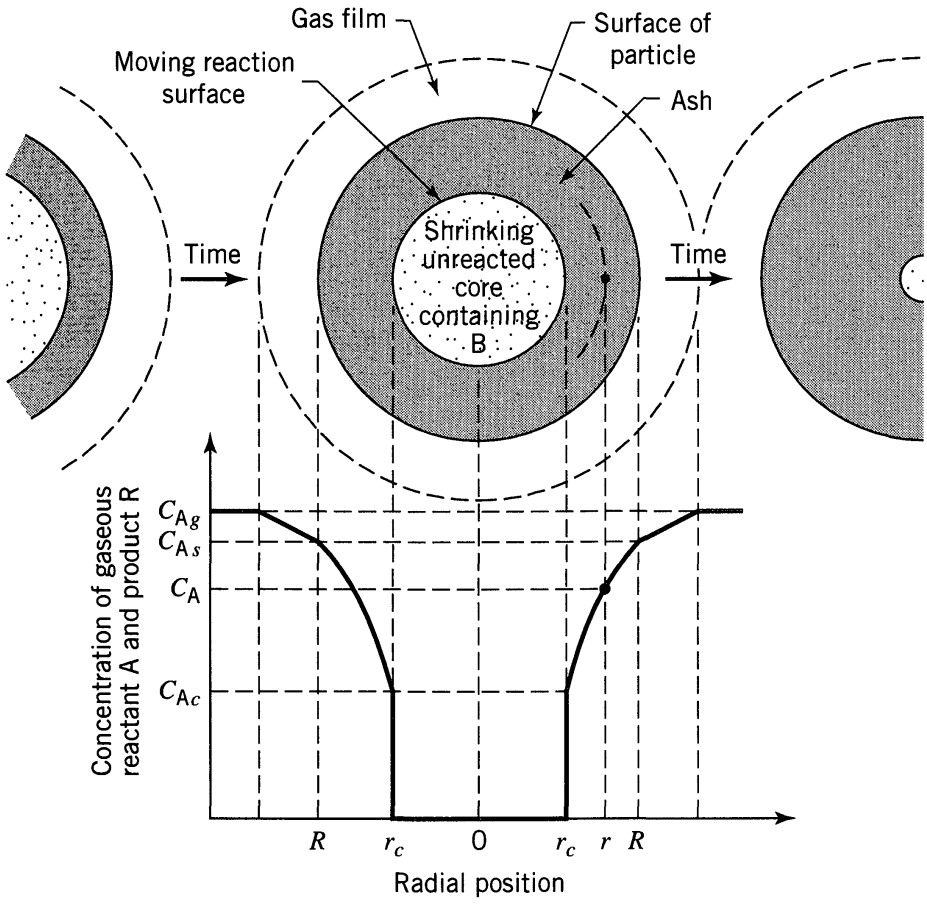

Figure 2.4: Schematic representation of the concentration profile of the reactants and products for a fluid-solid non-catalytic reaction in a shrinking core model illustrated by Levenspiel. Reprinted with permission from Ref 14. Copyright 1999 Wiley.

Some of these steps do not exist in some situations such, e.g., if no gaseous products are formed then steps 4 and 5 don't play any role in the rate of the reaction in which case the SCM model becomes the shrinking particle model (SPM). The rate controlling step in the SCM model can be either ash layer diffusion, fluid film diffusion or chemical reaction which is shown in the progressive conversion plot in Figure 2.5.[10,14]

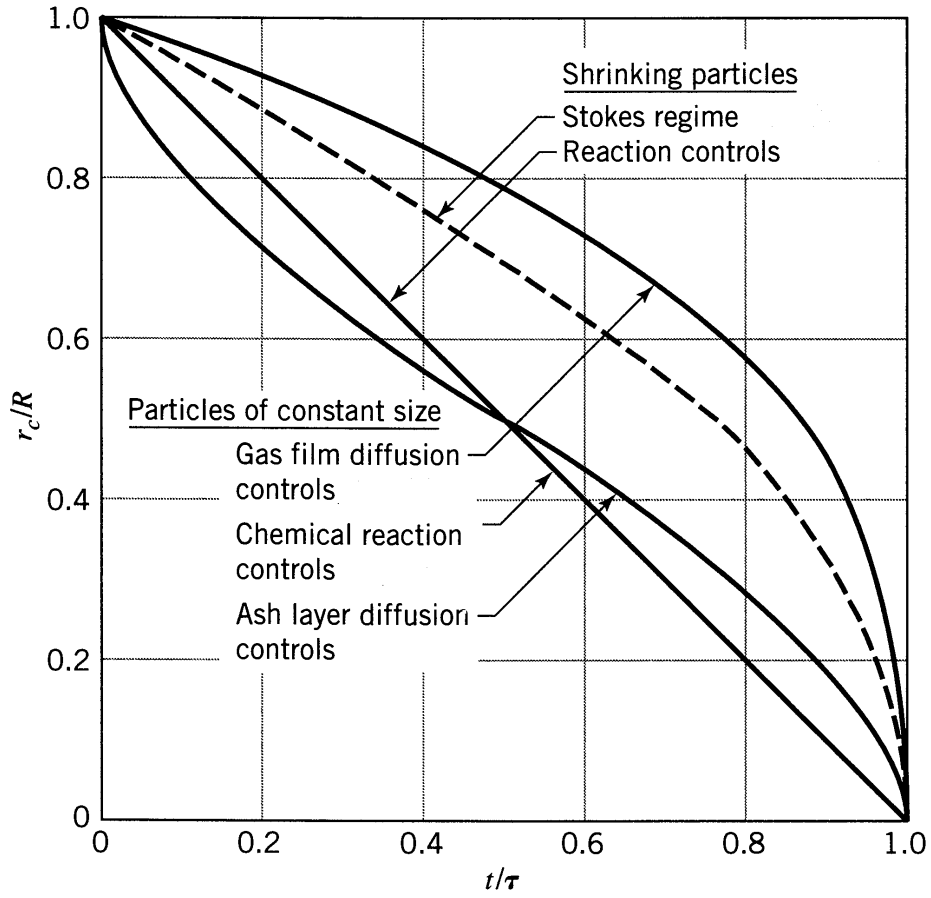

Figure 2.5: Graphical representation of the progress of reaction of a single spherical particle with surrounding fluid measured in terms of time for complete reaction illustrated by Levenspiel. Reprinted with permission from Ref. 14. Copyright 1999 Wiley.

2.4 Fluid Flow

A fluid is an assemblage of gas or liquid molecules that deforms constantly meaning it flows if shear stress is applied. Fundamental fluid properties are density ρ, viscosity μ, specific diffusivity D, heat capacities c_p and c_v, and thermal conductivity k, which are all dependent on temperature and species concentration. Fluid flows can be divided into: (i) Internal flows such as oil/air/water/steam in pipes, blood in arteries/veins,

water in rivers/canals, etc.; and (ii) External flows such as air past vehicles/building/planes, water past pillars/submarines, polymer coating on solid surfaces, etc. Driving forces behind fluid flow are gravity, pressure drops or gradients, temperature differences or gradients, surface tension, electromagnetic forces, and so on.[16]

2.4.1 Wicking

Displacement of one fluid by another immiscible and more viscous fluid in a porous medium is called imbibition. Wicking is spontaneous imbibition of a liquid into a porous substance driven by capillary pressure. During the wicking process of a wetting fluid in a capillary tube (with a radius $\mathrm{R_c}$), the capillary pressure (p_c) is expressed by the well-known Young-Laplace equation shown in Equation 2.13 where γ is the surface tension and θ is the contact angle of the wetting fluid.[17]

$$p_c = \frac{2\gamma\cos\theta}{\mathrm{R_c}} \qquad (2.13)$$

The traditional wicking model, which is described by the Lucas-Washburn (L-W) equation and was first proposed by Richard Lucas (1918) and later independently developed by Edward Wight Washburn (1921), considers the porous medium to be a bundle of aligned capillary tubes. The classical L-W equation (Equation 2.14) shows that the liquid imbibition height, $h(t)$, in porous media is proportional to the square root of time ($t^{0.5}$) when gravity and inertia effects can be neglected.[17,18]

$$h(t) = \sqrt{\frac{r\sigma\cos\theta}{2\mu}t} \qquad (2.14)$$

Here, μ is the viscosity of wetting liquid, θ is the contact angle, r is the tube radius, and σ is the surface tension of the wetting liquid. It was found that SCM model and wicking model seemed to play an important role in the fabrication of tapered optical fibers. We will go into more details about these models and their role in a possible etching mechanism of optical fibers in a subsequent chapter of this thesis.

References

(1) Knotter, D. M. Etching Mechanism of Vitreous Silicon Dioxide in HF-Based Solutions. *J. Am. Chem. Soc.* **2000**, *122* (18), 4345–4351. https://doi.org/10/c3rr4f.

(2) Monk, D. J.; Soane, D. S.; Howe, R. T. A Diffusion/Chemical Reaction Model for HF Etching of LPCVD Phosphosilicate Glass Sacrificial Layers. In *Technical Digest IEEE Solid-State Sensor and Actuator Workshop*; 1992; pp 46–49. https://doi.org/10/cz4pwq.

(3) Pande, A. A.; Mui, D. S. L.; Hess, D. W. SiO_2 Etching with Aqueous HF: Design and Development of a Laboratory-Scale Integrated Wet Etch/Dry Reactor. *IEEE Trans. Semicond. Manuf.* **2011**, *24* (1), 104–116. https://doi.org/10/fpz2qf.

(4) Shvartsev, B.; Gelman, D.; Komissarov, I.; Epshtein, A.; Starosvetsky, D.; Ein-Eli, Y. Influence of Solution Volume on the Dissolution Rate of Silicon Dioxide in Hydrofluoric Acid. *ChemPhysChem* **2015**, *16* (2), 370–376. https://doi.org/10.1002/cphc.201402627.

(5) Blumberg, A. A. Differential Thermal Analysis and Heterogeneous Kinetics The Reaction of Vitreous Silica with Hydrofluoric Acid. *J. Phys. Chem.* **1959**, *63* (7), 1129–1132. https://doi.org/10.1021/j150577a023.

(6) Blumberg, A. A.; Stavrinou, S. C. Tabulated Functions for Heterogeneous Reaction Rates: The Attack of Vitreous Silica by Hydrofluoric Acid. *J. Phys. Chem.* **1960**, *64* (10), 1438–1442. https://doi.org/10.1021/j100839a019.

(7) Kline, W. E.; Fogler, H. S. Dissolution of Silicate Minerals by Hydrofluoric Acid. *Ind. Eng. Chem. Fundam.* **1981**, *20* (2), 155–161. https://doi.org/10.1021/i100002a008.

(8) Carlson, C. A. Development of the Electrostatic Corral for the Trapping of Single Molecules in Solution. Ph.D. Dissertation, University of Wisconsin-Milwaukee, Milwaukee, WI, 2010.

(9) *Heterogeneous Reaction*. https://www.britannica.com/science/heterogeneous-reaction (accessed 2022-03-31).

(10) Pais, F. I. C. C.; Portugal, A. A. T. G. A Mathematical Model for Non-Catalytic Liquid-Solid Reversible Reactions. *Comput. Chem. Eng.* **1998**, *22* (3), 459–474. https://doi.org/10/dv4cmr.

(11) Wen, C. Y. Noncatalytic Heterogeneous Solid-Fluid Reaction Models. 21. https://doi.org/10/cnpwbp.

(12) Zou, Z.; Zhu, J.; Jia, J.; Du, Z.; Wang, Q.; Zhu, Q.; Li, H. CFD Simulation of a Fluid–Solid Non-Catalytic Reaction Based on a Structure-Based Mass Transfer Model: Shrinking Spherical Reaction. *Ind. Eng. Chem. Res.* **2020**, *59* (45), 19989–19998. https://doi.org/10/gm478q.

(13) Gupta, P.; Saha, R. K. Generalized Mathematical Modeling of Fluid-Solid Non-Catalytic Reactions Using Finite Volume Method: Multiple Reactions. *Can. J. Chem. Eng.* **2004**, *82* (5), 1096–1103. https://doi.org/10/dvftbn.

(14) Levenspiel, O. *Chemical Reaction Engineering*, 3rd ed.; Wiley: New York, 1999.

(15) Clements, J. L. An Experimental and Mathematical Investigation of Selective Fluid-Solid Reactions. Ph.D., University of Idaho, United States -- Idaho.

(16) Kleinstreuer, C. Modern Fluid Dynamics (2nd Edition).

(17) Masoodi, R.; Pillai, K. M. *Wicking in Porous Materials: Traditional and Modern Modeling Approaches*; Taylor & Francis Group: Baton Rouge, United States, 2012.

(18) Cai, J.; Jin, T.; Kou, J.; Zou, S.; Xiao, J.; Meng, Q. Lucas–Washburn Equation-Based Modeling of Capillary-Driven Flow in Porous Systems. *Langmuir* **2021**, *37* (5), 1623–1636. https://doi.org/10.1021/acs.langmuir.0c03134.

CHAPTER 3

Materials and Methods

3.1 Overview

This chapter describes the resources being used and the experimental procedures being carried out to complete this research work. It begins with listing all experimental materials (both chemical and nonchemical). After that, a list of equipment and tools is provided that played a significant role in this work. Subsequently, a compilation of software and programming platforms is provided that were employed to run the experimental procedures as well as to analyze the experimental data. Next, in the methods section, the experimental setups and procedures are described in detail. This includes the setup for chemical etching of optical fibers, the process of creating NSOM probes by the sealed-tube method, making the probe surfaces hydrophilic by the surface cleaning procedures, covalently attaching silane coupling agents to the probe surfaces, functionalizing the silanized probes with fluorescent molecules, and detecting pH and metal ions in solution using the functionalized NSOM probes.

3.2 Materials

This research project involved experiments of sensitive and precise nature such as fabricating NSOM probes with nanoscale tip diameter, functionalizing the probes, and utilizing the functionalized probes in sensing trials. Therefore, pure chemicals and clean materials were used, and NSOM probes were carefully handled to ensure minimal interference during the experiments. In addition, some chemicals were needed as precautionary measures due to the hazardous acids used in the probe fabricating

process. The following gives the account of chemicals used for the different experiments in this research project:

- 40% Hydrofluoric acid (Honeywell, Charlotte, NC)
- Calcium gluconate (Attard's Minerals, San Diego, CA)
- Calcium carbonate (Thermo Fisher Scientific, Waltham, MA)
- 98% Sulfuric acid (Honeywell, Charlotte, NC)
- 95% Nitric acid (Sigma-Aldrich, St. Louis, MO)
- Mercury (Thermo Fisher Scientific, Waltham, MA)
- Silicone oil (Acros Organics, Geel, Belgium)
- 99% Hydrochloric acid (Thermo Fisher Scientific, Waltham, MA)
- Methanol or MeOH (Sigma-Aldrich, St. Louis, MO)
- Isopropanol or 2-Propanol (Thermo Fisher Scientific, Waltham, MA)
- Acetone (Sigma-Aldrich, St. Louis, MO)
- (3-Aminopropyl)triethoxysilane or APTES (Thermo Fisher Scientific, Waltham, MA)
- Fluorescein 5-isothiocyanate or FITC (Thermo Fisher Scientific, Waltham, MA)
- Absolute ethanol or EtOH (Thermo Fisher Scientific, Waltham, MA)
- Rhodamine B (Acros Organics, Geel, Belgium)
- 1-Ethyl-3-(3-dimethylaminopropyl)carbodiimide or EDC (Thermo Fisher Scientific, Waltham, MA)
- 4-Dimethylaminopyridine or DMAP (Thermo Fisher Scientific, Waltham, MA)
- Dichloromethane or DCM (Thermo Fisher Scientific, Waltham, MA)
- Iron (III) chloride hexahydrate (Thermo Fisher Scientific, Waltham, MA)

- Anhydrous copper (II) sulfate (Thermo Fisher Scientific, Waltham, MA)
- Sodium hydroxide pellets (Thermo Fisher Scientific, Waltham, MA)

Ultrapure water with a resistivity of $18.2\ \mathrm{M\Omega\text{-}cm}$ was always used in cleaning, rinsing, and preparing solutions. Ultrapure water was produced from a reverse-osmosis (RO) water supply line using the Sartorius Arium 611 VF ultrapure water system (Sartorius, Goettingen, Germany). S405-XP pure silica core single-mode optical fiber (Coherent, Santa Clara, CA) was used in the chemical etching process to fabricate NSOM probes. In some of the experiments, 1” x 3” microscope slides (VWR, Radnor, PA) were used to place sample solution drops, whereas in other experiments 1” x 1” microscope coverslips (VWR, Radnor, PA) were used.

3.3 Equipment and Tools

In this research, several different tools and equipment performed various tasks necessary for the different experiments. Only the more complex and important equipment and tools are listed below with a brief description:

1) XY Translation Stage (Arrick Robotics, Tyler, TX): This instrument, which was controlled by a computer program developed in-house, was vital for precise movement of the optical fiber between different hazardous acid solutions as well as automating the chemical etching procedure.
2) Custom-made Teflon Holder: Optical fiber was clamped to this holder, which was mounted on the mobile unit of the XY translation stage.

3) Teflon Beaker: Hydrofluoric acid was contained in this beaker during the chemical etching of the optical fiber. Special containment is a requirement for HF due to its ability to react with glass as well as many plastics.
4) Thermo Haake DC10 Recirculating Water Bath (Thermo Fisher Scientific, Waltham, MA): The hydrofluoric acid beaker was placed in this water bath to keep the temperature constant during the etching experiments.
5) Sartorius Arium 611 VF Ultrapure Water System (Sartorius, Goettingen, Germany): Ultrapure water with a resistivity of $18.2\ \mathrm{M\Omega\text{-}cm}$, which was used in the experiments, was produced from RO water supply line by this system.
6) Isotemp 506G Incubating Oven (Thermo Fisher Scientific, Waltham, MA): Surface reaction of vapor silane coupling agents were conducted inside this oven with a set high temperature.
7) FK12 Precision Fiber Optic Cleaver (Photon Kinetics, Beaverton, OR): Optical fibers were cleaved using this device.
8) Hitachi S-4800 II FE-SEM (Hitachi, Tokyo, Japan): All the Scanning Electron Microscopy (SEM) images of the NSOM probes were generated by this system.
9) Zeiss Axiovert 200M Inverted Microscope (Zeiss, Jena, Germany): Some of the experiments required utilizing this inverted optical microscope to produce brightfield or fluorescence images.
10) Cascade II EMCCD Camera (Teledyne Photometrics, Tucson, AZ): The images that were produced by the Zeiss Axiovert 200M Inverted Microscope were captured by this EMCCD (electron multiplying charge coupled device) camera.

11) Stabilite 2017 Ion Laser (Spectra-Physics, Mountain View, CA): This laser source was used for fluorescence experimentation and imaging.
12) Newport 1918-R Optical Power Meter (Newport, Irvine, CA): Laser power was measured and monitored with this power meter.
13) Custom-made Tools: Several tools were designed and custom-made from aluminum or stainless steel for specific experimental purposes.
    a. A metal scaffolding that was made to keep the hazardous acid containers in a fixed position.
    b. An attachment for the Teflon holder so that multiple optical fibers can be attached side by side on the holder.
    c. An NSOM probe holder was made so that the probe can be placed in solutions without breaking the tip.
    d. An SEM stage was made to securely hold multiple NSOM probes for SEM imaging.
    e. A sample stage so that NSOM probes can be tightly held at an angle while allowing for removal of the microscope coverslip with sample.

3.4 Software and Programming Platforms

The equipment used in this research project was operated by either proprietary software or programs developed in-house using licensed programming platforms. Postprocessing and analyzing of data were done by either open-source programs or

licensed software and programming platforms. These software and programming platforms are enumerated below with a brief description:

1) LabVIEW: LabVIEW is a graphical programming environment to develop automated test systems. The LabVIEW license was purchased from National Instruments, Inc. and was used to develop programs in-house to control various instruments, e.g., to control and automate the XY Translation Stage. LabVIEW was also used to develop the program to control the Zeiss Axiovert 200M Inverted Microscope and Cascade II EMCCD Camera from a computer for optical images acquisition.
2) Hitachi PC-SEM: Hitachi PC-SEM software is the proprietary software that comes with the computer that controls the Hitachi S-4800 II FE-SEM.
3) Quartz PCI: Quartz PCI is a proprietary software that provides digital image capture for the SEM images generated by the Hitachi S-4800 II FE-SEM.
4) COMSOL: COMSOL is a proprietary multiphysics simulation software based on advanced numerical methods and was used to develop a simulation model for etching of optical fiber.
5) MATLAB: MATLAB is a proprietary programming and numeric computing platform and was used for analyzing data and post-processing of the SEM and the fluorescence images.
6) Fiji: Fiji is open-source image processing distribution package of ImageJ. Fiji was used to determine the cone angle of the different NSOM probes from the captured SEM images.

3.5 Methods

3.5.1 Chemical Etching Setup

The Turner method (also known as meniscus etching) and the modified sealed-tube (MST) etching are the two chemical etching methods that were used in this research project to fabricate NSOM probes for different experiments.[1–3] MST etching requires the use of hydrofluoric acid (HF) and mercury, two of the most hazardous chemicals that were used, along with concentrated sulfuric acid ($\mathrm{H_2SO_4}$) and concentrated nitric acid ($\mathrm{HNO_3}$). Therefore, extraordinary measures were taken to avoid exposure to these hazardous chemicals, which led to the implementation of the etching setup as shown in Figure 3.1.

Mercury, HF and silicone oil were put in the Teflon beaker, which was held fixed in the temperature-controlled water bath by the metal scaffolding. The water bath temperature was set to $20.0°\mathrm{C}$ for all the chemical etching experiments in this research work. Two layers of personal protective equipment that are resistant to HF were donned before handling of any HF solution. Single-mode optical fiber was etched by HF inside this Teflon beaker. Another glass beaker with a mixture of conc. $\mathrm{H_2SO_4}$ and conc. $\mathrm{HNO_3}$ heated to $200°\mathrm{C}$ on a hot plate was securely fixed by the same metal scaffolding.

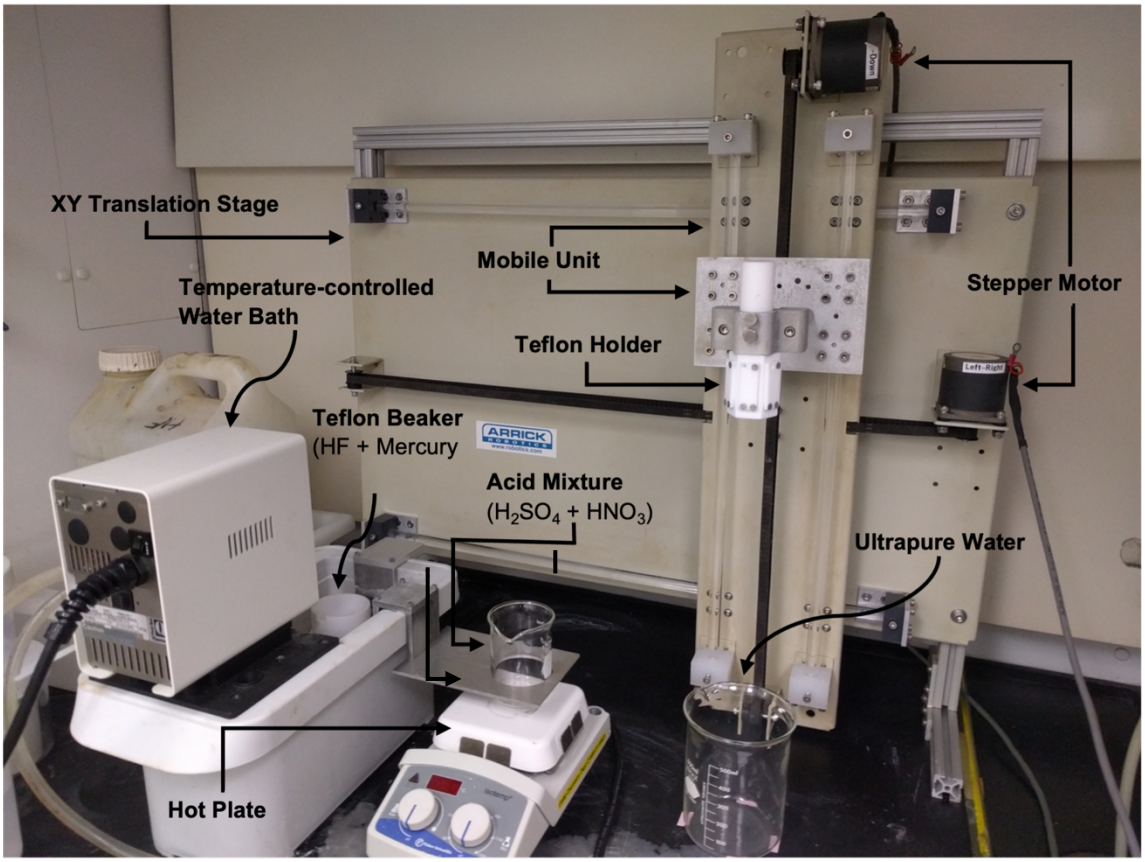

Figure 3.1: Setup for the chemical etching method to fabricate NSOM probes from single-mode optical fibers.

The polymer jacket of the optical fiber was dissolved by the acid mixture inside this second beaker. A third beaker with ultrapure water was used to clean off the acids from the etched optical fiber. The optical fiber was fastened tightly to the custom-made Teflon holder which was mounted on the mobile unit of the XY translation stage. The XY translation stage was controlled by a custom LabVIEW program developed in-house. As shown in Figure 3.2, the LabVIEW program allows specifying the etching time, i.e., the time the optical fiber stays in the HF etching solution, the speed of the mobile stage movement, the distance it moves, the stripping time, i.e., the time the etched optical fiber stays in the acid mixture, the cleaning time, i.e., the time it stays in the ultrapure water.

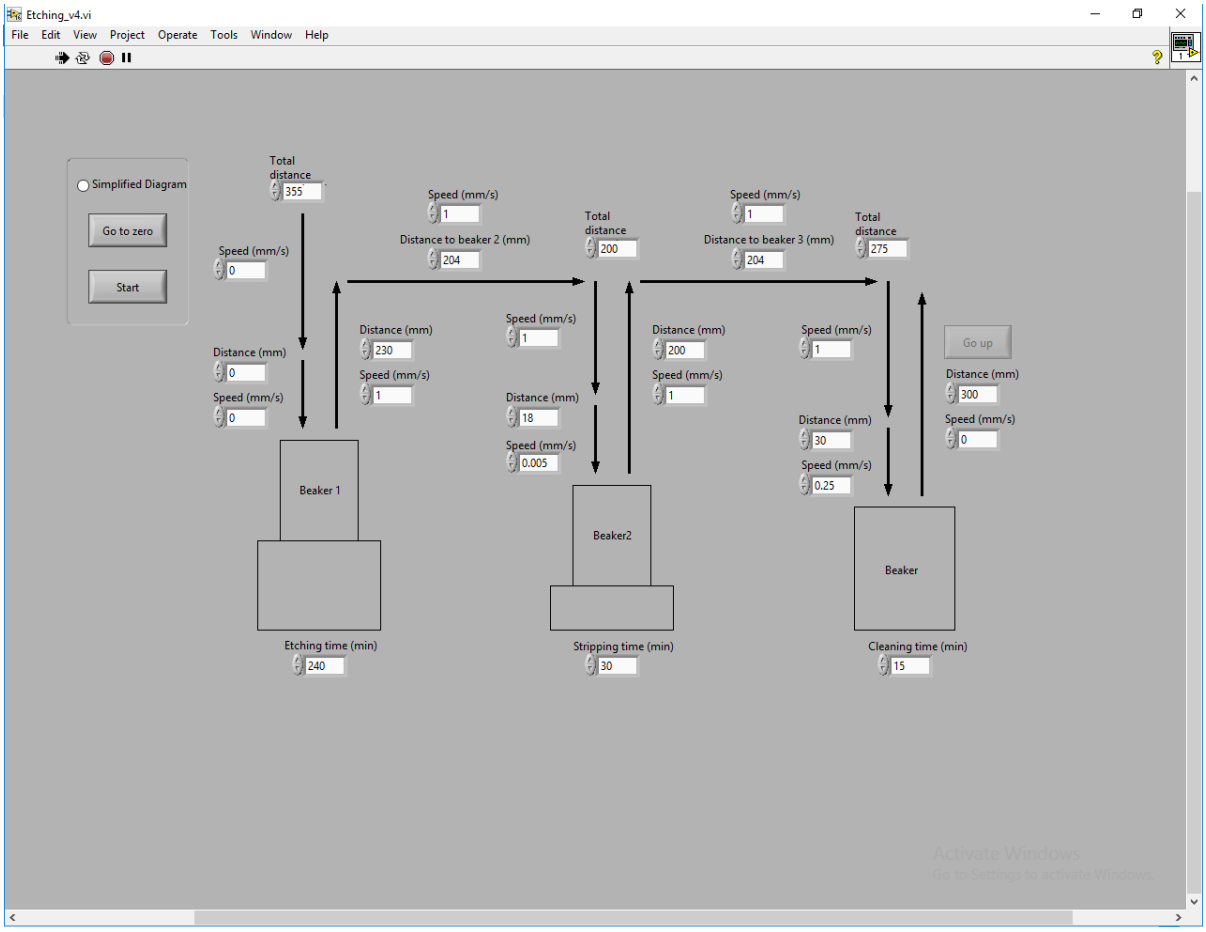

Figure 3.2: User interface of the LabVIEW program developed in-house that controls the XY translation stage for the HF etching of optical fibers.

3.5.2 Time-dependent MST Etching

MST etching was used for the time-dependent chemical etching experiments in this research work. In the MST etching developed in-house, the bottom end of the optical fiber is inserted into a layer of mercury at the bottom of the beaker containing HF solution instead of sealing it with HF-impermeable plastic.[3] Single-mode optical fibers were cut to a length of $70\ \mathrm{mm}$ from the optical fiber spool for each of the time-dependent etching experiment. Fibers were securely placed on the Teflon holder so that a $45\ \mathrm{mm}$ long part

of the fiber was sticking out from the bottom end of the Teflon holder. The Teflon holder was mounted onto the mobile unit of the XY Translation stage and positioned at the starting point (the top left corner). Only the etching time was adjusted for each etching experiment, but the stripping time and the cleaning time were kept at the same values in the LabVIEW program (Figure 3.2). Also, fresh HF solution was used for each etching experiment.

Once the LabVIEW program is started, the optical fiber descends into the HF beaker (Figure 3.3(a)) where it stays for the specified etching time. Then it is pulled out and is lowered into the acid mixture beaker (Figure 3.3(b)) where it stays for the specified stripping time, before it is pulled out and lowered into the ultrapure water beaker.

(a) **(b)**

Figure 3.3: (a) Optical fibers attached to the Teflon holder are placed in the 1st beaker containing 40% HF solution for etching. (b) Etched optical fibers are transferred to the 2nd beaker containing the acid mixture in order to dissolve the polymer jacket.

When the program stops and the Teflon holder is taken out of the ultrapure water, the fully formed NSOM probe (Figure 3.4(a)) can be seen sticking out about $10 - 15\ \mathrm{mm}$ from the holder's bottom edge (Figure 3.4(b)).

(a) **(b)**

Figure 3.4: (a) Fully formed NSOM probe taken out of the ultrapure water after the etching experiment. (b) Formed tip extends out to about 10-15 mm from the Teflon holder's bottom edge.

The NSOM probes from each etching experiment are then investigated by SEM (Figure 3.5) at different magnifications; the images were later analyzed to determine the cone angle.

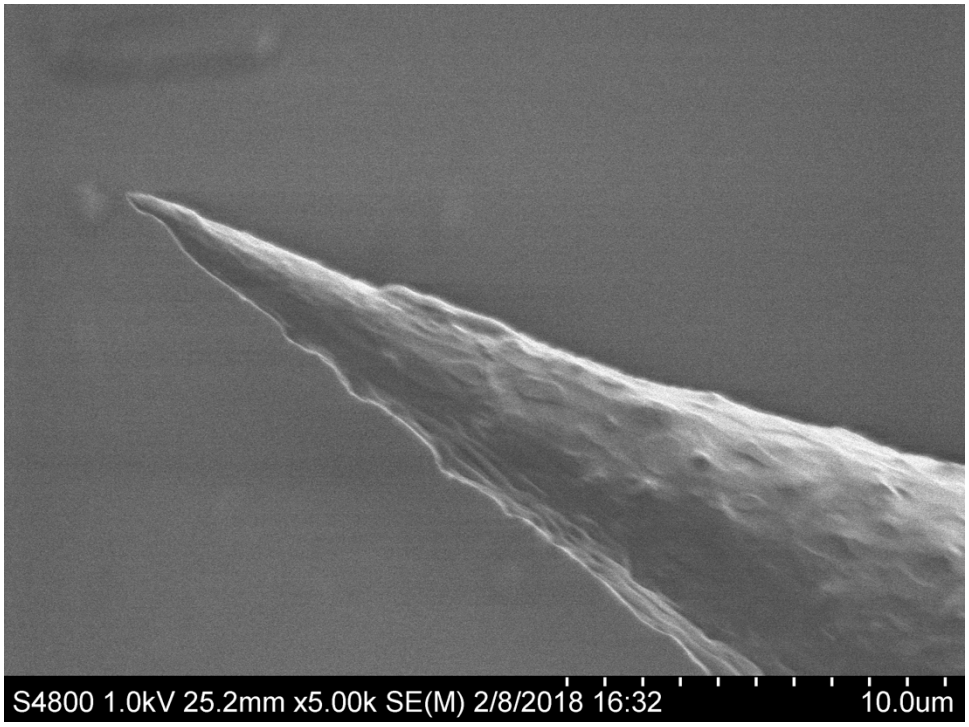
S4800 1.0kV 25.2mm x5.00k SE(M) 2/8/2018 16:32
10.0um

(a)

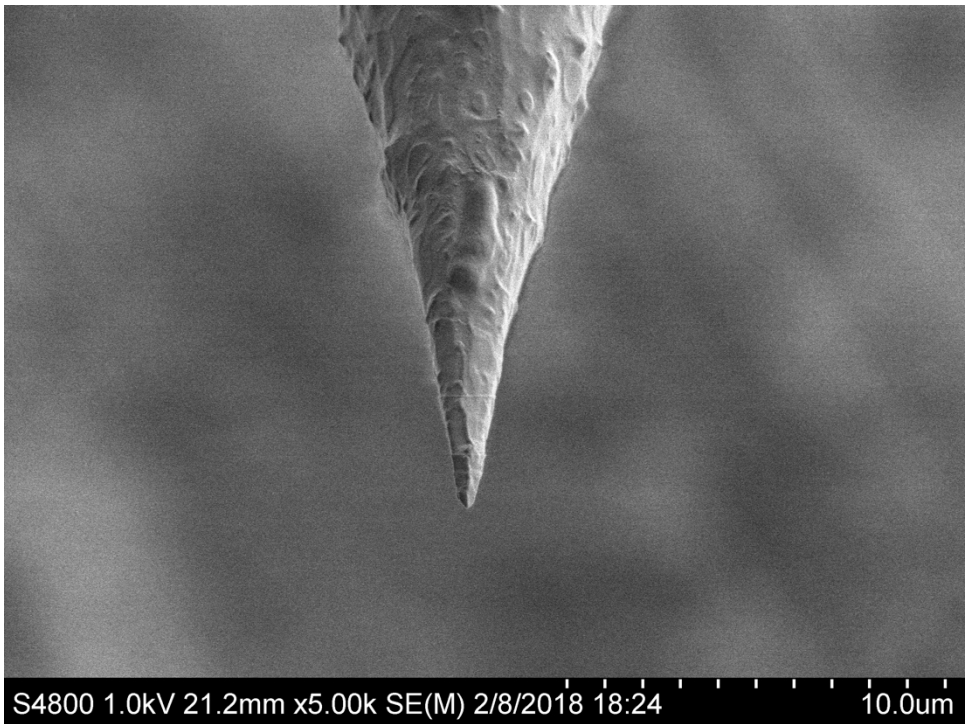
S4800 1.0kV 21.2mm x5.00k SE(M) 2/8/2018 18:24
10.0um

(b)

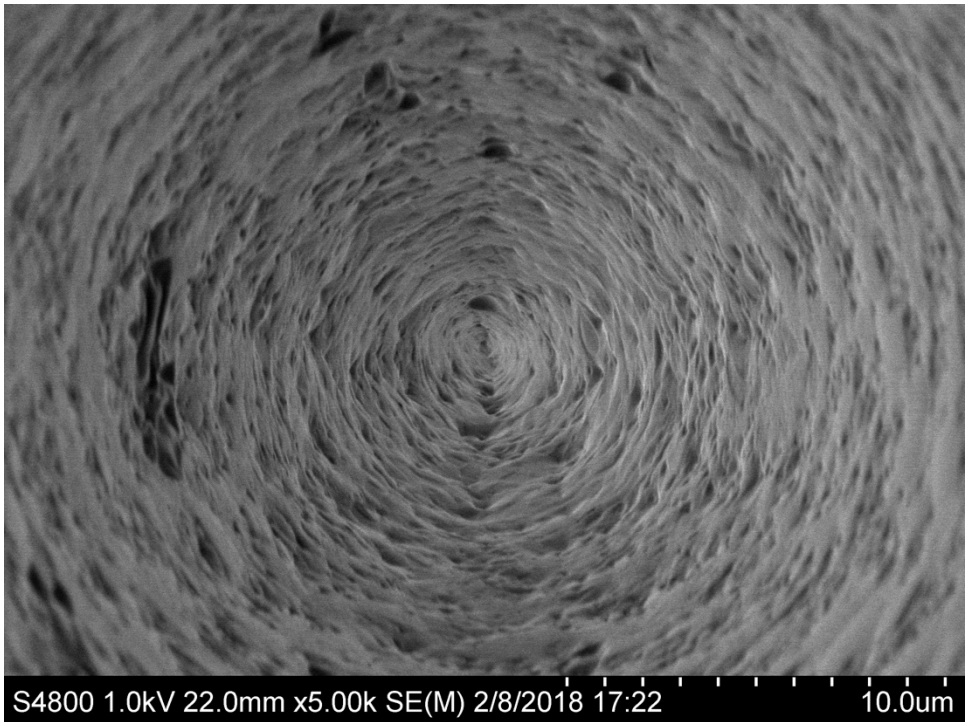

(c)

Figure 3.5: SEM images of the fabricated NSOM probe after 4 hours of chemical etching (a) viewed from the side, (b) viewed from a 45° angle, (c) viewed from the top.

3.5.3 Comparison of Etching Methods

A set of comparative experiments were done by the two etching methods: the meniscus etching (Turner method) and the MST etching. Two pieces of optical fibers of the same length ($70\ \mathrm{mm}$ long) were cut from the optical fiber spool for these experiments. The polymer jacket was stripped from one end of one of the optical fibers over a length of approximately $40\ \mathrm{mm}$, and the stripped end was cleaned by wiping with KimWipes soaked in methanol. Two optical fibers that were prepared in this manner were then placed on the Teflon holder side by side less than half a millimeter apart using a custom-made attachment. Several etching experiments were conducted by changing the etching

time in order to compare the two etching methods at different etching times. Afterwards, SEM images of the two optical fibers were taken together without removing the fibers from the custom-made attachment.

3.5.4 Probes for Sensing Applications

Sensing applications required laser light to be coupled into the end of the optical fiber opposite to the NSOM probe. Therefore, about 1-meter-long optical fibers were cut from the fiber spool to make probes for the sensing applications. As before, the polymer jacket was stripped over a length of about $40\ \mathrm{mm}$ from one end of this optical fiber and cleaned by wiping with KimWipes soaked in methanol. The stripped end was attached to the Teflon holder, and the rest of the optical fiber was rolled up into a 6-inch diameter coil and taped to the other end of the Teflon holder. The stripped fiber end was etched for 4 hours to fabricate the NSOM probes.

3.5.5 Surface Cleaning

The core and the cladding of an optical fiber are composed of silica ($\mathrm{SiO_2}$). Fluorescent organic compounds can be bound to the silica surfaces of the optical fibers by means of silane coupling agents. Covalent attachment of silane coupling agents (or, in other words, silanization of the silica surfaces) with optimal uniformity and reproducibility requires the silica surfaces to be free from any contaminants and reactive hydroxyl groups on the surfaces of the silica have to be activated.[4,5] There are eight

methods found in the literature for cleaning the silica surfaces and activating their hydroxyl groups, as shown in Table 3.1. Method 2, which produced the smallest water contact angle, was utilized for cleaning the cleaved optical fiber (with flat end) and the NSOM probe (with tapered end) surfaces and making those surfaces hydrophilic before silanization of the surfaces.[4]

Table 3.1: Different chemical cleaning methods for glass surfaces used by Cras et al. Reprinted with permission from Ref. 4. Copyright 1999 Elsevier.

Method	Steps
1	30 min in 1:1 MeOH:HCl Rinse in H_2O, dry under N_2
2	Method 1 + additional incubation (30 min) in conc. H_2SO_4 Rinse in H_2O, dry under N_2
3	Method 2 + additional incubation (30 min) in 100°C H_2O Dry under N_2
4	5 min in 1:1:5 NH_4OH:H_2O_2 (30%):H_2O at 80°C Rinse in H_2O, dry under N_2
5	Method 4 + additional incubation (5 min) in 1:1:5 HCl:H_2O_2 (30%):H_2O at 80°C Rinse in H_2O, dry under N_2
6	30 min in 10% KOH in isopropanol Rinse in H_2O, dry under N_2
7	20 min in 1 M NaOH Rinse in H_2O, dry under N_2
8	Method 7 + additional incubation (30 min) in piranha (1:2 H_2O_2:H_2SO_4) Rinse in H_2O, dry under N_2

The cleaved optical fibers and the NSOM probes were clamped to a custom-made stainless-steel holder placed in a small glass vial containing $2\ \mathrm{mL}\ \mathrm{MeOH/HCl}$ [1 : 1 by volume] for 30 minutes. Then it was rinsed 3 times with ultrapure water and dried with $\mathrm{N_2}$. Next it was placed in another small glass vial containing $2\ \mathrm{mL}$ conc. $\mathrm{H_2SO_4}$ for another 30 minutes. Afterwards, it was rinsed 3 times with ultrapure water and again dried with $\mathrm{N_2}$. Performing this cleaning procedure produces hydroxyl groups on the silica surfaces as shown in Figure 3.6.

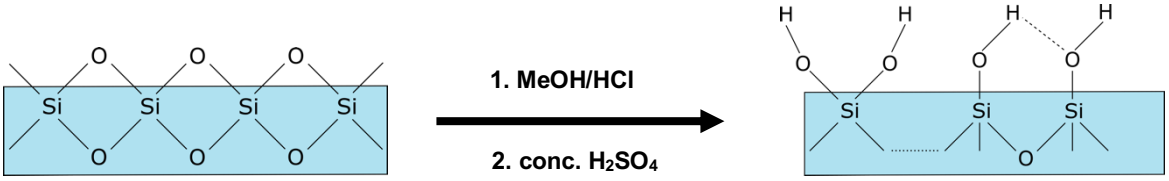

Figure 3.6: Schematic representation of activating the reactive hydroxyl groups on the silica surfaces.

3.5.6 Silanization

Silane coupling agents usually contain hydrolyzable groups and nonhydrolyzable organofunctional groups. Reactive silanol groups, which are formed when the hydrolyzable groups such as alkoxy, acyloxy, etc., of the silane coupling agents undergo hydrolysis, and can condense with other silanol groups of inorganic solid compounds like those found on the activated silica surfaces to form siloxane linkages. Organic compounds, on the other hand, react with the nonhydrolyzable organofunctional groups of the silane coupling agents to form a covalent bond. Activated silica surfaces can be treated with either a solution or vapor of silane coupling agents.

APTES vapor was utilized for the silanization of the cleaved optical fibers or the NSOM probes that were cleaned. The cleaved optical fibers or the NSOM probes were clamped to a custom-made holder and placed in an aluminum enclosure and preheated inside the oven to $165°C$. Then, 1-inch diameter glass wool bundles were placed on each side of the holder and a few drops of APTES were put on each of the bundles and the encloser was closed. Next, the enclosure was left in the oven for 15 minutes at $165°C$ so that the APTES could vaporize and deposit on the surfaces.[6] Then, the enclosure was opened to let the APTES vapor escape, and the glass wool bundles were removed. Two new glass wools bundles soaked in ultrapure water were then placed inside the enclosure, which was then closed and left in the oven for 30 minutes at $165°C$. After that, a mild vacuum was pulled to complete the coupling process. The silica surfaces, after the silanization process with APTES, contain amine terminals as shown in Figure 3.7.

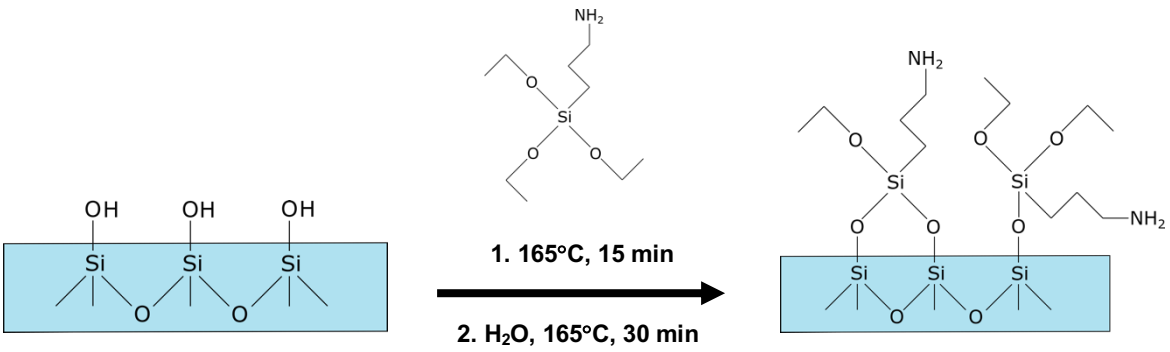

Figure 3.7: Schematic representation of silanization of the silica surfaces with APTES.

3.5.7 Fluorophore Attachment

Amine-terminated silanized cleaved optical fibers or NSOM probes can form covalent bonds with fluorophores having carboxy or isothiocyanate groups through a simple one-step organic reaction at room temperature and atmospheric pressure. Simple one-step reactions at room temperature and atmospheric pressure are especially advantageous for NSOM probes to protect the very fine and delicate nano scale tip of the probe from damage during the reaction. The viability of surface functionalization of amine-terminated silanized cleaved optical fibers and NSOM probes was tested using Rhodamine B, a fluorophore with a carboxy group, by applying the Steglich esterification method.[7,8]

In this experiment, the NSOM probes were fabricated from $70\ \mathrm{mm}$ long optical fibers. But the cleaved optical fibers were $50\ \mathrm{mm}$ long and the polymer jacket was stripped from one end over a length of approximately $20\ \mathrm{mm}$. The cleaved optical fibers or the NSOM probes silanized with APTES were clamped to a custom-made aluminum holder and placed in a plastic vial. A $10\ \mathrm{mL}$ solution mixture was prepared that contained $1.0\ \mathrm{mM}$ Rhodamine B, $1.0\ \mathrm{mM}$ EDC and $0.2\ \mathrm{mM}$ DMAP in DCM as the solvent. The solution mixture was added to the vial; the vial was then capped and wrapped with aluminum foil. Afterwards, the vial was left in the dark overnight to complete the functionalization reaction (Figure 3.8). The next morning, the cleaved optical fibers or the NSOM probes were taken out of the vial and then first rinsed with fresh DCM, followed by rinsing with acetone. They were then washed three times with ultrapure water, dried with

N_2, and imaged under the optical microscope in fluorescence mode using $514\ \mathrm{nm}$ laser excitation.

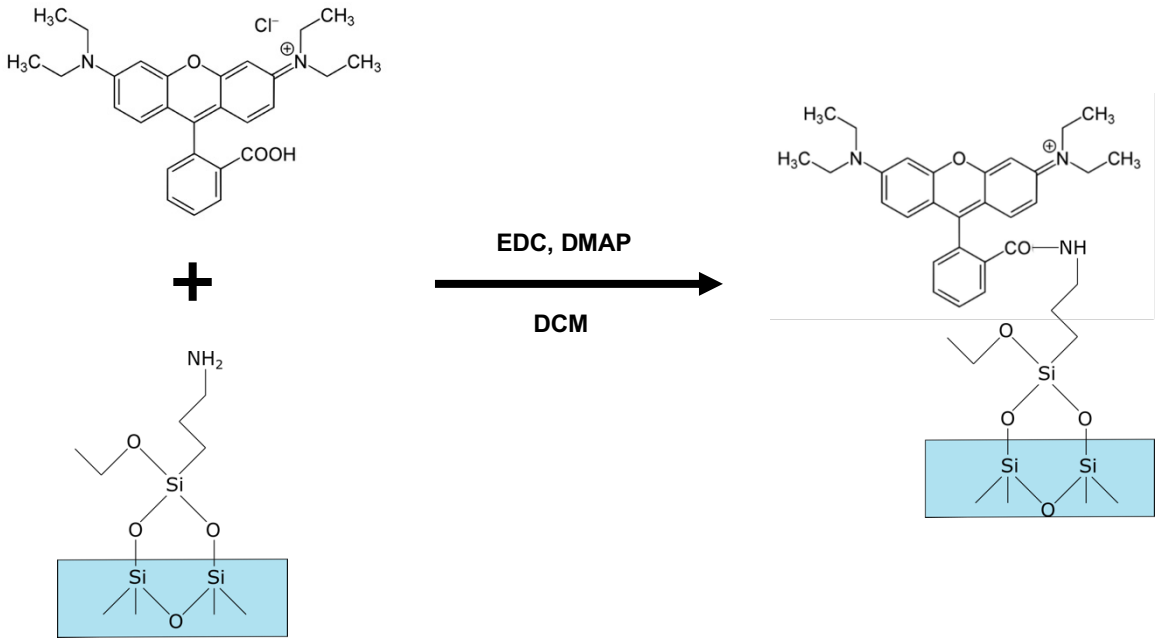

Figure 3.8: Schematic representation of covalent attachment of Rhodamine B to the amine terminal of the silanized silica surfaces by means of the Steglich esterification process.

NSOM probes functionalized with FITC were employed for the sensing applications. FITC, a fluorophore with an isothiocyanate group, forms a thiourea linkage with the amine terminal of the silanized NSOM probes. For this experiment, the NSOM probes were fabricated from $1\ \mathrm{m}$ long optical fibers and silanized with APTES. The silanized NSOM probes were then clamped to a custom-made aluminum holder, which was placed in a plastic vial. A $4\ \mathrm{mL}$ solution of $1.0\ \mathrm{mM}$ FITC was prepared using absolute EtOH as the solvent. The solution was then added to the vial and the vial was wrapped

with aluminum foil. Afterwards, the vial was left in the dark overnight for the functionalization reaction to complete (Figure 3.9).

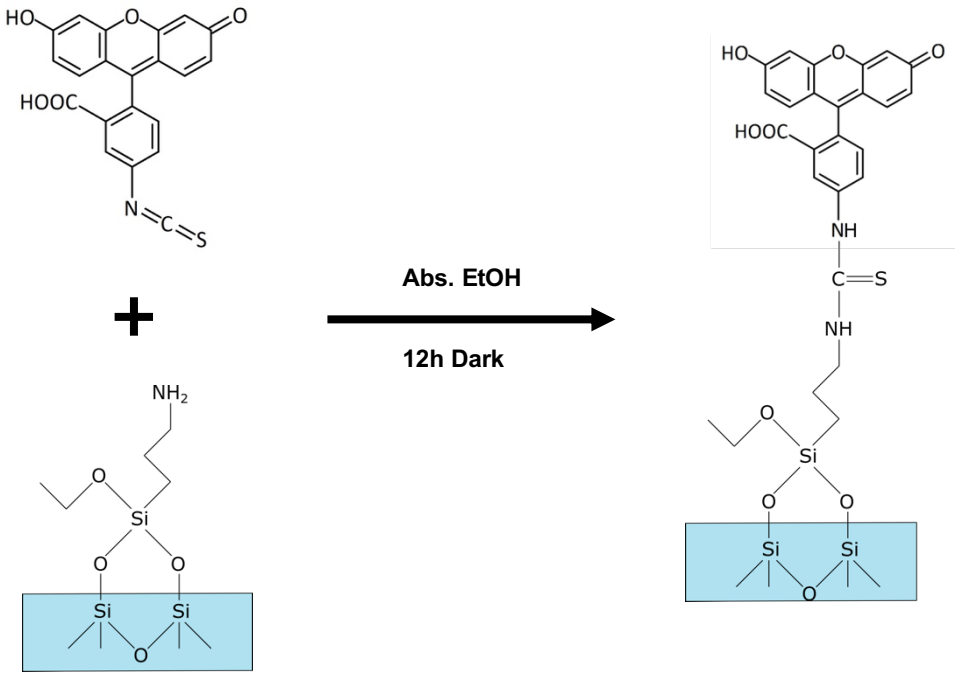

Figure 3.9: Schematic representation of covalent attachment of FITC to the amine terminal of the silanized silica surfaces.

The next morning, the NSOM probes were taken out of the vial and first rinsed with fresh EtOH, then rinsed with acetone. They were then washed three times with ultrapure water, dried with N_2, and imaged under the optical microscope in fluorescence mode using $488\ \mathrm{nm}$ laser excitation.

3.5.8 Detection with Nanosensor Probe

NSOM probes functionalized with FITC were used as a nanosensor for pH and for detecting metal ions in the respective solution drops. FITC will fluoresce when excited with $488\ \mathrm{nm}$ laser light. The $488\ \mathrm{nm}$ emission from an argon ion laser was directed by mirrors and coupled into the end of the fiber optic cable on the laser table side (Figure 3.10).

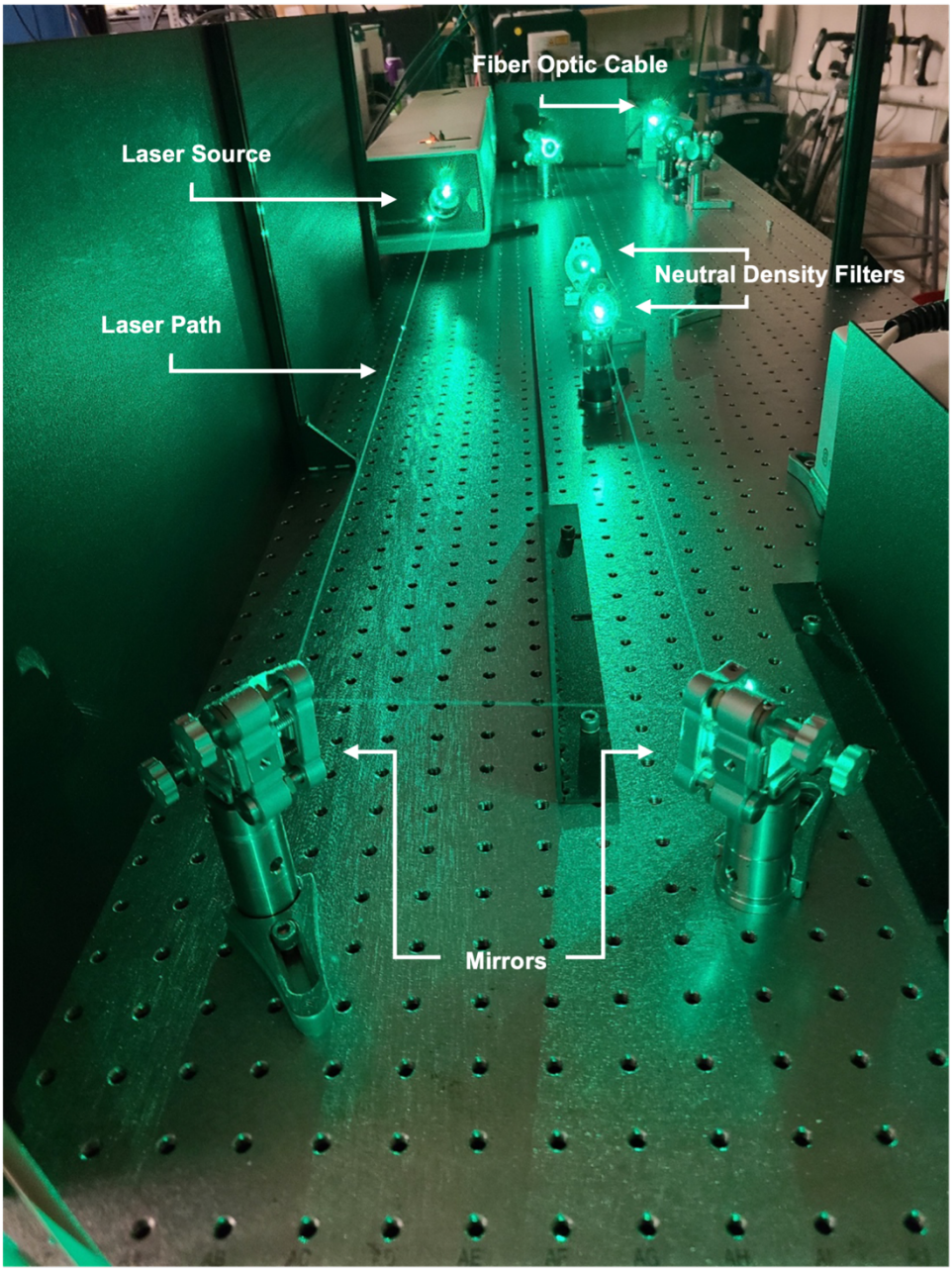

Figure 3.10: Laser setup for the detection of pH and metal ions with the FITC functionalized NSOM probes.

The laser light exiting from the other end of the fiber optic cable (on the microscope table) was directed by mirrors and passed through a noise eater before being coupled into the

opposite end of the optical fiber containing the FITC functionalized NSOM probe (Figure 3.11).

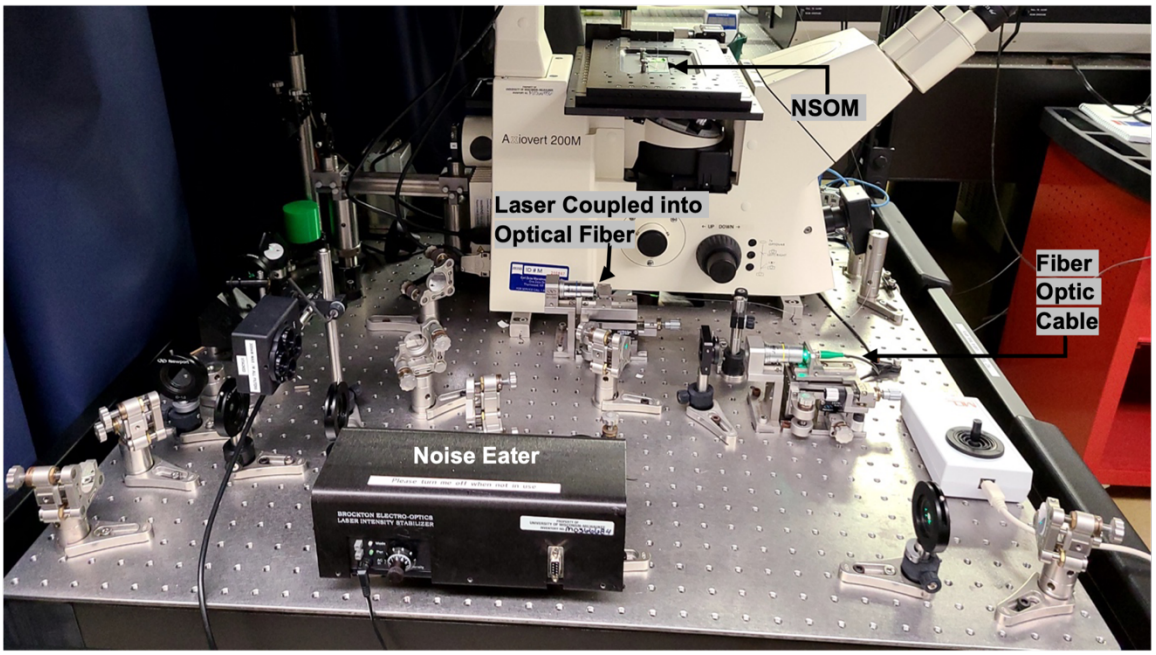

Figure 3.11: Experimental setup with optical microscope for the detection of pH and metal ions with the FITC functionalized NSOM probes.

The FITC functionalized NSOM probe is clamped to the custom-made sample stage (Figure 3.12) so that the microscope coverslip can be removed from underneath. The tip of the NSOM probe is placed very close to the coverslip without touching it, and sample solution is dropped on top of the tip so that the tip is immersed in the droplet.

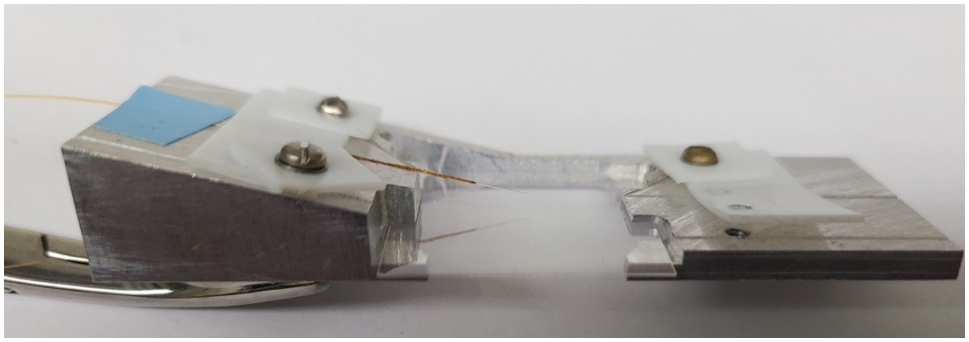

Figure 3.12: FITC functionalized NSOM probes clamped to the custom-made sample stage with removable coverslip to hold sample solution drops.

For the pH detection experiments, solutions with pH > 7 were prepared from NaOH pellets whereas solution with pH < 7 were prepared from conc. HCl. Ultrapure water was used as a pH 7 solution for these experiments. For the metal ion detection experiments, various concentrations of $\mathrm{FeCl_3}$ solution and $\mathrm{CuSO_4}$ solution were prepared.

References

(1) Stöckle, R.; Fokas, C.; Deckert, V.; Zenobi, R.; Sick, B.; Hecht, B.; Wild, U. P. High-Quality near-Field Optical Probes by Tube Etching. *Appl. Phys. Lett.* **1999**, *75* (2), 160–162. https://doi.org/10/d7m8jt.

(2) Nikbakht, H.; Latifi, H.; Oraie, M.; Amini, T. Fabrication of Tapered Tip Fibers With a Controllable Cone Angle Using Dynamical Etching. *J. Light. Technol.* **2015**, *33* (23), 4707–4711. https://doi.org/10/gmzqf4.

(3) Shi, J.; Qin, X. R. Formation of Glass Fiber Tips for Scanning Near-Field Optical Microscopy by Sealed- and Open-Tube Etching. *Rev. Sci. Instrum.* **2005**, *76* (1), 013702. https://doi.org/10.1063/1.1823778.

(4) Cras, J. J.; Rowe-Taitt, C. A.; Nivens, D. A.; Ligler, F. S. Comparison of Chemical Cleaning Methods of Glass in Preparation for Silanization. *Biosens. Bioelectron.* **1999**, *14* (8–9), 683–688. https://doi.org/10.1016/S0956-5663(99)00043-3.

(5) Dey, T.; Naughton, D. Cleaning and Anti-Reflective (AR) Hydrophobic Coating of Glass Surface: A Review from Materials Science Perspective. *J. Sol-Gel Sci. Technol.* **2016**, *77* (1), 1–27. https://doi.org/10.1007/s10971-015-3879-x.

(6) Fenske, T. A Study in Molecular Recognition: Synthesis of a β-Sheet Mimic & Quantitation of Metal Ions in Aqueous Solutions Through Solid Supported Semi-Selective Chemosensors. 191.

(7) Neises, B.; Steglich, W. Simple Method for the Esterification of Carboxylic Acids. *Angew. Chem. Int. Ed. Engl.* **1978**, *17* (7), 522–524. https://doi.org/10.1002/anie.197805221.

(8) Jordan, A.; Whymark, K. D.; Sydenham, J.; Sneddon, H. F. A Solvent-Reagent Selection Guide for Steglich-Type Esterification of Carboxylic Acids. *Green Chem.* **2021**, *23* (17), 6405–6413. https://doi.org/10.1039/D1GC02251B.

CHAPTER 4

Aperture NSOM Probe

4.1 Overview

This chapter focuses on the realization of the first objective as stated in the introduction, namely “To determine the cone angle of the near-field scanning optical microscopy (NSOM) probe during the chemical fabrication process by conducting a time-dependent study”. The chapter starts with a discussion of some important concepts of aperture NSOM probes related to probe design, factors affecting power output, and ways to improve efficiency. After that, different chemical etching methods to fabricate probes are presented, and their features and the key differences are briefly explained. Next, the experimental results are discussed in four parts: measuring the cone angles with varying etching time, using image analysis techniques to verify cone angle measurements, analyzing the trend in cone angle progression with etching time, and comparing the etching process of two chemical etching methods. Lastly, the findings from the results are summarized in the concluding remarks.

4.2 Aperture Probe Design

In the aperture NSOM configuration, the intensity of the nanoscale light source, which solely depends on the dimensions and quality of the aperture probe, plays a critical role in nanoscopic imaging. Because optical fibers have high collection and transmission efficiency and light can be easily guided through the optical fibers, it has become extremely common to use optical fibers for making aperture probes. An aperture probe is created by first tapering the optical fiber, having a diameter of a few hundreds of microns, to a conical shape with an apex some tens of nanometers in diameter. However, this cone-shaped end of the optical fiber loses the light guiding ability, because light leakage

occurs as the diameter decreases. To prevent this, a reflective metal coating is applied to the side walls of the tapered end to prevent this phenomenon, which not only helps to guide the light but also forms an aperture at the apex. However, the apertures thus formed usually have irregularities. Therefore, the end is milled flat using a focused ion beam (FIB) to create a uniform aperture NSOM probe (Figure 4.1).

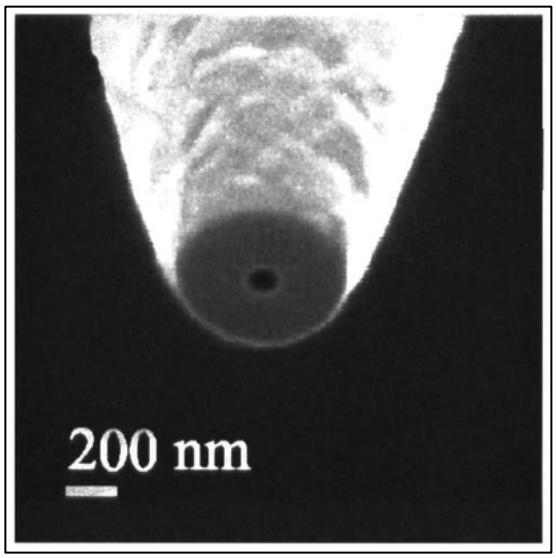

Figure 4.1: SEM image taken by Veerman et al. of an aluminum coated aperture NSOM probe where the end has been milled flat using FIB. Adapted with permission from Ref. 1. Copyright 1999 Elsevier.

4.3 Aperture Probe Efficiency

The efficiency of the aperture probe in near-field microscopy depends on: (a) the spot size determined by the aperture diameter, and (b) the light intensity at the aperture.[2] The resolving power of the aperture probe increases with decreasing diameter of the aperture, and the highest resolution is achieved when the smallest realistically possible diameter of the aperture has been reached. On the other hand, smaller apertures lead to reduced light transmission, which negatively affects the irradiance and signal-to-noise

ratio for the sample. The maximum irradiance is achieved when the light intensity reaches the damage threshold of the metal coating on the probe. The power output of an aperture probe is reliant on both the aperture size and the tapered region of the probe.

4.3.1 Aperture Size

The transmission coefficient of an aperture probe for a specified wavelength λ is expressed by the ratio of the light power transmitted by the aperture to the light intensity inside the fiber.[2] Bethe was first to formulate the relationship between the transmission coefficient and the diameter of a subwavelength hole in an infinitely thin, perfectly conducting screen, which was later corrected for errors in the expression for the near field by Bouwkamp. According to the Bethe-Bouwkamp model, the transmission coefficient of a subwavelength hole is proportional to $(a/\lambda)^4$, where a is the diameter of the aperture.[2–4] This model suggests that if the diameter of the aperture of the NSOM probe is reduced from $100\ \mathrm{nm}$ to $10\ \mathrm{nm}$ to increase the spatial resolution, the light intensity will drop by a factor of 10,000, which could result in signals from the sample that are indistinguishable from the noise due to the light source and the detector.[4]

4.3.2 Tapered Region

The fate of all the modes of the optical waveguides for an aluminum coated dielectric core with a diminishing core radius were calculated by Novotny and Hafner.[5] Their results shows that the waveguides inside an aluminum coated tapered core run into cutoff one after another as the core diameter gradually decreases until only the final HE_{11} mode is still propagating. The pure HE_{11} mode at a wavelength of $488\ \mathrm{nm}$ propagates

inside the aluminum coated ($\varepsilon_{alu} = -34.5 + i8.5$) dielectric core ($\varepsilon_{core} = 2.16$) of the tapered probe between inner core diameters of $250\ \mathrm{nm}$ and $160\ \mathrm{nm}$ (Figure 4.2).[2]

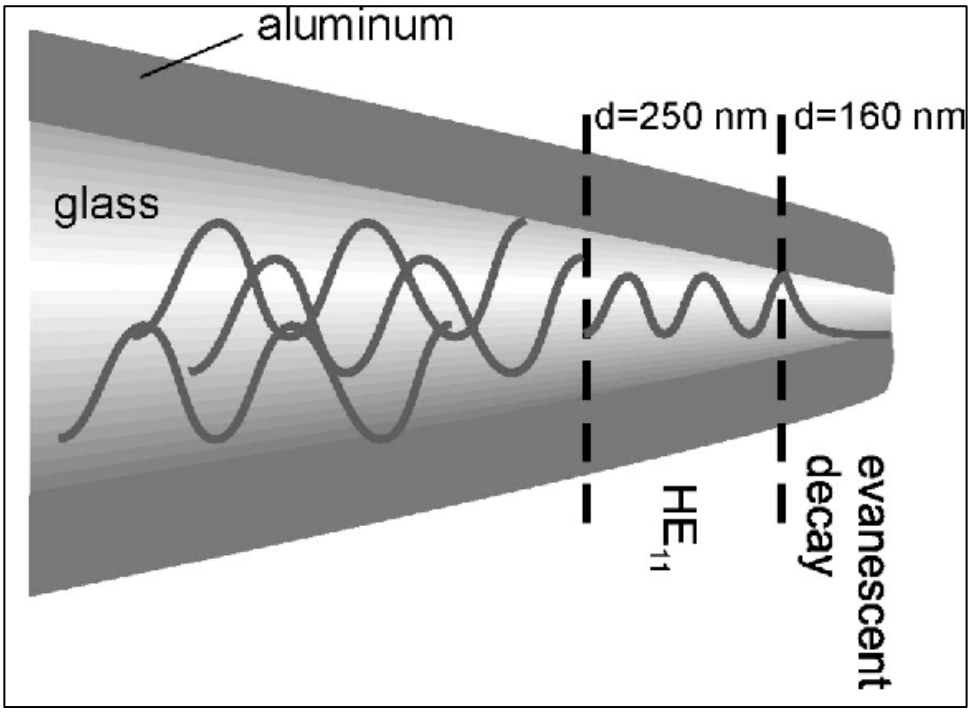

Figure 4.2: Mode propagation of light with a wavelength of $488\ \mathrm{nm}$ inside a tapered metal-coated optical fiber illustrated by Hecht et al. Reprinted with permission from Ref. 2. Copyright 2000 American Institute of Physics.

The tiny fraction of the input power retained in the still-propagating HE_{11} mode (along with other factors) results in the power output of the aperture probe, whereas the large part of the power not contained in propagating modes is either reflected back up the fiber from the taper region or is lost due to absorption by the aluminum coating.[2,6] The propagating HE_{11} mode also runs into cutoff and decays exponentially below the inner diameter of $160\ \mathrm{nm}$. The distance between the HE_{11} cutoff diameter and the aperture plane, which controls the final power output, is determined by the cone angle of the taper.[2]

4.3.3 Improving Efficiency

Aperture NSOM probes have a low throughput problem (for etched fibers: $10^{-3} - 10^{-4}$, for pulled fibers: 10^{-6}) which makes it difficult to obtain nano-scale, high resolution images and various efforts have been made to overcome this problem.[4] One such endeavor looked into the possibility of increasing the input power that could result in higher output power at the apex of the probe. But because most of the input power is absorbed by the aluminum coating in the tapered region, injecting excessive power leads to extreme local heating at the tapered end, which can destroy the aluminum coating and the tip or cause heat transfer to the sample.[4,6] Another possible way to solve the low throughput problem is to increase the aperture diameter of the probe (Figure 4.3), which would produce greater output power; however, the probe would lose its resolving power at the same time. The most practical approach to the low throughput problem is to decrease the distance between HE_{11} cutoff diameter and the aperture plane by increasing the cone angle (Figure 4.3) of the tapered probe. In addition to an increase in throughput with increasing cone angles, a study showed that the temperature coefficients dropped from $60\ \mathrm{K/mW}$ for a tip with a narrow cone angle to $20\ \mathrm{K/mW}$ for a large cone angle tip when measured approximately $70\ \mu\mathrm{m}$ away from the apex of the probe.[6,7]

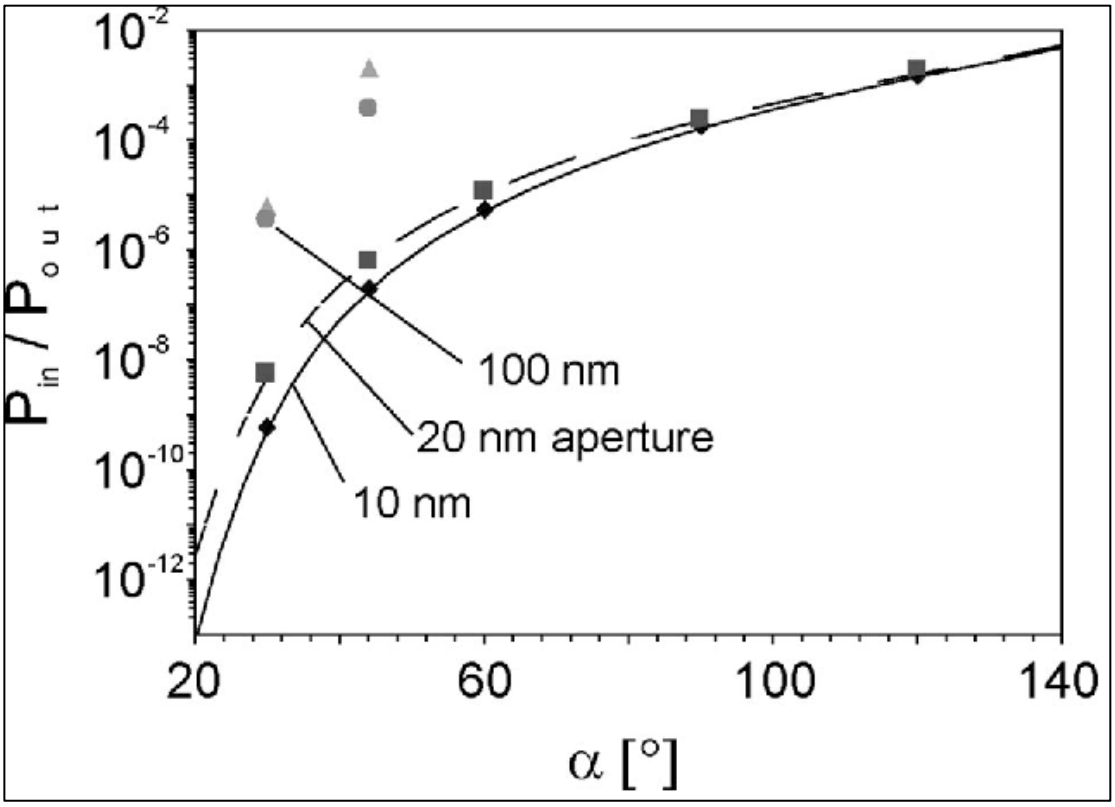

Figure 4.3: Transmission coefficient of an aperture NSOM probe as a function of the cone angle α of the tapered probe calculated by Hecht et al. Reprinted with permission from Ref. 2. Copyright 2000 American Institute of Physics.

4.4 Chemical Fabrication Method

The “heating and pulling” method produces long NSOM tips with small cone angles. Producing tips with large cone angles is not possible with this method, but one can effortlessly produce tips with large cone angles using the chemical etching method. Also, the tips produced by the “heating and pulling” method lose the original properties of the core and the cladding because the optical fiber melts during heating. In the chemical etching method, however, the etching solution eats away the cladding first and then corrodes the core during the etching process, which leaves the original properties of the core and the cladding intact. We pursued the chemical etching method to fabricate NSOM

probes because of the aforementioned advantages of the chemical etching method over the “heating and pulling” method.

4.4.1 Meniscus Etching

The first chemical etching method of optical fibers, known as the “Turner method” or “Meniscus etching”, was proposed by D. R. Turner.[8] This method uses a two-phase liquid system consisting of hydrofluoric acid (HF) as the etching solution at the bottom and a protective overlayer of organic oil to etch bare optical fibers stripped of any protective polymer jacket .[9,10] The height of the initially formed meniscus at the liquid-liquid and liquid-solid interface gradually decreases due to surface tension as the fiber diameter is reduced by the etchant and a taper is formed (Figure 4.4).[8–10]

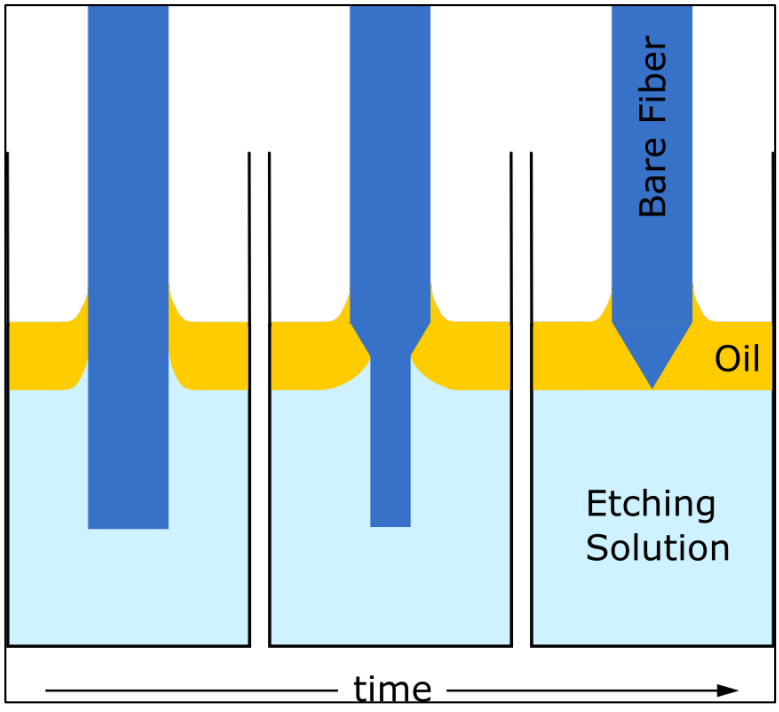

Figure 4.4: Schematic representation of fabrication NSOM probes from optical fiber using the meniscus etching or the Turner method of chemical etching.

This chemical etching method can create NSOM probes with wide-ranging large cone angles which results in higher optical throughput. However, the tip shape and quality are influenced by environmental factors such as vibrations, temperature, drifts, etc., that can influence the height of the meniscus during the etching process, which results in considerable roughness of the tip surface and uncertainty in producing comparable tips every time.[8,10] Once the tip has formed the cone angle becomes larger, but the tip quality degrades with increasing etching time. The etching process stops when the tip reaches the protective oil layer and cone angles up to $41°$ have been reported for the Turner method.[10,11]

4.4.2 Tube Etching

The tube etching method, developed in the late 1990s based on the Turner method, removed the effects of the environment in the tip making process by not stripping the protective polymer coating from the optical fiber before dipping it into HF solution for etching (Figure 4.5).[8,10,12] In this method, etching by HF happens entirely inside a hollow cylinder formed by the polymer jacket of the optical fiber.

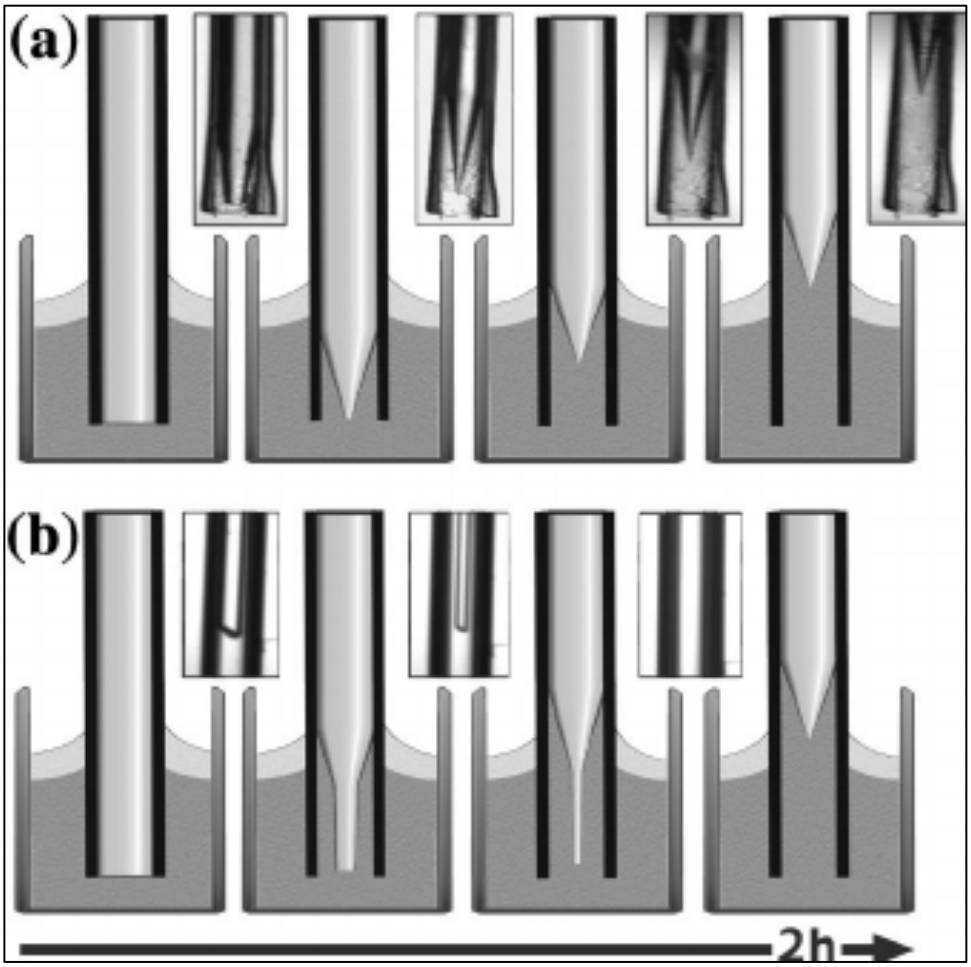

Figure 4.5: Taper formation by tube etching for different fiber polymer coatings illustrated by Stöckle et al.: (a) HF impermeable coating and (b) HF permeable coating. The insets show video frames below the meniscus. Reprinted with permission from Ref. 10. Copyright 1999 American Institute of Physics.

With this method, tip formation occurs according to Figure 4.5(a) if the polymer jacket is impermeable to HF but looks more like Figure 4.5(b) if the polymer jacket is permeable to HF. Lateral diffusion through the polymer jacket, micro-convection inside the tube (Figure 4.6), transient capillary action, removal of reaction products by gravity, and geometrical constraints at the open end of the tube - all of these play a role in the tip formation and the etching process in this method. Once a tip is formed, the tip only shortens inside the tube while the cone angle and the surface quality do not change with

increasing etching time. The authors found the tube etching process to be “self-limiting” with cone angles between $18°$ and $35°$ depending on the type of optical fiber and HF concentration used.[10]

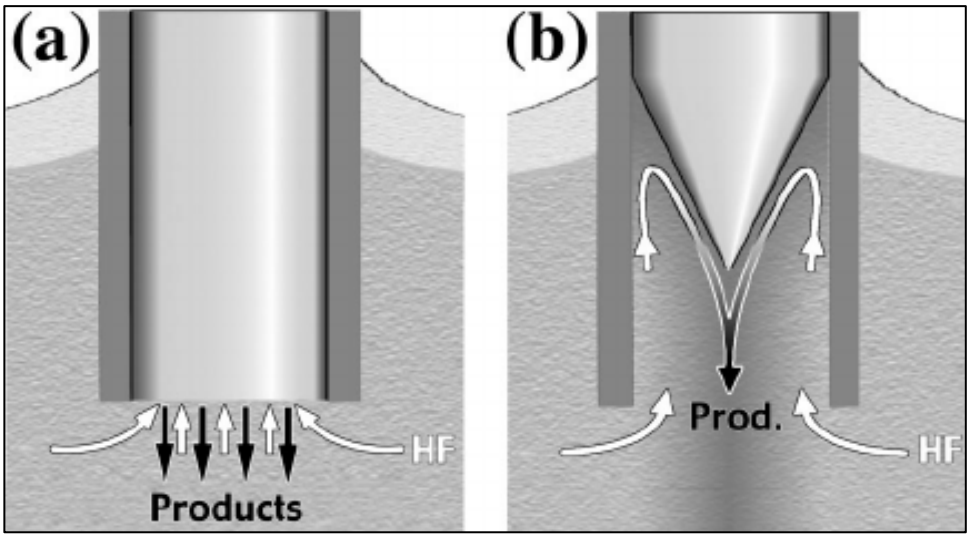

Figure 4.6: Schematic of the convection mechanism proposed by Stöckle et al. in tube etching: (a) initial diffusion-controlled etching and (b) convection-controlled tip formation inside the tube. Reprinted with permission from Ref. 10. Copyright 1999 American Institute of Physics.

4.4.3 Sealed-tube Etching

In 2004, a technique called “Sealed-tube etching” was reported by Shi & Qin where the bottom end of the optical fiber was sealed with HF-impermeable plastic so that only lateral diffusion of HF through the protective polymer coating controls the etching process inside the tube (Figure 4.7).[11]

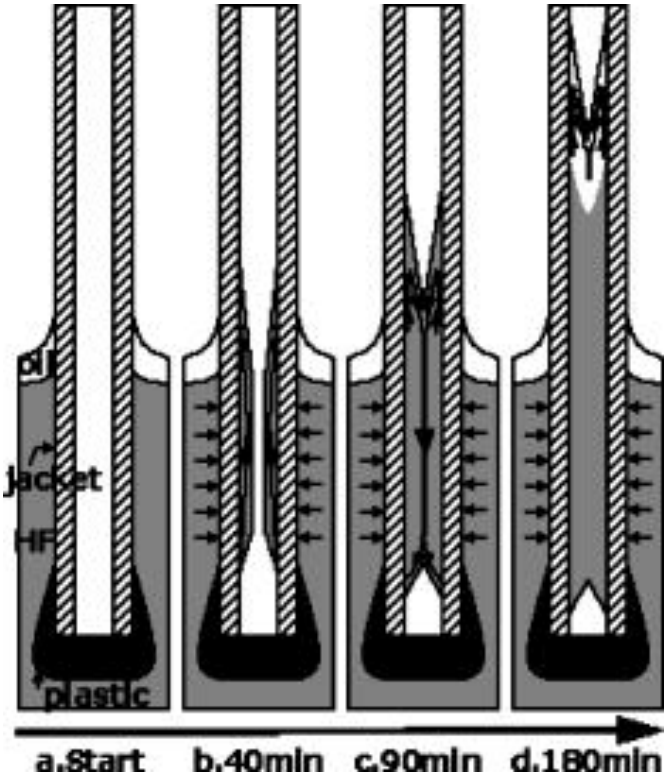

Figure 4.7: Schematic diagram of the etching process in a sealed tube illustrated by Shi and Qin. Reprinted with permission from Ref. 11. Copyright 2005 American Institute of Physics.

The authors suggested that the sealant not only blocks the direct diffusion of HF but also blocks removal of the heavier etching products through the bottom end of the fiber. The buildup of the etching products inside the tube slows down the etching reaction at the bottom and pushes the diffused HF etchant levels up. The author also suggested that HF creeps up along the tube to etch the base of the inverted cone-shaped upper tip and flows down together with the etching products along the tip to its apex once the initial upper tip is formed. This process, described as a second kind of convection, causes the shortening of the tip without changing the tip shape with typical cone angles of about $40°$.[11]

4.4.4 Modified Sealed-tube Etching

Christine Carlson from our research group investigated for a new sealant to replicate the sealed-tube etching method because the previous researchers were vague about the plastic used as a sealant in their article. Using beeswax and fast curing two-component epoxies as a sealant, it was found that any slight variations during processing and applying these sealants to the fiber resulted in inconsistent tip formation when producing optical fiber probes. The “Modified Sealed-tube (MST) etching” developed in-house uses a layer of mercury at the bottom of a Teflon beaker containing the HF acid solution as the sealant (Figure 4.8). The layer of mercury will automatically seal the bottom end of the optical fiber when it is submerged into the HF and the mercury.

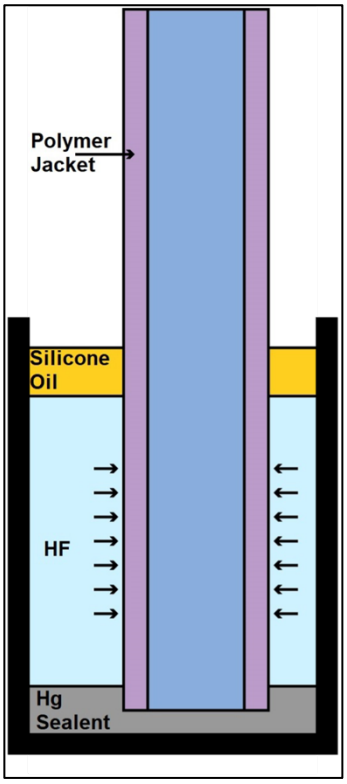

Figure 4.8: Schematic representation of the arrangements for the in-house developed modified sealed-tube (MST) etching method to fabricate NSOM probes.

Mercury is an excellent sealant because not only is it dense enough to seal the fiber end and impede capillary action but it also is both resistant and impermeable to HF as well as chemically unreactive towards the optical fiber and its polymer coating.[13] We used the MST etching method to fabricate NSOM probes and measured their cone angles as a function of the etching time.

4.5 Experimental Results

4.5.1 Time-varying Cone Angle Measurements

The primary goal for developing the chemical etching method was to create NSOM probes with wide-ranging large cone angles so that higher optical throughput can be achieved. The maximum cone angles attained by the chemical etching methods other than the MST etching have been reported in the literature. One of the objectives of this research project was to fabricate different NSOM probes at varying etching times and to determine the time required to obtain the largest (i.e., optimal) cone angle. We etched optical fibers with etching times from 60 to 180 minutes and determined that the initial cone is formed after 160 minutes. It was observed that cone angles gradually became larger as the etching time was increased to 240 minutes. ImageJ has an angle measurement tool which was used to measure the cone angles from the original SEM images of the NSOM probes (Figure 4.9).

(a)

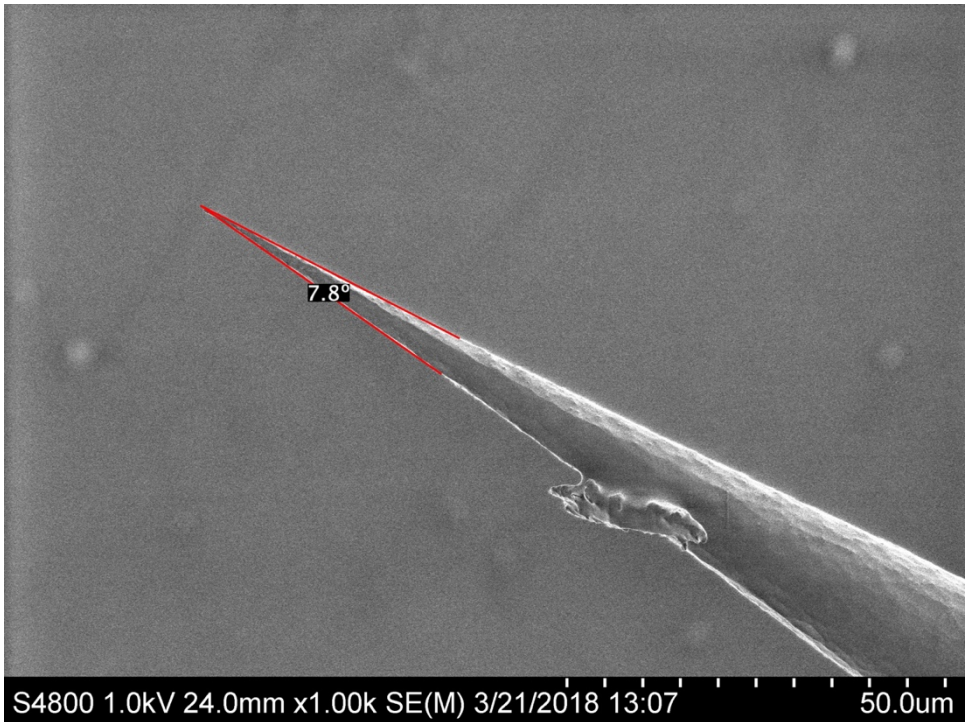

(b)

Figure 4.9: (a) Angle measurement tool in Fiji software, (b) Cone angle measured from the original SEM image of a NSOM probe using Fiji software.

All the other tube etching methods claimed the etching process to be “self-limiting”, meaning that the cone angles didn’t change once the tip was established, so we decided to test this by etching fibers for 720 minutes or 12 hours. To our surprise, this resulted in one of the smallest cone angles measured at various etching times, which prompted us to measure all the cone angles between 3 hours and 12 hours etching times at ½ hour

increments. As shown in Table 4.1, after the formation of the initial cone at 160 minutes, there was a trend for cone angles to increase and reach a maximum value after which the cone angles started to decrease again.

Table 4.1: Cone angles of the NSOM probes fabricated with etching time varied in ½ hour increments.

Etching Time (min)	Cone Angle (°)
160	7.8
180	12.8
210	20.8
240	23.3
270	21.0
300	21.7
330	19.2
360	17.9
390	19.5
420	18.9
450	19.7
480	23.4
510	18.1
540	16.1
570	15.3
600	17.4
660	15.9
720	15.4

This trend happened twice, resulting in a minimum value in between the two maxima shaded blue in Table 4.1. We collected a few more data points close to these extreme values with shorter than the ½ hour increments in etching time and created a dataset with all the etching times and cone angle values (see Appendix) for data analysis.

This dataset contained 26 data points, and because handling HF is extremely hazardous and dangerous only a few data points were reported to calculate standard errors as shown in Table 4.2.

Table 4.2: Standard errors calculated for the etching times 160, 240 and 720 minutes.

Etching Time (min)	Standard Error (°)
160	2.497
240	0.575
720	1.321

4.5.2 Validating Cone Angle Measurements

The original SEM images of the NSOM probes did not always have sharp contrast at the probe boundary, which could potentially lead to errors in cone angle measurements. The MATLAB programming platform has a toolbox for image processing, which contains MATLAB apps (self-contained MATLAB programs with a user interface that automates a task or calculation) for image segmentation. The “Image Segmenter” MATLAB app was used to separate the foreground from the background of the original SEM images to obtain a sharper boundary delimiting the NSOM probes. Afterwards, the angle measurement tool of ImageJ was used to measure the cone angles of the probes from the converted images. These latest cone angle measurements were used to cross-check the original cone angle measurements from the original SEM images. Both cone angle measurement techniques gave similar results with small deviations that fall within the margin of error (Figure 4.10).

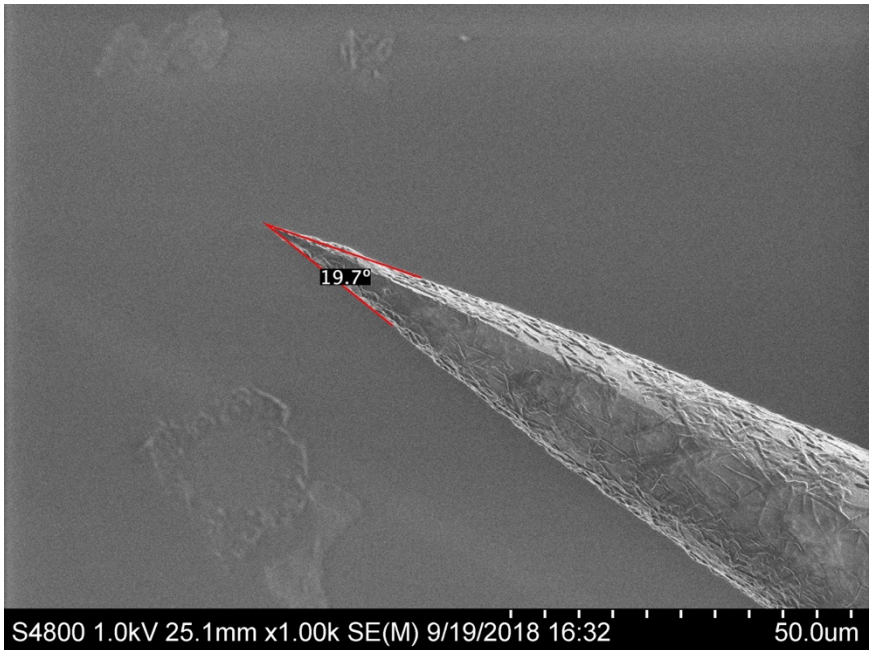

(a)

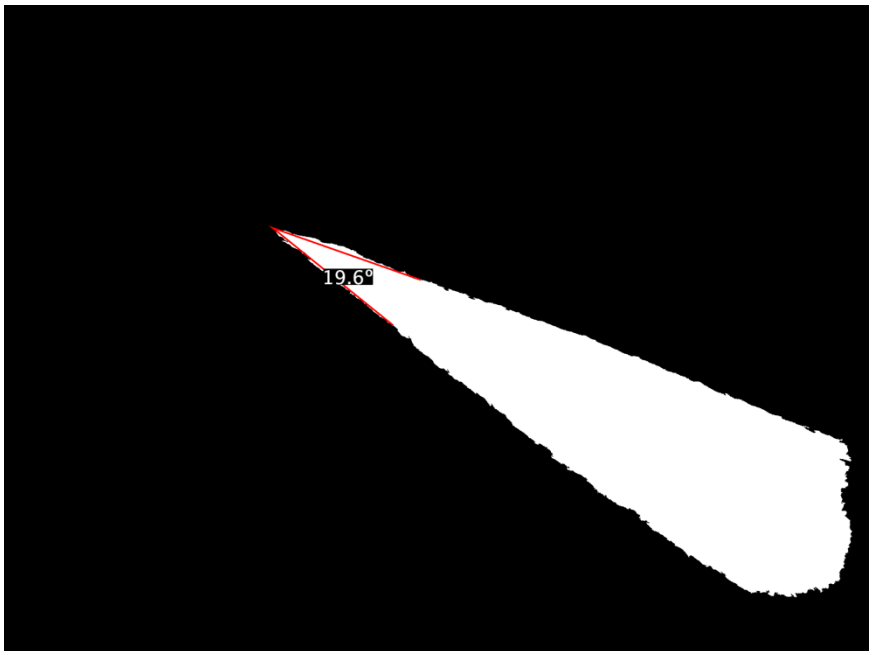

(b)

Figure 4.10: Comparison between (a) measured cone angle from original SEM image and (b) measured cone angle from converted image for an etching time of 450 minutes.

4.5.3 Progression of Cone Angles

Data visualization is a good way to analyze trends in data sets. Once again, we utilized MATLAB to analyze the trends in the progression of cone angles with etching time. At first, we plotted the data from Table 4.1 in MATLAB. Then we used the "Curve Fitting Toolbox" in MATLAB to get the best fit curve from interpolation using cubic spline method (Figure 4.11). The best fit curve shows two peak points and one trough in the curve.

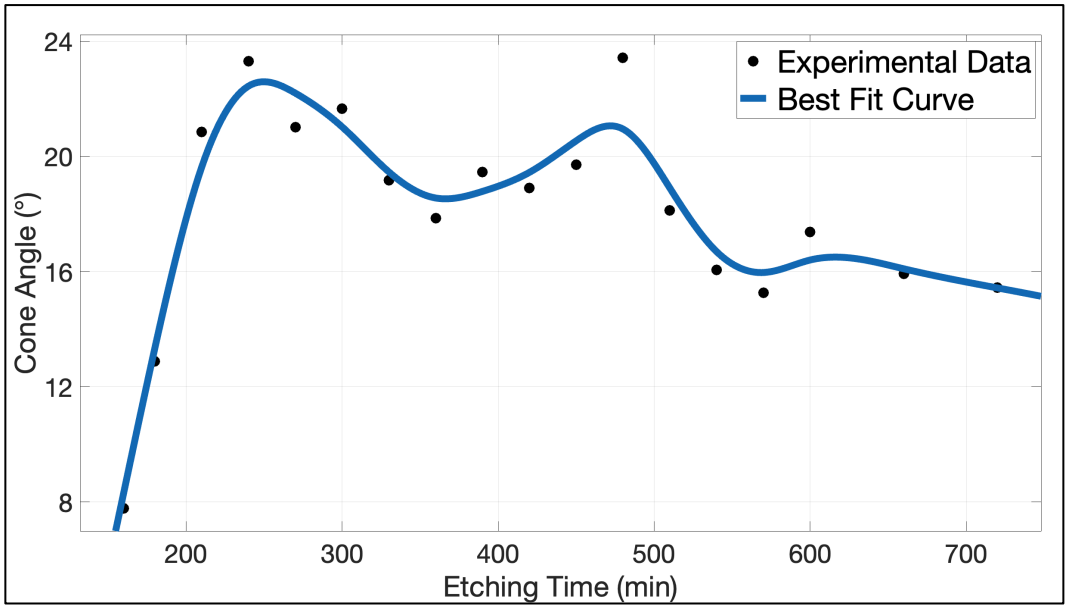

Figure 4.11: Plot of the cone angle data from Table 4.1 and the best fit curve drawn from the data using MATLAB.

This trend is also visible in the actual SEM images placed side-by-side (Figure 4.12).

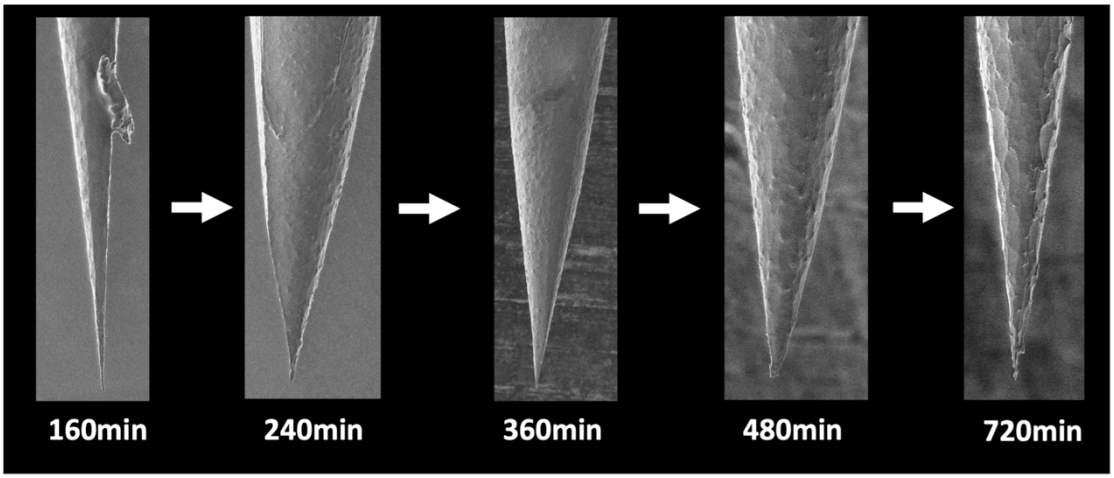

Figure 4.12: Lined up SEM images that show the trend in the progression of cone angles over etching time.

The same approach was taken with the full dataset from Appendix A (Figure 4.13). Although the additional data points near the two peaks and the trough have flattened the second peak somewhat in the best fit curve, its presence is still apparent within the spread of the date.

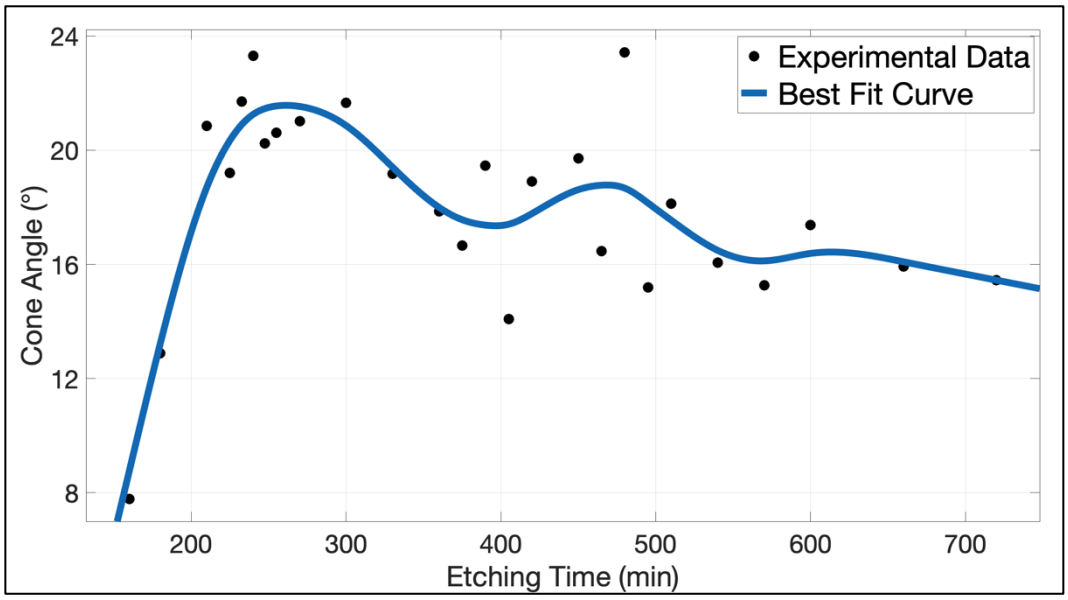

Figure 4.13: Plot of the cone angle data from Appendix A and the best fit curve drawn from the data using MATLAB.

4.5.4 Comparing Meniscus and MST Etching

It is understood from the literature that etching stops when the tip rises above the HF layer in the case of meniscus etching. It is also found in literature that the initial tip is formed above the HF layer in other tube etching methods when optical fibers consisting of HF permeable polymer coating are used. According to our experiments, the initial tip formation took 60 minutes with meniscus etching in 40% HF etching solution at a constant temperature of $20.0°C$ but took 160 minutes with the MST etching. The two etching methods were compared side-by-side using a stripped fiber subjected to the meniscus etching and a non-stripped fiber subjected to the MST etching. We found that for an etching time of 160 minutes, the tip formed by the meniscus etching was vertically positioned “higher up” than the tip formed by the MST etching (Figure 4.14).

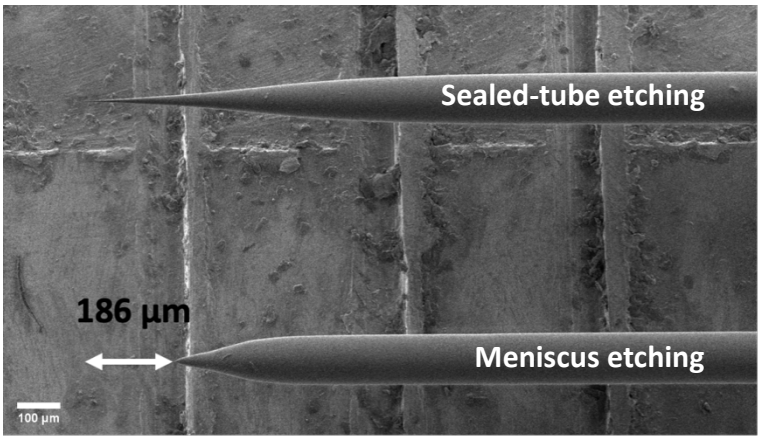

Figure 4.14: Tip formation comparison between meniscus and MST etching after 160 minutes of etching.

We also observed that for an etching time of 720 minutes, the tip became blunt with the meniscus etching, although the etching and tip shortening continued with the MST etching (Figure 4.15).

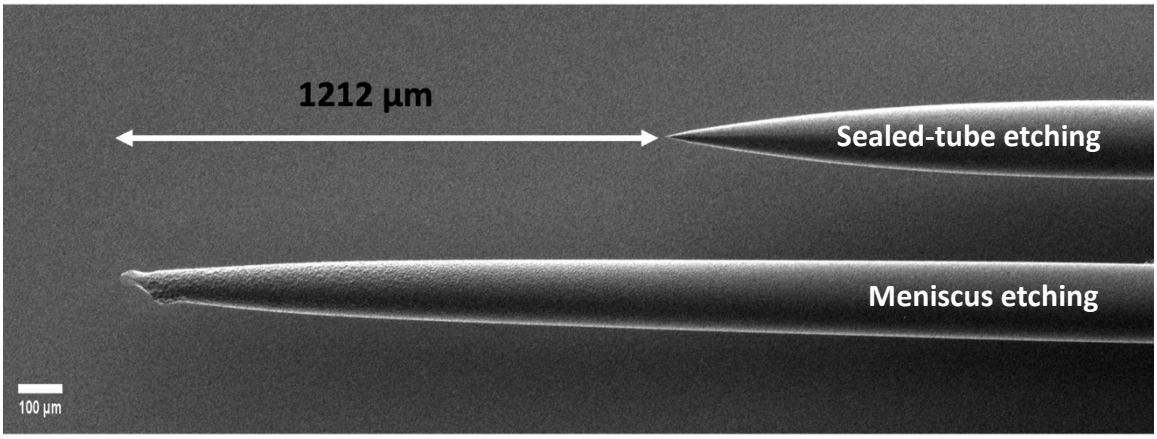

Figure 4.15: Tip formation comparison between meniscus and MST etching after 720 minutes of etching.

4.6 Concluding Remarks

The trend in the cone angle progression with etching time showed that the etching process in the MST etching method is not “self-limiting”, but rather that the shape of the conical probe changes with increasing etching time. And this change is not unidirectional but oscillating, which casts doubts on the etching mechanisms based on “micro-convection” or “a second kind of convection” as suggested by the research of other tube etching processes. The results from the experiments comparing meniscus etching and MST etching show a shortening of the tips beyond the HF layer, which is shown schematically in Figure 4.16.

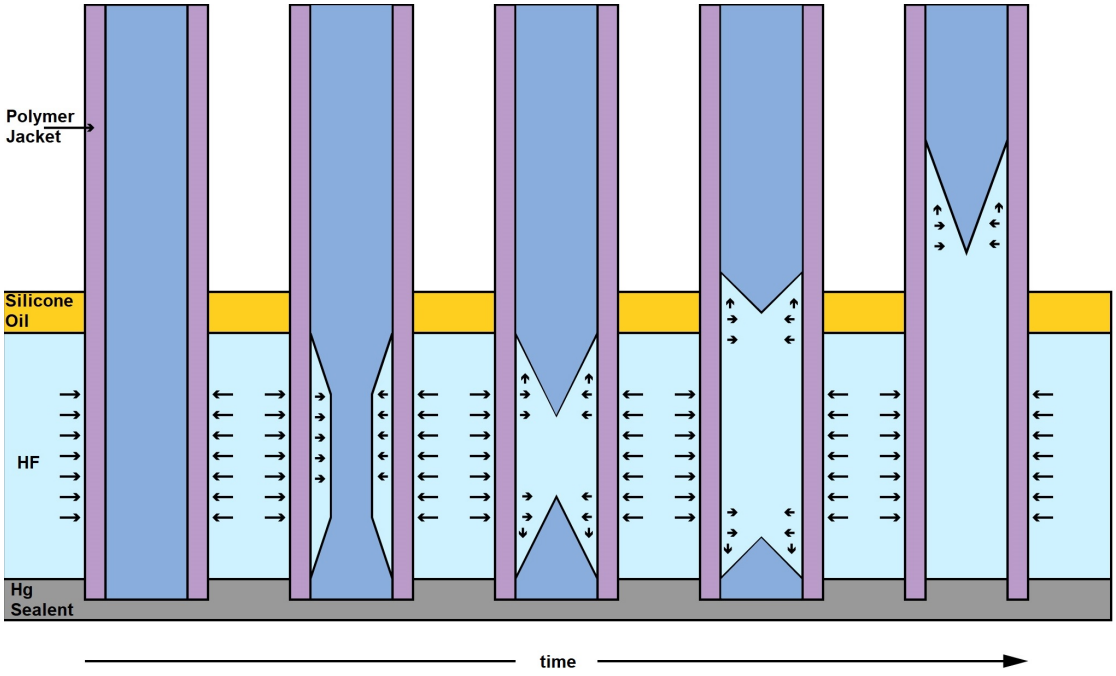

Figure 4.16: Schematic representation of the etching process for the MST etching method.

The possible etching mechanism as well as potential factors affecting the mechanism is discussed in the next chapter. The results showed that the maximum cone angle achieved by the MST etching method was approximately $24°$.

References

(1) Veerman, J. A.; Otter, A. M.; Kuipers, L.; van Hulst, N. F. High Definition Aperture Probes for Near-Field Optical Microscopy Fabricated by Focused Ion Beam Milling. *Appl. Phys. Lett.* **1998**, *72* (24), 3115–3117. https://doi.org/10.1063/1.121564.

(2) Hecht, B.; Sick, B.; Wild, U. P.; Deckert, V.; Zenobi, R.; Martin, O. J. F.; Pohl, D. W. Scanning Near-Field Optical Microscopy with Aperture Probes: Fundamentals and Applications. *J. Chem. Phys.* **2000**, *112* (18), 7761–7774. https://doi.org/10/bttvp3.

(3) Bethe, H. A. Theory of Diffraction by Small Holes. *Phys. Rev.* **1944**, *66* (7–8), 163–182. https://doi.org/10.1103/PhysRev.66.163.

(4) Kim, J.; Song, K.-B. Recent Progress of Nano-Technology with NSOM. *Micron* **2007**, *38* (4), 409–426. https://doi.org/10/bqxvpq.

(5) Novotny, L.; Hafner, C. Light Propagation in a Cylindrical Waveguide with a Complex, Metallic, Dielectric Function. *Phys. Rev. E* **1994**, *50* (5), 4094–4106. https://doi.org/10.1103/PhysRevE.50.4094.

(6) Dunn, R. C. Near-Field Scanning Optical Microscopy. *Chem. Rev.* **1999**, *99* (10), 2891–2928. https://doi.org/10/dcr69v.

(7) Stähelin, M.; Bopp, M. A.; Tarrach, G.; Meixner, A. J.; Zschokke-Gränacher, I. Temperature Profile of Fiber Tips Used in Scanning Near-field Optical Microscopy. *Appl. Phys. Lett.* **1996**, *68* (19), 2603–2605. https://doi.org/10.1063/1.116195.

(8) Liu, Y. X.; Zhang, B.; Zhang, N.; Liu, Z. L. Fabricating Fiber Probes for Optical Tweezers by an Improved Tube Etching Method. *Appl. Opt.* **2019**, *58* (29), 7950. https://doi.org/10/gmzqf6.

(9) Nikbakht, H.; Latifi, H.; Oraie, M.; Amini, T. Fabrication of Tapered Tip Fibers With a Controllable Cone Angle Using Dynamical Etching. *J. Light. Technol.* **2015**, *33* (23), 4707–4711. https://doi.org/10/gmzqf4.

(10) Stöckle, R.; Fokas, C.; Deckert, V.; Zenobi, R.; Sick, B.; Hecht, B.; Wild, U. P. High-Quality near-Field Optical Probes by Tube Etching. *Appl. Phys. Lett.* **1999**, *75* (2), 160–162. https://doi.org/10/d7m8jt.

(11) Shi, J.; Qin, X. R. Formation of Glass Fiber Tips for Scanning Near-Field Optical Microscopy by Sealed- and Open-Tube Etching. *Rev. Sci. Instrum.* **2005**, *76* (1), 013702. https://doi.org/10.1063/1.1823778.

(12) Lambelet, P.; Sayah, A.; Pfeffer, M.; Philipona, C.; Marquis-Weible, F. Chemically Etched Fiber Tips for Near-Field Optical Microscopy: A Process for Smoother Tips. *Appl. Opt.* **1998**, *37* (31), 7289. https://doi.org/10/cnzw5x.

(13) Carlson, C. A. Development of the Electrostatic Corral for the Trapping of Single Molecules in Solution. Ph.D. Dissertation, University of Wisconsin-Milwaukee, Milwaukee, WI, 2010.

CHAPTER 5

Optical Fiber Etching Simulation

5.1 Overview

The focal point of this chapter is to attain the second objective i.e., “To develop a multiphysics simulation model for the chemical fabrication process of the NSOM probe” stated in the introductory chapter. Multiphysics simulation and COMSOL Multiphysics® software are explained briefly at the beginning of this chapter. After that the models for the etching simulation are discussed in greater detail. This covers setting up the models in COMSOL® by specifying the governing equations, the boundary conditions, and the geometry as well as the results of the etching simulation that includes comparison of the models. Next, the discussion of the wicking simulation models includes model setup and their results. The chapter ends with some concluding remarks about the simulation results.

5.2 Multiphysics Simulation

If a system consists more than one type of physical phenomenon and each phenomenon is governed by its own principle(s) for evolution or equilibrium, typically expressed by a conservation law, then it is called a multiphysics system.[1] When a simulation model couples multiple physical systems, and each of these systems captures a different type of physics, then it is commonly referred to as a multiphysics simulation or multiphysics modelling.[1,2] In “Lectures on Physics”, Richard Feynman said, “*There is only one precise way of presenting laws, and that is by means of differential equations*”.[3]

Partial differential equations (PDEs) describe the change of a system in more than one independent variable over space and time rather than its state; hence the laws of physics for space- and time-dependent problems of a system are usually expressed in terms of PDEs in multiphysics simulations.[1,4,5] Analytical methods cannot solve the PDEs that describe the vast majority of geometries and problems. Therefore, numerical model equations are constructed from the PDEs by different types of discretization methods that approximate the PDEs and then solve them using numerical methods.[5] Among the various numerical methods, the three most popular methods to solve PDEs are: (a) the finite difference method (**FDM**), (b) the finite element method (**FEM**), and (c) the finite volume method (**FVM**).[6]

5.2.1 COMSOL Multiphysics®

COMSOL Multiphysics® is a commercially available interactive computer simulation environment used for modelling and solving scientific and engineering problems. The built-in "*physics interfaces*" and the support for material properties in the COMSOL Multiphysics® software simplifies model building by defining the relevant physical quantities rather than by defining the underlying equations. That said, the option of applying variables, expressions, or numbers directly to solid and fluid domains, boundaries, edges, and points independently of the computational mesh is always available in the software.

COMSOL® finds solutions to simulations models using the finite element method (FEM) applied to the weak forms (the integral forms) of the numerical equations. Although

COMSOL® in its base configuration (Figure 5.1(a)) has the capabilities of creating simulation models for many application areas, there are also optional add-on modules (Figure 5.1(b)) for several of the key application areas. These application-specific modules use terminology, solution methods, and plot types specific to corresponding disciplines, which simplifies creating and analyzing models.

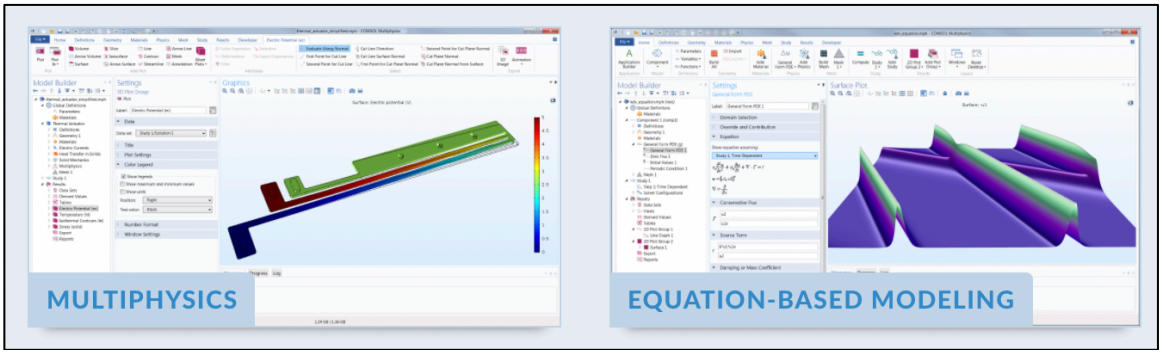

(a)

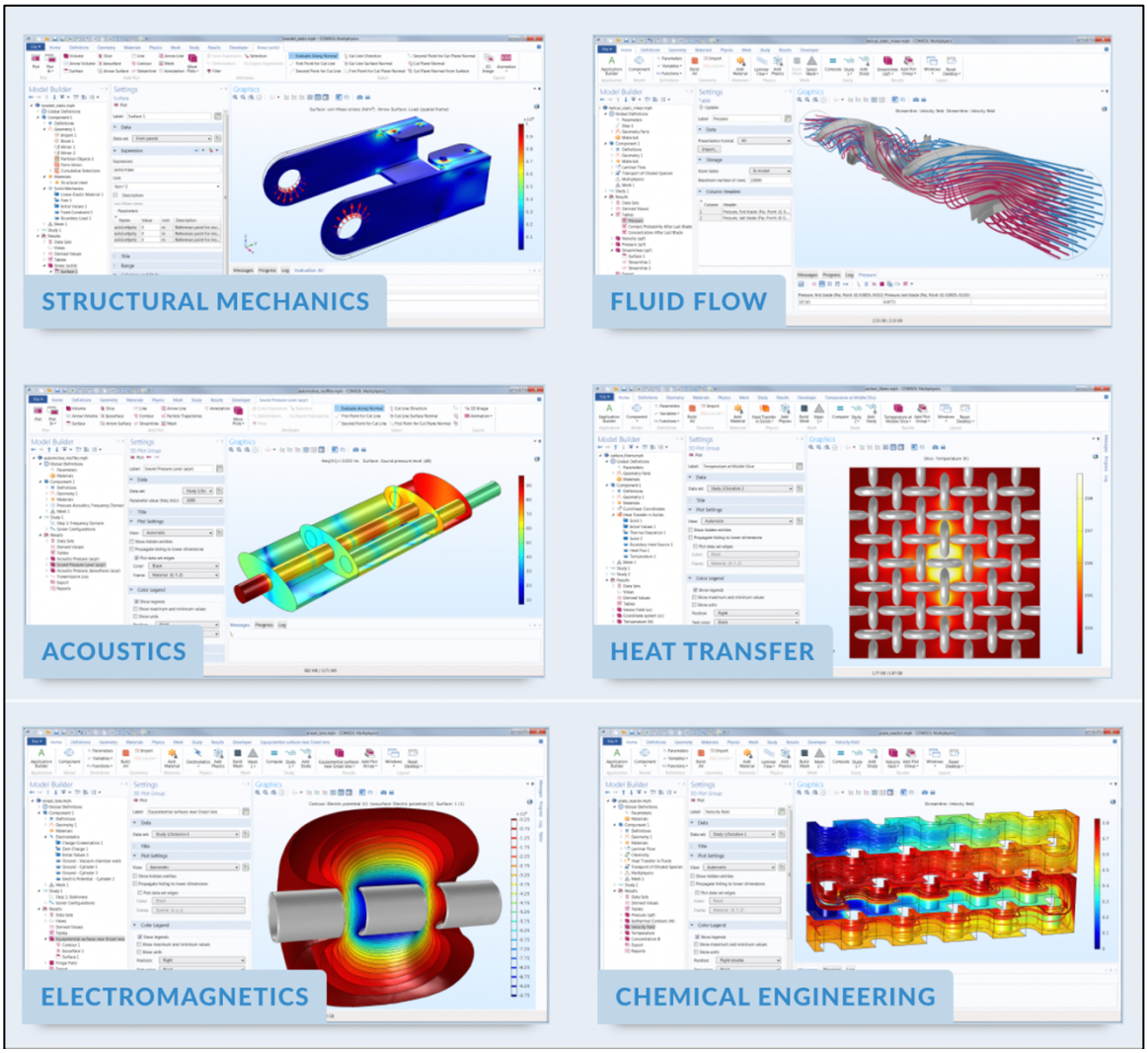

(b)

Figure 5.1: Views of simulations in COMSOL Multiphysics® software with (a) the base configuration, and (b) optional add-on modules. Image made using COMSOL Multiphysics® software and provided courtesy of COMSOL.

The *COMSOL Desktop*® user interface (Figure 5.2) in COMSOL® provides a modeling environment for creating, analyzing, and visualizing multiphysics models and applications. We used COMSOL Multiphysics® v. 5.5 software with the "*Microfluidics*" and "*Particle Tracing*" optional add-on modules to develop simulation models for the different projects in our research group.

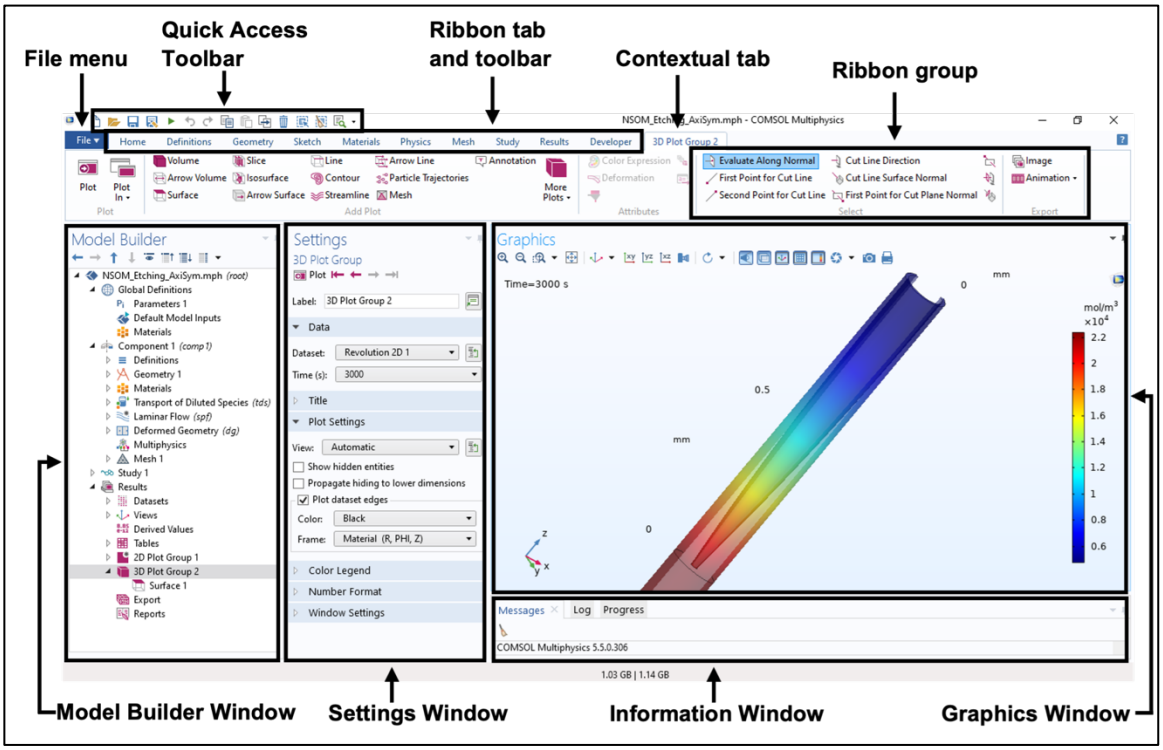

Figure 5.2: Different functionalities in the Graphical User Interface (GUI) of the *COMSOL Desktop*®.

5.3 Setting up of Etching Model

Not many published articles can be found with simulation models of the wet etching process of crystalline SiO_2 structures by HF, and none of them describe a simulation model for etching of an optical fiber by HF. Most of the SiO_2 etching simulation models feature HF fluid flow over a horizontal, rectangular SiO_2 structure with an HF-resistant mask on top, whereas an optical fiber etching simulation model requires having a vertical, cylindrical SiO_2 structure surrounded by a still HF fluid, with no HF-resistant mask

between SiO_2 and HF. However, all published SiO_2 etching simulation models use the same generally accepted overall chemical equation (Equation 5.1) for the surface etching of SiO_2 by HF, despite the wide range of opinions about the etching mechanism.

$$SiO_2 + 6HF \rightleftharpoons H_2SiF_6 + 2H_2O \qquad (5.1)$$

Additionally, most researchers agree that the etching mechanism follows a non-first order kinetics, but every published SiO_2 etching model assumes that the etching reaction follows first-order kinetics. Making such an assumption simplifies the model without losing too much accuracy. In the time-dependent study of our simulation model for MST etching of a single-mode optical fiber, we also used first-order kinetics for the etching reaction (Equation 5.2).

$$\frac{-d[SiO_2]}{dt} = k[HF] \qquad (5.2)$$

5.3.1 Physics Interfaces and Governing Equations

The key physical processes involved in the wet chemical etching of an optical fiber by HF are:

- Mass transport of HF toward the SiO_2 surface
- Fluid flow
- Surface reactions
- Change in geometry due to the surface reactions

In COMSOL Multiphysics®, the mass transport and the surface reaction can be simulated using the "*Transport of Diluted Species (TDS)*" interface. With this interface, a surface reaction is described as a flux of HF into the optical fiber surface where the HF is consumed in the etching reaction. Therefore, the HF species needs to be transported from the bulk concentration boundary to the reacting surface boundary through a domain of solvent assumed to be liquid water.

The *TDS* interface can simulate the diffusive transport of HF, but coupling this interface with the "*Laminar Flow (LF)*" interface can add convective transport to the simulation.[7] The simulation of the mass transport of HF is thus achieved by solving the convection-diffusion equations (Equations 5.3-5.4):

$$\frac{\partial c}{\partial t} + \nabla \cdot \mathbf{J} + \mathbf{u} \cdot \nabla c = \mathbf{R} \qquad (5.3)$$

$$\mathbf{J} = -D\nabla c \qquad (5.4)$$

where $\mathbf{J}$ is the flux, c is the HF concentration, $\mathbf{R}$ represents the "sources" or the "sinks" for c, D is the diffusion coefficient, and $\mathbf{u}$ is the fluid velocity. At the etching surface (i.e., the moving boundary) the flux condition is considered as in Equation 5.5:

$$D\nabla c \cdot \mathbf{n} = -\kappa c \qquad (5.5)$$

where κ (SI unit: $\mathrm{m/s}$) is the etching rate constant for linear kinetics of the etching species and $\mathbf{n}$ is the normal vector.

The fluid velocity $\mathbf{u}$ is obtained by solving the Navier-Stokes equation (Equation 5.6) for laminar flow of a compressible Newtonian fluid together with the continuity equation (Equation 5.7):

$$\rho\frac{\partial \mathbf{u}}{\partial t} + \rho(\mathbf{u}\cdot\nabla)\mathbf{u} = \nabla\cdot[-p\mathbf{I} + \mu(\nabla\mathbf{u} + (\nabla\mathbf{u})^T)] + \mathbf{F} \qquad (5.6)$$

$$\rho\nabla\cdot\mathbf{u} = 0 \qquad (5.7)$$

where ρ is the fluid density, p is the fluid pressure, μ is the fluid dynamic viscosity, and $\mathbf{F}$ is the external forces applied to the fluid.

The reaction rate at the optical fiber surface is coupled with a "*Deformed Geometry (DG)*" interface so that the reaction causes a change in the geometry. The coupling is done by converting the reaction rate to a normal mesh velocity using the following three equations (Equations 5.8-5.10):

$$v_{\mathrm{n}} = R_s \mathrm{K_D} \qquad (5.8)$$

$$R_{\mathrm{s}} = \hbar c \qquad (5.9)$$

$$\mathrm{K_D} = \frac{\mathrm{M_{SiO_2}}}{\mathrm{n_F}\rho_{\mathrm{SiO_2}}} \qquad (5.10)$$

where v_{n} is the normal mesh velocity, R_{s} is the etching rate at the optical fiber interface, $\hbar$ is the etching rate constant, $\mathrm{K_D}$ is a coefficient of proportionality called diffusion model constant, and $\mathrm{n_F}$ is the number of HF molecules consumed per $\mathrm{SiO_2}$ unit.[8]

5.3.2 Geometry and Simulation Conditions

In the MST etching experiment of the single-mode optical fibers, the fibers were partially submerged in the HF beaker containing Hg, so a $2\mathrm{D}$ geometry was created that represented the longitudinal cross-section of the optical fiber dipped in HF and $\mathrm{H}g$. However, because the length of the optical fiber and the diameter of the HF beaker were several times larger than the diameter of the optical fiber with the polymer jacket, the optical fiber would have appeared like the longitudinal cross-section of a thin wire if the geometry was created with the actual dimensions of the experimental etching setup. Therefore, all the dimensions of the experimental etching setup other than the diameter of the optical fiber were scaled down while creating the geometry in COMSOL®, representing a longitudinal cross-section of the system such that it would not influence the simulation results (Figure 5.3).

In Figure 5.3, the rectangular domain structures are shaded blue for the HF solution, grey for the Hg-sealant, and purple for the polymer jacket. However, the $125\ \mu\mathrm{m}$ wide optical fiber (the core and the cladding are depicted here as a single unit) is not represented by a rectangular domain structure in the Figure 5.3, but was constructed by blocking the two sides of an open space with $62.5\ \mu\mathrm{m}$ wide, purple rectangular domain structures representing the polymer jacket around the fiber. The reason behind it was that the *DG* interface does not allow any deformation of the border boundary between domain structures. Only the boundary conditions for the *TDS* interface are shown in Figure 5.3 – dashed lines for “Flux” boundaries, solid lines for “No Flux” boundaries, and c_{bulk} for “Concentration” boundaries.

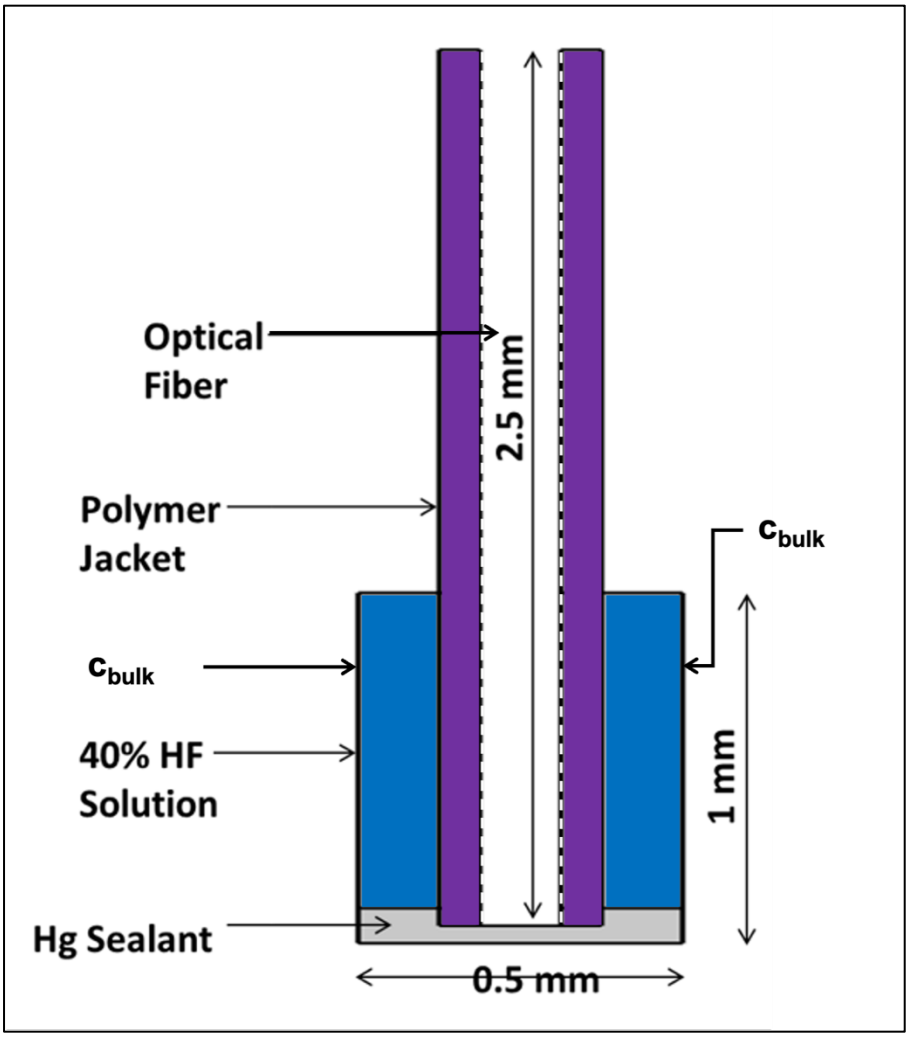

Figure 5.3: 2D geometry in COMSOL® for etching simulation representing the MST etching experimental setup where dashed lines represent "Flux" boundaries and solid lines represent "No Flux" boundaries in the TDS interface.

A constant bulk concentration of HF was assumed at the "Concentration" boundaries. The "Concentration" boundaries and the "Flux" boundaries were connected through a liquid water solvent domain (blue shades in Figure 5.4). There is a diffusive flux of HF from the bulk to the etched surface due to the concentration gradient, which replenishes the HF at the surface so that the etching process can continue. The domains

representing the polymer jacket were selected as liquid water solvent domain because COMSOL® cannot calculate the diffusion of HF from the “Concentration” boundaries to the “Flux” boundaries in the TDS interface if these boundaries are not connected by a fluid.

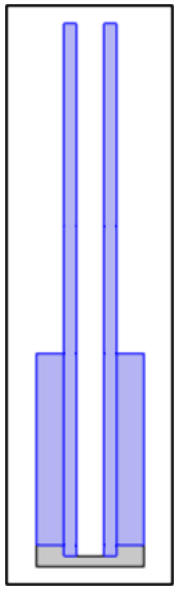

Figure 5.4: Domains (blue shades) in the geometry selected as solvent domain in *TDS* interface with the etching simulation models.

The boundaries selected as “Flux” for the *TDS* interface in Figure 5.3 were also the boundaries selected using the “Prescribed Normal Mesh Velocity” making these boundaries move and deform according to the velocity given by Equation 5.8. COMSOL® calculates the flux and the normal mesh velocity using the parameters from Table 5.1. A time-dependent study of the models was performed from $t = 0\ \mathrm{s}$ to $t = 28800\ \mathrm{s}\ (8\ \mathrm{h})$ in steps of $\Delta t = 300\ \mathrm{s}$.

Table 5.1: Values (in SI units) used for the parameters in the etching simulation models.

Parameters	Values
40% HF bulk concentration (c_{bulk})	$22.4{\cdot}10^{3}\ \mathrm{mol/m^3}$
Diffusion coefficient for HF (D)	$3.0{\cdot}10^{-9}\ \mathrm{m^2/s}$
Estimated etching rate constant (k)	$4.0{\cdot}10^{-7}\ \mathrm{m/s}$
Diffusion model constant (K_D)	$2.01{\cdot}10^{-6}\ \mathrm{m^3/mol}$

5.3.3 Three Variant Models

We developed three simulation models with the acknowledgement of the fact that the simulation of HF diffusion through the polymer jacket might not accurately represent the experimental process because of two possible drawbacks in the models. The first drawback was that the polymer jacket domains needed to be part of the liquid water solvent domain in the simulation models for the *TDS* interface to function properly, which meant that HF could diffuse to any part of the polymer jacket domain including the top ends. The second drawback was that the diffusion coefficient for HF in the polymer jacket should have a lower value than that in water, but this value is unknown.

In the first model (*Model 1*), we tried to resolve the second drawback by assigning an arbitrary, lower value to the isotropic diffusion coefficient for HF in the polymer jacket domain to mimic the actual etch rate. However, this model lacked the wicking phenomenon that any porous media, such as the polymer jacket, will show when partially

submerged in liquid, which is due to the first drawback. In the second model (*Model 2*), we tried to solve the issue and mimic the wicking process using anisotropic HF diffusion in the polymer jacket domain by assigning an even lower value to the diffusion coefficient for HF in the vertical direction.

In the third model (*Model 3*), we propose that the MST etching of optical fiber follows a mechanism akin to the Shrinking Core Model (SCM). During the MST etching experiment, the optical fiber was being etched radially inside the polymer jacket creating a tube filled with etchant and products. We assume that the diffusion of the products is much slower than that of the etchant. This means that over time product accumulates inside the tube and HF has to diffuse through the product layer to reach the etching surface. Eventually, the etch rate at the cone tip becomes slower than that of the cone base region, resulting in the observed trend of a decreasing cone angle with the progression of time. But when most of the product has diffused out of the tube, then the etch rate in the cone tip region becomes faster than that of the cone base region, which again leads to an increase in cone angle. We incorporated this mechanism into the lateral part of the anisotropic diffusion field of the *TDS* interface using a function in *Model 3*.

Additionally, we found from simulations that the maximum height of the liquid front in polymer jacket of an unetched optical fiber is about $1\ \mathrm{mm}$ above the liquid layer whenever wicking occurs. However, in the MST experiments, we found that etching effects can be observed more than $2\ \mathrm{mm}$ above the HF layer. We think that the wicking in polymer jacket could be dynamic (i.e., that the maximum height of the liquid front changes with time) because the height of the HF layer inside the tube increases over

time. So, we restricted any vertical HF diffusion inside the polymer jacket domain to $1\ \mathrm{mm}$ above the HF layer for the first half of the simulation and used a function in the vertical part of anisotropic diffusion field of the *TDS* interface in *Model 3* for the second half of the simulation to simulate the change in the maximum height of the liquid front with time.

5.4 Wet Etching Simulation Results

The simulation results from all three models showed that the initial tip was formed after 160 minutes, which agrees with the experimental etch rate. The cone angle of the initially formed tip was different for the different models. But all models showed tip formation near the top boundary of the HF solution domain that represents the oil-HF interface.

5.4.1 Model 1

The results of the time-dependent simulation of *Model 1* are shown in Figure 5.5 for t values of: $0\ \mathrm{min}$, $60\ \mathrm{min}$, $120\ \mathrm{min}$, $160\ \mathrm{min}$, $210\ \mathrm{min}$, and $240\ \mathrm{min}$. These results demonstrate the formation of the tip and that the cone angle changes with time. It shows that a tip is formed due to the concentration gradient at the corner of the two “No Flux” boundaries between the solution domain and polymer jacket domain. In this model, the concentration gradient of HF is most pronounced at what becomes the base of the cone. This results in an initial tip formation with a moderately wide cone angle. The increase in cone angle over time shown can also be considered moderate.

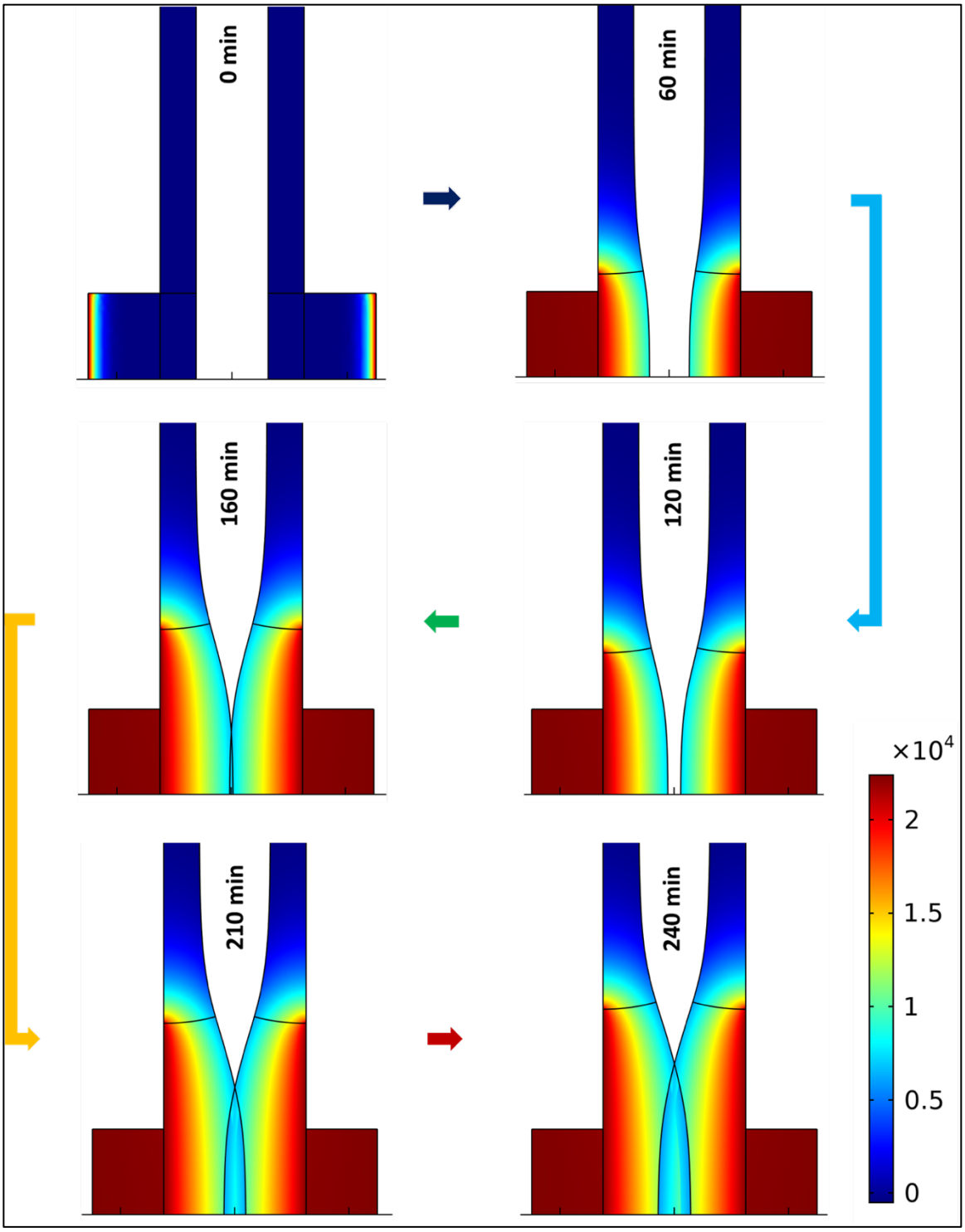

Figure 5.5: Simulated results showing tip formation and progression of cone angles over time in the etching simulation *Model 1* for t values from $0\,\mathrm{min}$ to $240\,\mathrm{min}$. Here, the color legend represents HF concentration in $\mathrm{mol/m^3}$.

5.4.2 Model 2

Figure 5.6 displays the simulation results of *Model 2* for the same t values as the *Model 1* simulation. The cone angle of the initially formed tip is much wider than the first model. The HF concentration change is most pronounced near the cone base, and because of the reduced vertical diffusion, the cone base is closer to where the tip will be formed. It was also found that the increase in cone angle over time was much greater in *Model 2* than in *Model 1*.

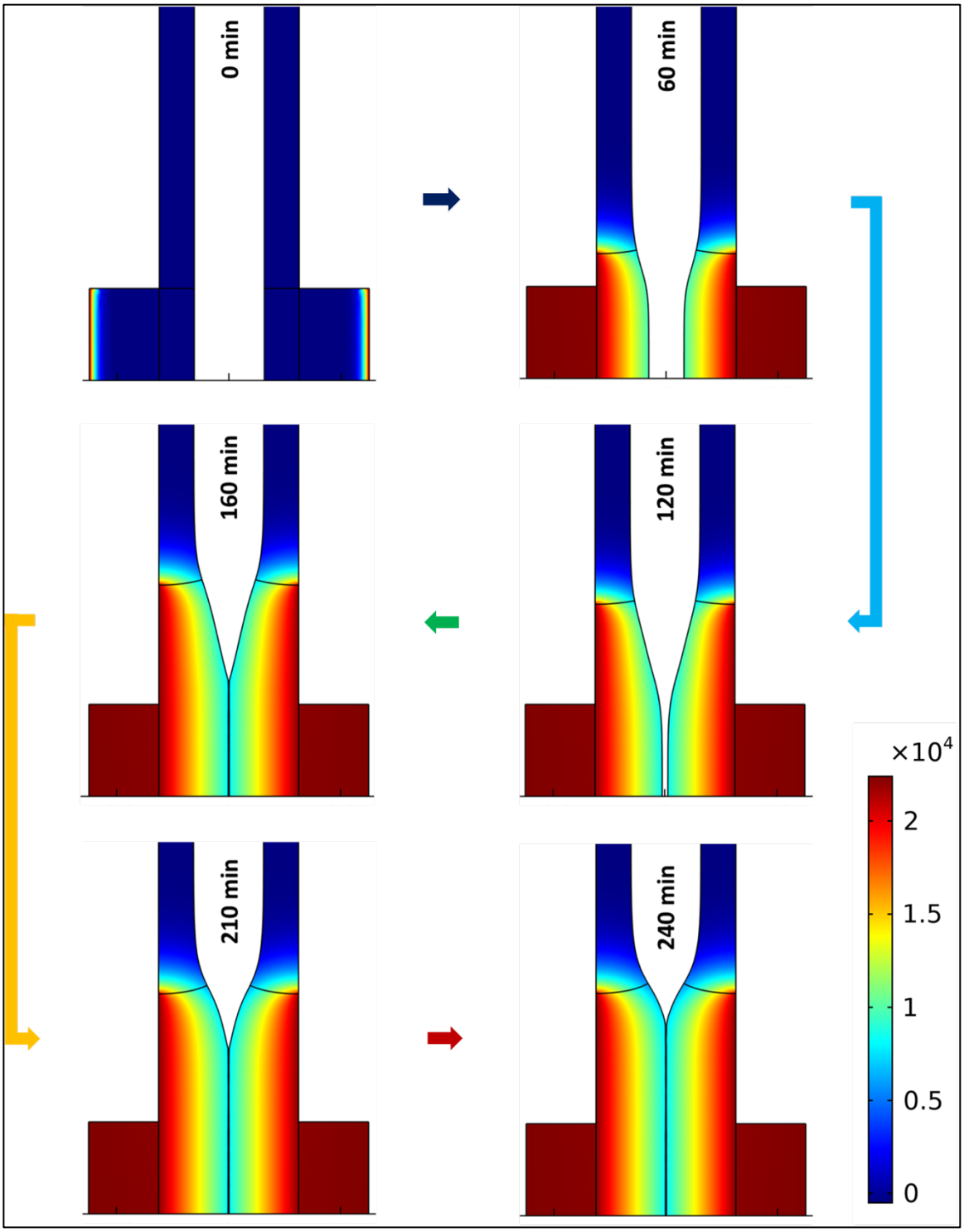

Figure 5.6: Simulated results showing tip formation and progression of cone angles over time in the etching simulation *Model 2* for t values from $0\,\mathrm{min}$ to $240\,\mathrm{min}$. Here, the color legend represents HF concentration in $\mathrm{mol/m^3}$.

5.4.3 Model 3

The simulation results of *Model 3* are presented in Figure 5.7 (using the same t values as for the other two models) and show that the initially formed tip has the narrowest cone angle among all the models. In this case, the concentration gradient of HF is not confined to a small area near the cone base but rather spread over a much larger area. This effect of the concentration gradient is caused by the fluctuation of HF diffusion in the lateral direction by the implementation of the SCM model into the simulation. This model shows the increase in cone angle over time, and the tip moves higher much more quickly over time compared to the other two models.

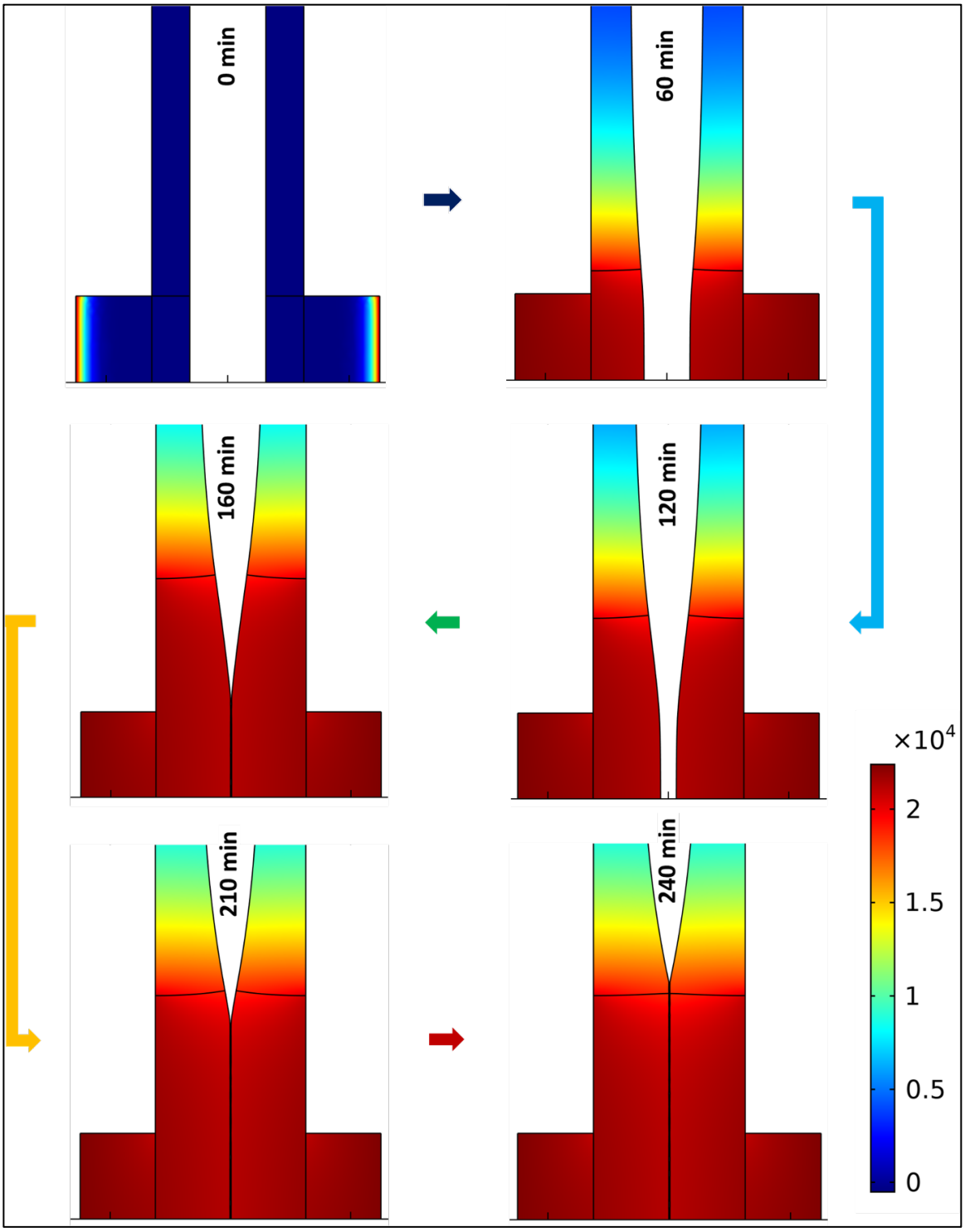

Figure 5.7: Simulated results showing tip formation and progression of cone angles over time in the etching simulation *Model 3* for t values from $0\,\mathrm{min}$ to $240\,\mathrm{min}$. Here, the color legend represents HF concentration in $\mathrm{mol/m^3}$.

5.4.4 Comparison of the Three Models

We want to compare the results of the three simulation models among themselves as well as with the experimental results. Experimentally, the tips were formed after $160\ \text{min}$ and had the largest cone angle after $240\ \text{min}$ of etching time. First, we put the results of the three simulation models side-by-side for t values of $160\ \text{min}$ (Figure 5.8(a)) and $240\ \text{min}$ (Figure 5.8(b)) and compare them visually. It is evident from Figure 5.8 that *Model 3* has the smallest and *Model 2* has the largest cone angles for both t values of $160\ \text{min}$ and $240\ \text{min}$.

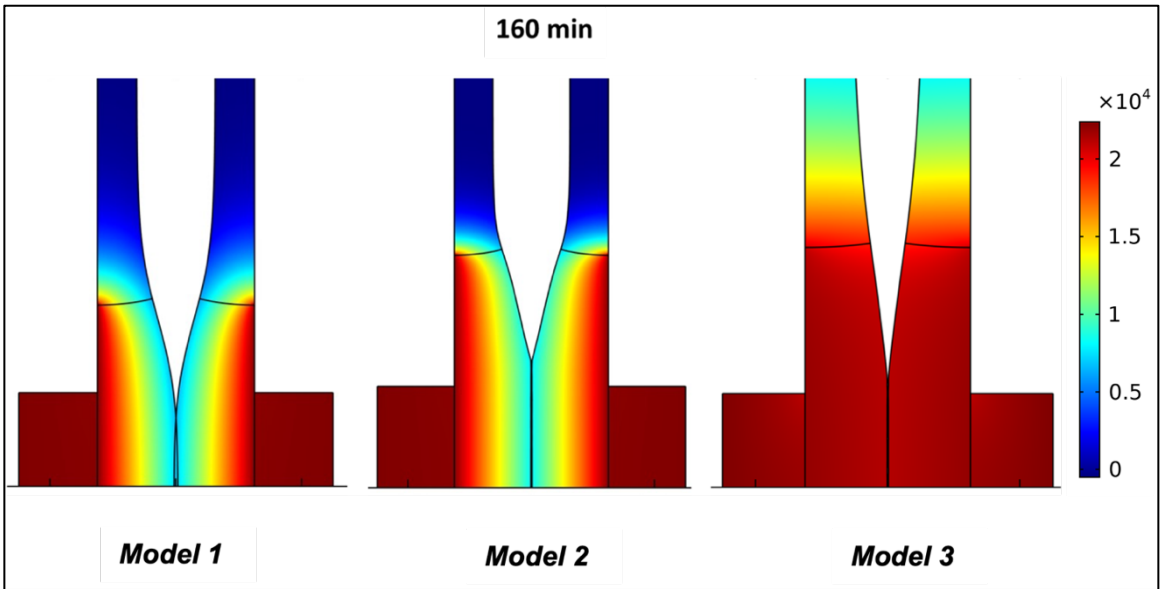

(a)

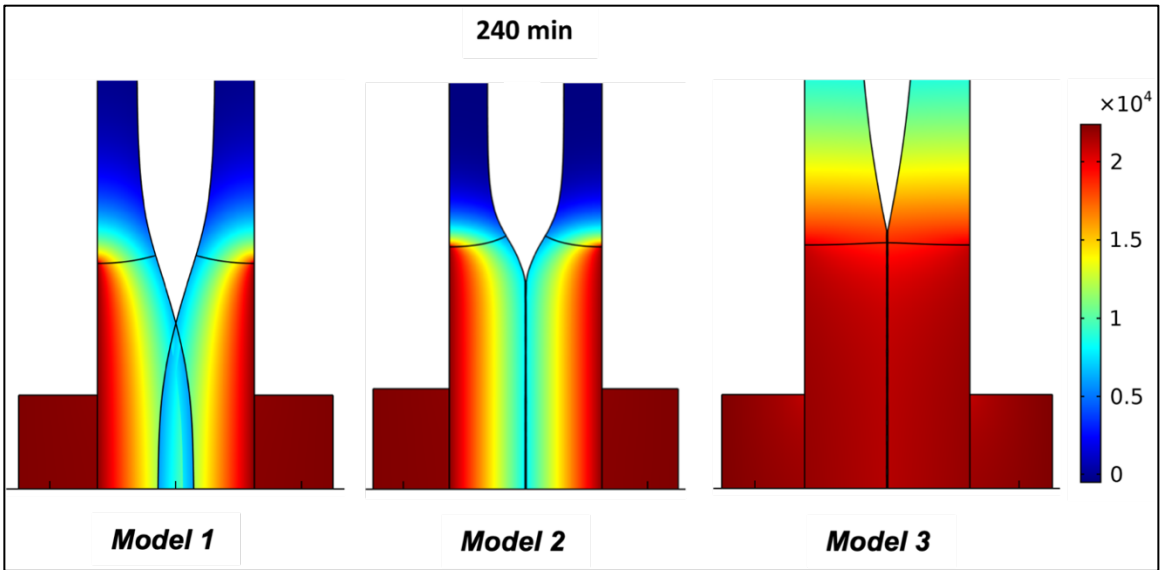

(b)

Figure 5.8: Visual comparison of the cone angles formed in the time-dependent simulation with t values of (a) $160\ \mathrm{min}$, and (b) $240\ \mathrm{min}$ for the three etching models. Here, the color legend represents HF concentration in $\mathrm{mol/m^3}$.

Next, we did a trend analysis of the progression of cone angles with time for the three simulation models and compared these trends with the experiments. To do this, we measured all the cone angles from the results of the three simulation models with t values between 3 hours and 6 hours at ½ hour increments as well as with t value of $160\ \mathrm{min}$ using ImageJ as shown in Table 5.2.

Table 5.2: Measured cone angles of the three etching simulation models with t values varied in ½ hour increments.

t (min)	Cone Angle (°)		
	Model 1	***Model 2***	***Model 3***
160	18.3	34.9	13.6
180	25.1	41.4	15.9
210	30.6	49.2	19.6
240	32.5	54.4	23.2
270	35.5	59.2	22.0
300	37.6	63.0	21.0
330	39.0	64.9	21.1
360	40.5	67.2	19.9

Figure 5.9 presents the cone angle data for the simulation models from Table 5.2 and the cone angle data for the MST etching experiments from Table 4.1 in Chapter 4. Similar to the side-by-side comparison, the data shows that *Model 3* generated the smallest and *Model 2* generated the largest cone angles over time.

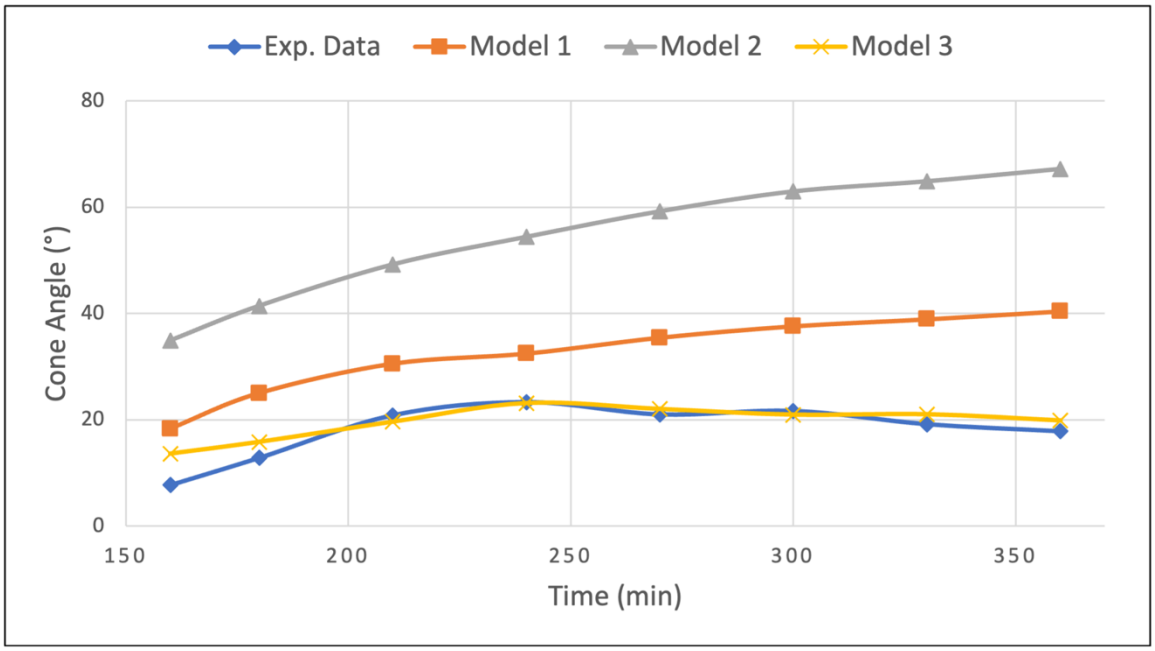

Figure 5.9: Comparison plot of the progression in cone angles with time of the three etching simulation models with the MST etching experiment.

The figure also shows that only the *Model 3* showed similar trends in the progression of cone angles with time as the experimental results. In the other two models, cone angles gradually increased with time and were much wider than the experimental values. Therefore, we compared only the cone angles from *Model 3* with the experimental cone angles in a new plot (Figure 5.10). In this plot, both *Model 3* and experimental values show an increase in cone angles and reach the same, highest point after $240\ \mathrm{min}$, although the cone angles of the initially formed tips were different. In addition, it was interesting to see that *Model 3* shows a decreasing trend for the cone angles at times greater than $240\ \mathrm{min}$ similar to the etching experiments, which was not seen in the other two models.

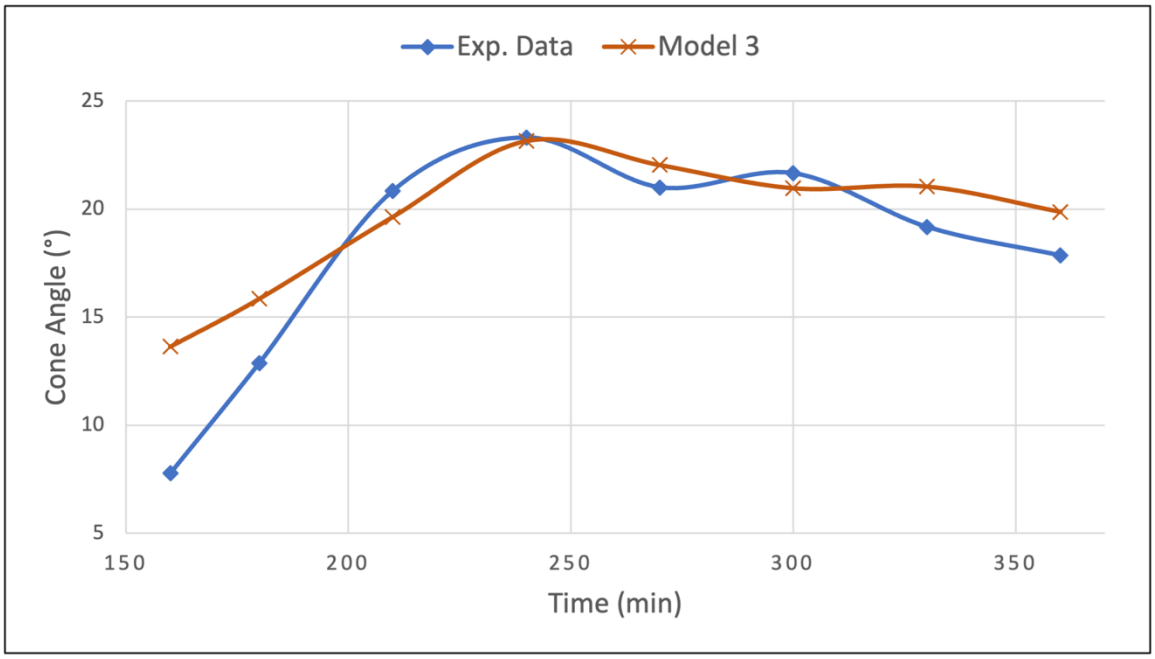

Figure 5.10: Comparison plot of the progression in cone angles with time of the etching simulation *Model 3* with the MST etching experiment.

5.5 Wicking Simulation

The SCM model for the etching reaction and the dynamic wicking in the polymer jacket were at the center of *Model 3*. In porous media wicking, the liquid front reaches a certain, maximum height that doesn't change over time if the interface between the porous media and the reservoir is not moved. However, the maximum height of the liquid front will evolve if the interface between the porous media and the reservoir is moved in the direction of wicking. In case of fiber etching, the height of the HF layer rises inside the tube over time and might become the interface of a new liquid source for wicking. We carried out time-dependent simulations with simplified $2\mathrm{D}$ models for wicking in the polymer jacket of an optical fiber to test the hypothesis above. The models were created

with a rectangular geometry having a length of $12\,\mathrm{cm}$ and a width of $150\,\mu\mathrm{m}$ that represented only the polymer jacket of an optical fiber. The different material parameters used in the wicking models are listed in Table 5.3.

Table 5.3: Material properties for air, water, and the polymer jacket of an optical fiber for the wicking simulation models.

Parameters	Values
Thickness of polymer jacket	$1.0{\cdot}10^{-4}\ \mathrm{m}$
Density of water	$1000\ \mathrm{kg/m^3}$
Density of air	$1\ \mathrm{kg/m^3}$
Porosity	0.1
Pore radius	$8.8{\cdot}10^{-7}\ \mathrm{m}$
Pore size distribution index	2
Permeability	$6.195{\cdot}10^{-12}\ \mathrm{m^2}$
Viscosity of water	$1.0{\cdot}10^{-3}\ \mathrm{Pa{\cdot}s}$
Viscosity of air	$1.76{\cdot}10^{-5}\ \mathrm{Pa{\cdot}s}$
Surface tension of water	$7.23{\cdot}10^{-2}\ \mathrm{m}$
Contact angle	0

Setting-up the wicking models required coupling of the "*Darcy's Law (DL)"* and "*Phase Transport in the Porous Media (PTPM)*" interfaces of the "*Porous Media Flow*" module which was provided courtesy of COMSOL® by means of a trial license. COMSOL® finds the volume fraction s_i of the wetting or nonwetting fluid i by solving Equation 5.11 for the *PTPM* interface:

$$\frac{\partial}{\partial t}(\varepsilon_p \rho_i s_i) + \nabla \cdot (\rho_i \kappa \frac{\kappa_{ri}}{\mu_i}(\nabla p_i - \rho_i g)) = \boldsymbol{Q}_i = 0 \qquad (5.11)$$

where ε_p is the porosity, ρ_i is the fluid density, κ_{ri} is the relative permeability, μ_i is the fluid's dynamic viscosity, and p_i is the pressure. The governing equation (Equation 5.12) for the *DL* interface combines Darcy's law with the continuity equation:

$$\frac{\partial}{\partial t}(\rho \varepsilon_p) + \nabla \cdot \rho[-\frac{\kappa}{\mu}(\nabla p)] = 0 \qquad (5.12)$$

where density ρ and dynamic viscosity μ are average values of the two wetting and nonwetting fluids. The rectangle is initially filled with air with an initial water saturation of 0.01. There is no water flow at the side boundaries. For the water phase, atmospheric pressure is set at the bottom boundary and capillary pressure subtracted from the hydrostatic atmospheric pressure is set at the top boundary. For the air phase, no flux is assumed at the bottom boundary and a mass flux is defined at the top boundary.

5.5.1 Fixed Reservoir

In the first wicking model, the bottom boundary does not move so that the model represents regular wicking behavior in a polymer jacket without any effect from the etching process (Figure 5.11). The results show that the height of the liquid front reaches a maximum height of approximately $0.8\ \mathrm{mm}$ after $0.073\ \mathrm{s}$.

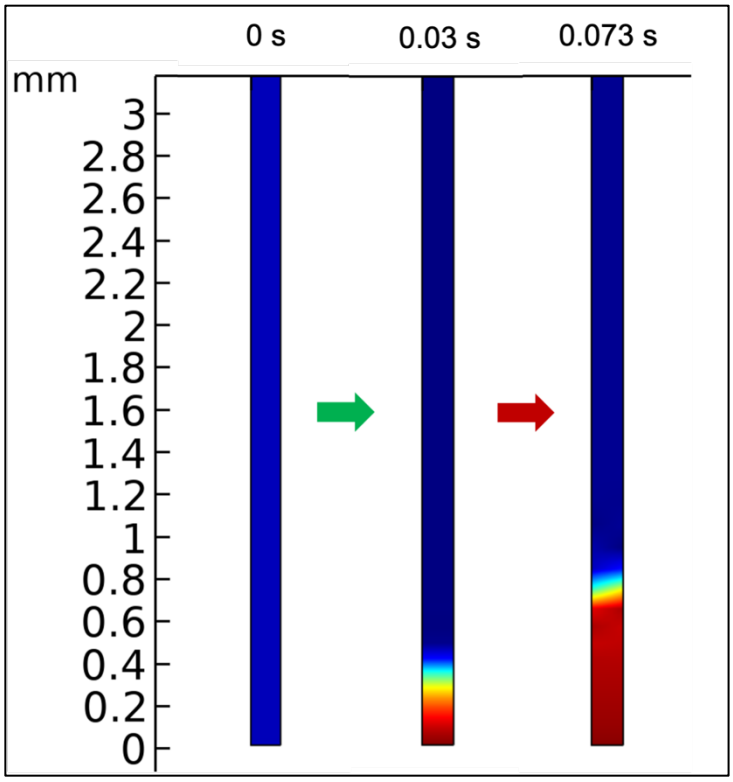

Figure 5.11: Simulated results showing wicking in polymer jacket where the liquid front reaches a maximum height in the fixed reservoir wicking simulation model.

5.5.2 Moving Reservoir

The second wicking model was developed to test the hypothesis whether the maximum height of the liquid front would rise if the HF layer inside the polymer jacket tube rises as etching progresses. To incorporate the rise in the liquid reservoir, the "*Deformed Geometry (DG)*" interface was added to the model. The bottom boundary was assigned the "Prescribed Normal Mesh Velocity" and a specific velocity at regular interval was applied to this boundary in order to mimic a rise in liquid layer at regular intervals. The results show that the maximum height of the liquid front is increasing whenever the liquid reservoir is rising (Figure 5.12).

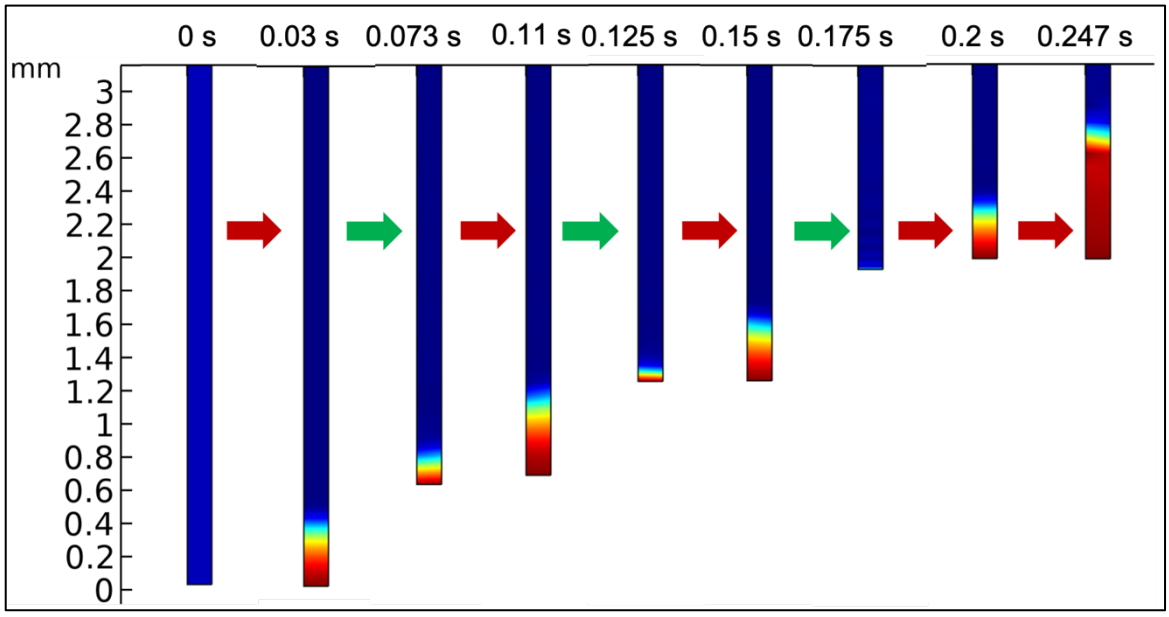

Figure 5.12: Results of moving reservoir wicking simulation model showing wicking continuing in polymer jacket where the height of the liquid front is about 3 times higher than the previous model.

5.6 Concluding Remarks

Model 3 of the etching simulation captured the trend of decreasing cone angles observed in the etching experiments of the optical fibers. This reinforces the doubts that we expressed about etching mechanisms based on “micro-convection” or “a second kind of convection”, as suggested by the research of other tube etching processes. The wicking model with moving reservoir supports the claim that during the etching process, the rise in the HF layer inside the tube causes the maximum height of the liquid front to change with time because of dynamic wicking in the polymer jacket.

References

(1) Keyes, D. E.; McInnes, L. C.; Woodward, C.; Gropp, W.; Myra, E.; Pernice, M.; Bell, J.; Brown, J.; Clo, A.; Connors, J.; Constantinescu, E.; Estep, D.; Evans, K.; Farhat, C.; Hakim, A.; Hammond, G.; Hansen, G.; Hill, J.; Isaac, T.; Jiao, X.; Jordan, K.; Kaushik, D.; Kaxiras, E.; Koniges, A.; Lee, K.; Lott, A.; Lu, Q.; Magerlein, J.; Maxwell, R.; McCourt, M.; Mehl, M.; Pawlowski, R.; Randles, A. P.; Reynolds, D.; Rivière, B.; Rüde, U.; Scheibe, T.; Shadid, J.; Sheehan, B.; Shephard, M.; Siegel, A.; Smith, B.; Tang, X.; Wilson, C.; Wohlmuth, B. Multiphysics Simulations: Challenges and Opportunities. *Int. J. High Perform. Comput. Appl.* **2013**, *27* (1), 4–83. https://doi.org/10.1177/1094342012468181.

(2) Groen, D.; Zasada, S. J.; Coveney, P. V. Survey of Multiscale and Multiphysics Applications and Communities. *Comput. Sci. Eng.* **2014**, *16* (2), 34–43. https://doi.org/10.1109/MCSE.2013.47.

(3) The Feynman Lectures on Physics Vol. II Ch. 2: Differential Calculus of Vector Fields https://www.feynmanlectures.caltech.edu/II_02.html (accessed 2022 -04 -05).

(4) Comprehensive Introduction to Physics, PDEs, and Numerical Modeling https://www.comsol.com/multiphysics/introduction-to-physics-pdes-and-numerical-modeling (accessed 2022 -04 -05).

(5) Detailed Explanation of the Finite Element Method (FEM) https://www.comsol.com/multiphysics/finite-element-method?parent=physics-pdes-numerical-042-62 (accessed 2022 -04 -05).

(6) Ruas, V. *Numerical Methods for Partial Differential Equations: An Introduction*; John Wiley & Sons, Incorporated: Chicester, UNITED KINGDOM, 2016.

(7) Karlsson, R. How to Model Wet Chemical Etching in COMSOL Multiphysics®. *COMSOL Blog*, 2017.

(8) Ivanov, A. Simulation of Electrochemical Etching of Silicon with COMSOL; Stuttgart, Germany, 2011; p 6.

CHAPTER 6

Fluorescent Nanosensor

6.1 Overview

The intent of this chapter is to demonstrate the achievement of the third objective i.e., “to develop fluorescence nanosensors based on the NSOM probe for *in situ* sensing applications” as stated in Chapter 1. This chapter starts with a description of nanosensor design where the process of creating nanosensor probes using different fluorescent molecules is discussed in detail. Next, the method for quantifying the spot intensity of images is presented. Lastly, the results of the detection experiments using the nanosensor are discussed in depth.

6.2 Nanosensor Design

A nanosensor is a sensing device that has at least one dimension on the order of $100\ \mathrm{nm}$ or less. It is used for detecting biochemicals in cellular organelles, measuring nanoscopic particles in industry and the environment, and monitoring nanoscale physical and chemical phenomena in difficult to reach regions and convert them into data for analysis.[1,2] NSOM technology has great potential for developing nanosensors to perform nanoscale detections at precise sample locations in a nondestructive manner. Like other optical sensors, nanosensors can be created by functionalizing the aperture surface of NSOM probes with a monolayer of chemically sensitive molecules that are optically responsive. In this project, the nanosensor probes were made by covalently attaching fluorescent molecules to NSOM probes.

6.2.1 Creating Nanosersor Probes

The nanosensor probes used for the sensing experiments were created by functionalizing the NSOM probe end of a $1\,\mathrm{m}$ long optical fiber (fabricated by the meniscus method) with FITC. The other end of the optical fiber was cleaved to couple laser light of wavelength $488\,\mathrm{nm}$ into the fiber because the $488\,\mathrm{nm}$ excitation and emission filter set was suitable for FITC fluorescence imaging based on the absorption and emission spectra of FITC (Figure 6.1).

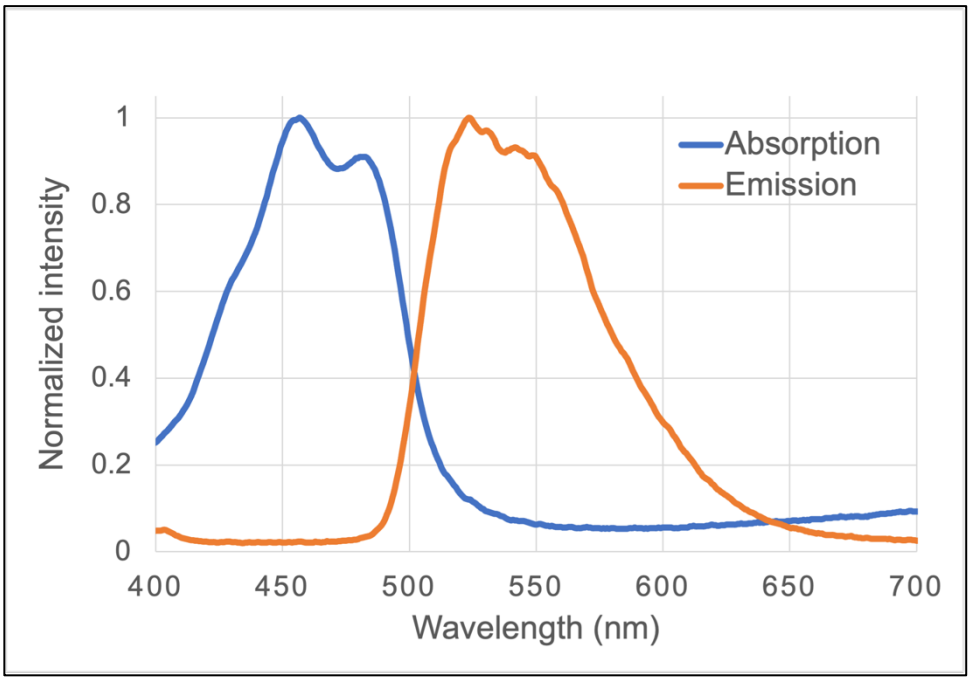

Figure 6.1: Excitation and emission spectra of FITC.

But first we checked the viability of surface functionalization with Rhodamine B on $50\,\mathrm{mm}$ long cleaved optical fibers as well as on NSOM probes made from $70\,\mathrm{mm}$ long optical fibers. Rhodamine B functionalized cleaved optical fibers and NSOM probes were

excited with 514 nm wavelength laser light because the 514 nm excitation and emission filter set was suitable for Rhodamine B fluorescence imaging based on the absorption and emission spectra of Rhodamine B (Figure 6.2).

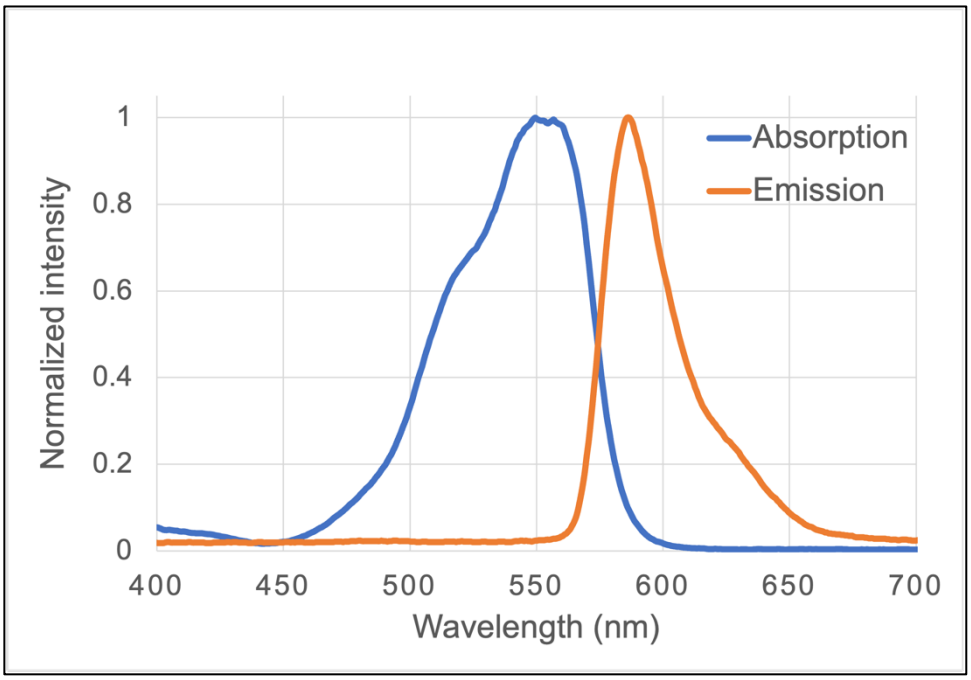

Figure 6.2: Excitation and emission spectra of Rhodamine B.

The functionalization process of the surface of NSOM probes or cleaved optical fibers has three steps: (a) surface cleaning, (b) silanization, and (c) fluorophore attachment (methods discussed in Chapter 3). Surface cleaning removes impurities from the surface and activates the hydroxyl groups on the surface. In the silanization step, a covalent bond is formed between the surface and the APTES which has an amine terminal group. The fluorophore attachment step is a one-step reaction to form a covalent bond between the amine group of the APTES and a functional group of the fluorescent molecule.

We functionalized the cleaved end of a cleaved optical fiber with Rhodamine B by the functionalization method mentioned in Chapter 3 and put it vertically under the optical microscope so that the flat surface of the cleaved end faced the microscope objective, and the halogen light source illuminated its back side. The flat surface appeared as a dark circle when imaged in brightfield mode (Figure 6.3(a)) but exhibited considerable fluorescence activity when excited with $514\ \mathrm{nm}$ wavelength laser light through the microscope objective, suggesting that the surface was successfully functionalized with Rhodamine B (Figure 6.3(b)). On the other hand, a non-functionalized cleaved optical fiber did not show such fluorescence behavior when excited with laser light (Figure 6.3(c)).

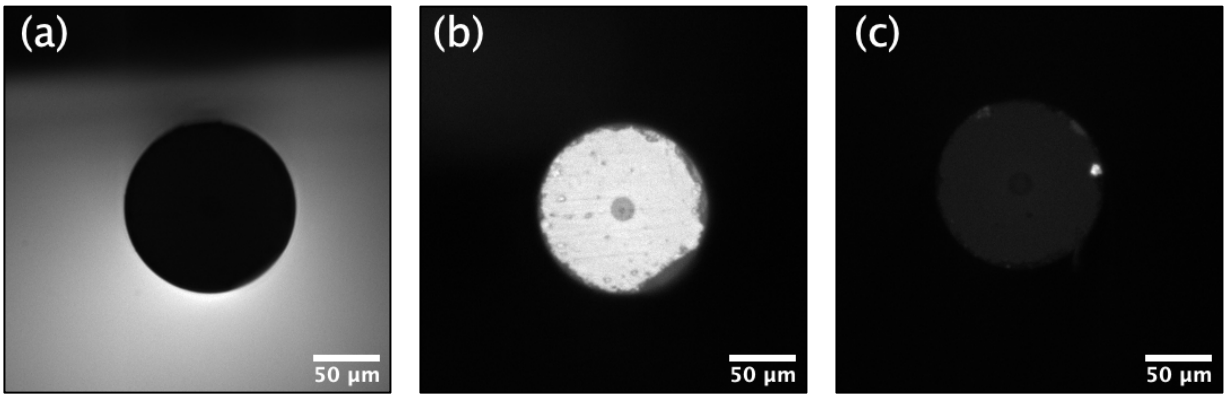

Figure 6.3: Image of the top view of cleaved optical fibers captured (a) in brightfield mode and (b) in fluorescence mode with Rhodamine B functionalization, and (c) in fluorescence mode without Rhodamine B functionalization.

Next, we functionalized an NSOM probe with Rhodamine B utilizing the same functionalization method. In this case, the probe was mounted horizontally and imaged from the side in both brightfield mode and fluorescence mode using the same setup for $514\ \mathrm{nm}$ laser excitation as before (Figure 6.4).

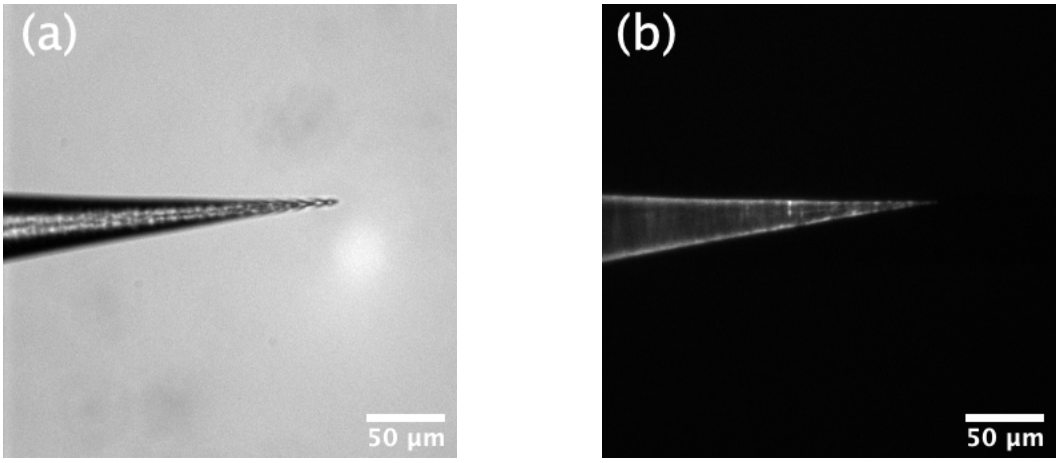

Figure 6.4: Image of the side view of Rhodamine B functionalized NSOM probe captured (a) in brightfield mode and (b) in fluorescence mode.

The fluorescence mode image shows that the walls of the cone are functionalized with Rhodamine B, but it was especially important to know whether any Rhodamine B attachment was successful at the apex of the probe. Therefore, we imaged the apex of the probe head-on (pointing towards the microscope objective) in brightfield mode as well as in fluorescence mode with $514\ \mathrm{nm}$ laser excitation through the microscope objective (Figure 6.5). In brightfield mode, the apex appears as a barely visible, tiny dark spot (marked by the red arrow in Figure 6.5(a)), while it shows significant fluorescence activity in fluorescence mode (Figure 6.5(b)).

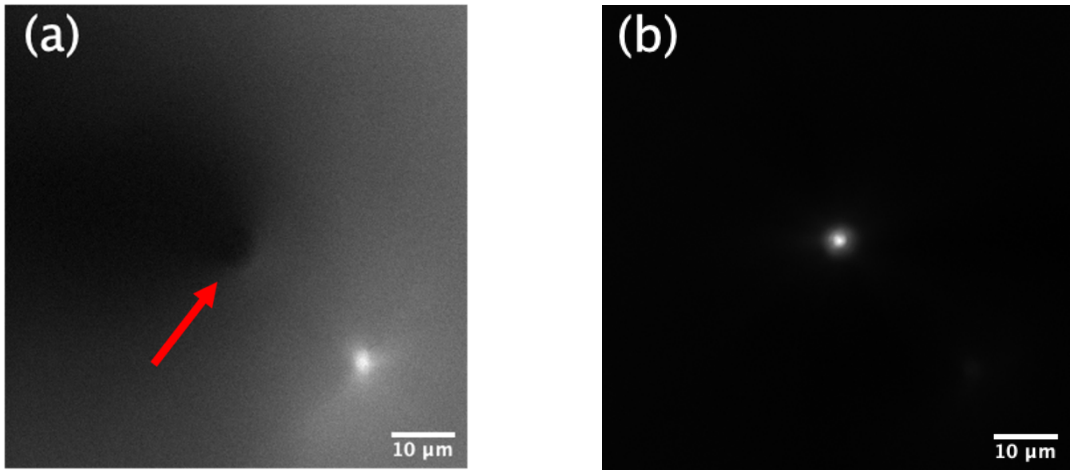

Figure 6.5: Image of the top view of Rhodamine B functionalized NSOM probe captured (a) in brightfield mode and (b) in fluorescence mode. Left image has a bright spot at the bottom right that is an image artifact caused by a crack in the halogen lamp.

FITC functionalization of the NSOM probe end of the $1\ \mathrm{m}$ long optical fiber was performed according to the method described in Chapter 3. After functionalization, laser light of wavelength $488\ \mathrm{nm}$ was coupled into the cleaved end of the nanosensor probe and the FITC functionalized NSOM probe end was placed under the microscope. The brightfield and fluorescence images of the tapered probe were both taken under laser excitation (Figure 6.6) and demonstrate that only the apex shows substantial fluorescence activity in both brightfield and fluorescence mode.

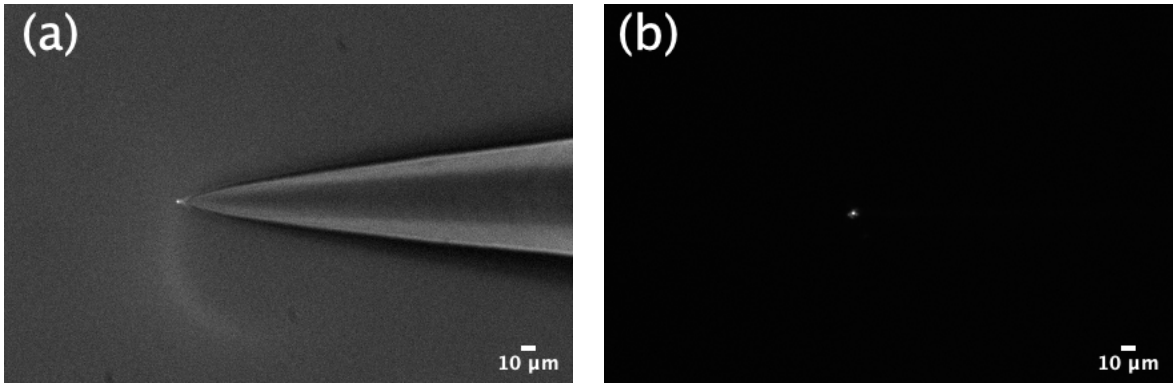

Figure 6.6: Image of the side view of FITC functionalized NSOM probe captured (a) in brightfield mode and (b) in fluorescence mode.

6.3 Quantifying Spot Intensity in Image

In the case of the fluorescent nanosensor, the intensity of the fluorescence depends on the chemical interaction between the fluorescent molecules on the nanosensor with the sample molecules. The fluorescence intensity can increase with increasing concentration for some samples or decrease with increasing concentration for other samples. Therefore, quantifying the intensity of the very tiny, bright fluorescent spot (Figure 6.6(b)) from the captured image is vital.

The EMCCD camera used with the optical microscope has a square-sized sensor with 512 pixels on each side. Each pixel has a length of $0.8396\ \mu\mathrm{m}$ when images are captured with the $10\mathrm{x}$ microscope objective, which is significantly larger than the diameter of the apex of the probe. Due to diffraction, however, the fluorescent light emitted from the apex is distributed over several pixels following (approximately) a Gaussian distribution of intensity. Given that consistent focusing is hard to achieve, we should therefore not just consider the value of the highest intensity pixel when using the

nanosensor for sensing application, but rather, find the integrated intensity of the contributing pixels when comparing the change in fluorescence intensity with change in concentration.

Once more, MATLAB was utilized to find the integrated intensity from the images captured in the fluorescence mode using custom-written code instead of using a MATLAB toolbox. In this MATLAB code, the brightest pixel on the image is located, and pixels within cutoff distances between 1 pixel and 100 pixels from the brightest pixel are summed into a value for the integrated intensity. Before summation, however, the mean intensity of all other pixels is subtracted from the intensity values of the contributing pixels to yield background-free integrated intensity values. Lastly, these integrated intensities are tabulated as a function of their corresponding cutoff distances in order to select the most accurate integration method.

6.4 Experimental Results

In the sensing experiments with the nanosensor, laser light of wavelength $488\ \mathrm{nm}$ was coupled into the cleaved end of the nanosensor probe and the tip of the FITC functionalized NSOM probe was immersed completely in drops of sample solutions. First, we conducted experiments to detect change in pH with different drops of known pH solutions using the nanosensor. Then we ran experiments on detecting the change in the concentration of Cu^{2+} ions as well as Fe^{3+} ions with different drops of known concentrations of the ion solutions. We rinsed the nanosensor probe with ultrapure water between each use of the sample solution drops during the detection experiments. Next,

integrated intensities were calculated from the captured images in fluorescence mode and plotted on a graph.

6.4.1 pH Detection

The different pH solutions that were used in the pH detection experiments using the nanosensor had pH values of 3, 5, 7, 9, and 11, where pH 7 solution was just ultrapure water. The fluorescence activities of the FITC functionalized nanosensor probe at different pH solutions was captured with the microscope camera. The captured images did not exhibit a significant intensity change as shown in Figure 6.7.

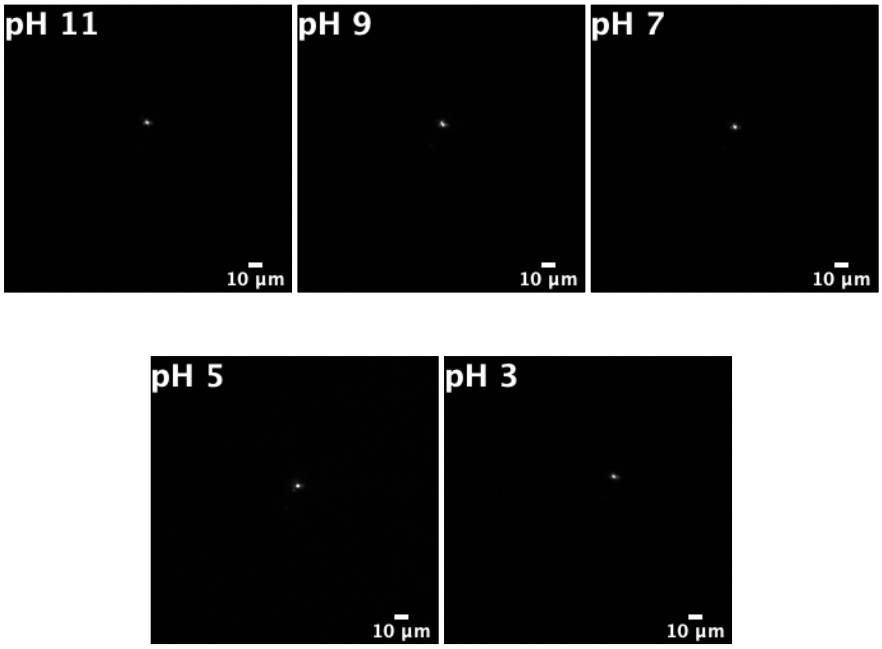

Figure 6.7: Images of the fluorescing nanosensor probe immersed in the drops of different pH solutions captured in fluorescence mode.

To ascertain the fluorescence intensities in different pH solutions, we ran the MATLAB function "*integInten*" on these images to obtain the integrated intensities for various cutoff distances. We identified that a cutoff distance of 20 pixels was ideal because background noise was added to the integrated intensities with higher cutoff distances and actual intensities were lost in the integrated intensities with lower cutoff distances. When the logs of the integrated intensities were plotted against the pH values as shown in Figure 6.8, the plot did not show a definitive trend in the fluorescence intensity change of FITC with change in the pH values, but rather showed some irregularities.

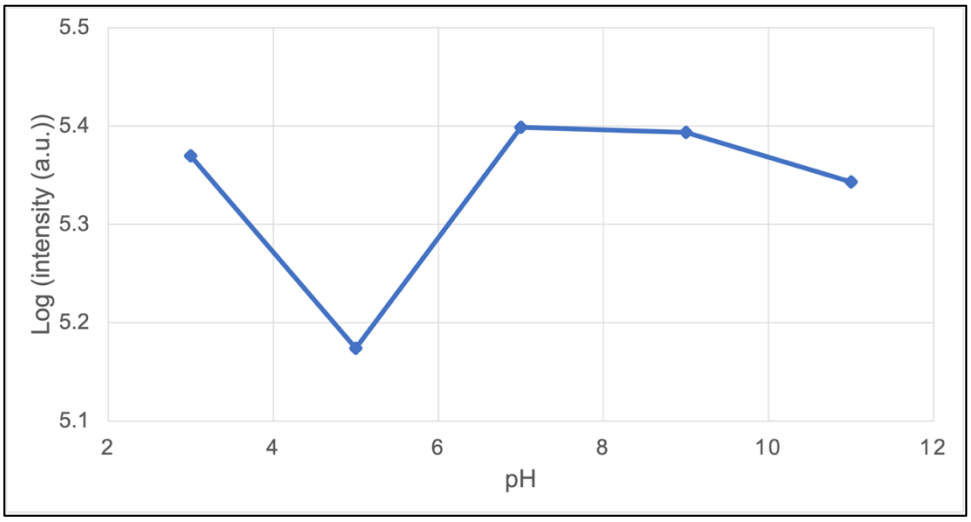

Figure 6.8: Variation of integrated intensity of FITC on the nanosensor probe as a function of pH.

We prepared several FITC solutions with pH of the solutions having values of 4, 7, and 10 and measured the relative fluorescence intensities of the solutions with the fluorescence spectrometer having excitation wavelength at $500\,\mathrm{nm}$. The peak fluorescence intensity of each solution was taken and plotted against the pH values of the solutions (Figure 6.9). The plot showed an increasing trend of fluorescence intensities

with increasing pH values. This trend was supposed to be seen in the pH detection experiment with the nanosensor.

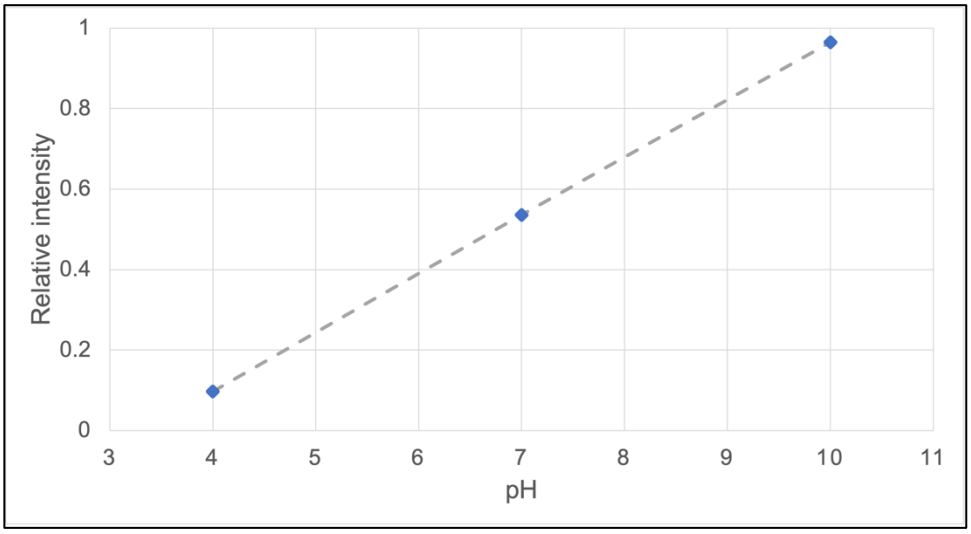

Figure 6.9: Variation of relative intensity of FITC in solution as a function of pH.

6.4.2 Cu^{2+} Ion Detection

In the Cu^{2+} ion detection experiments with the nanosensor, $0.001\ M$, $0.01\ M$, $0.1\ M$, and $1\ M$ $CuSO_4$ solutions were used. Images of the fluorescence activities of the FITC functionalized nanosensor probe were taken for the different Cu^{2+} ion concentrations. The intensity of the bright fluorescence spot on the images dropped slightly with increased concentration (Figure 6.10).

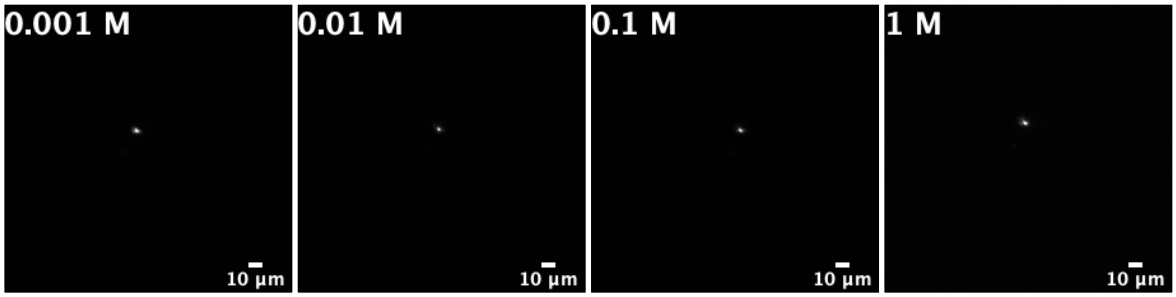

Figure 6.10: Images of the fluorescing nanosensor probe immersed in the drops of $CuSO_4$ solutions having different concentrations captured in fluorescence mode.

Integrated intensities were calculated by running the MATLAB function "*integInten*" on these images. When the logs of the integrated intensities calculated with a cutoff distance of 20 pixels from the brightest intensity pixel were plotted against the logs of Cu^{2+} ion concentrations, the intensities decreased with increasing concentration (Figure 6.11).

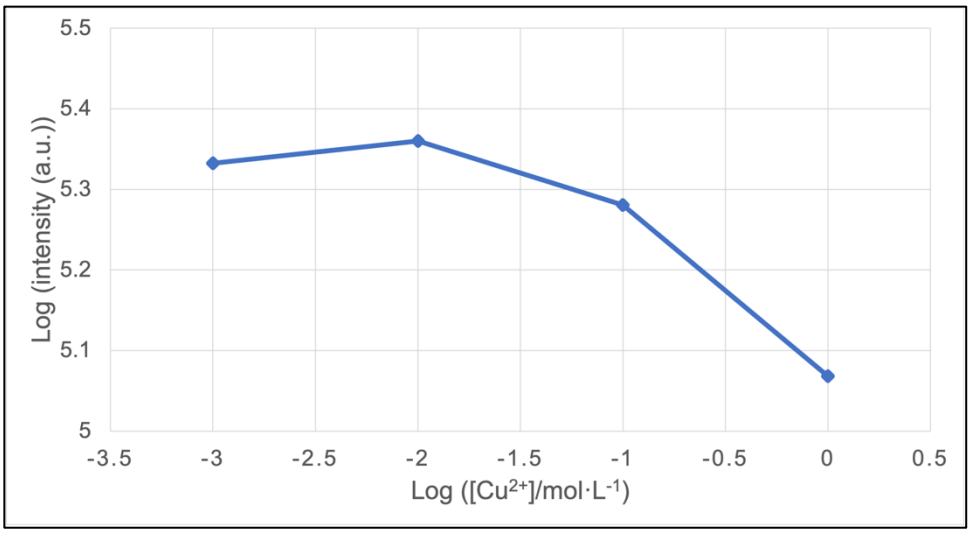

Figure 6.11: Variation of integrated intensity of FITC on the nanosensor probe as a function of $CuSO_4$ concentration.

We added $200\ \mu L$ of prepared FITC stock solution to each of the 4 cuvettes containing $2.5\ mL$ of ultrapure water and mixed them thoroughly. The FITC solution in each cuvette showed approximately the same relative fluorescence intensities. Then we added $100\ \mu L$ of prepared $0.001\ M$, $0.01\ M$, $0.1\ M$, and $1\ M$ $CuSO_4$ solutions to respective cuvette and mixed them thoroughly. Afterwards, we measured the relative fluorescence intensities of the solutions with the fluorescence spectrometer having excitation wavelength at $500\ nm$. The peak fluorescence intensity of each solution was taken and plotted against the logs of Cu^{2+} ion concentrations of the solutions (Figure 6.12). The plot showed a decreasing trend of fluorescence intensities with increasing concentration. This trend was also seen in the Cu^{2+} ion detection experiment with the nanosensor which meant the nanosensor appropriately detected the change in Cu^{2+} ion concentration.

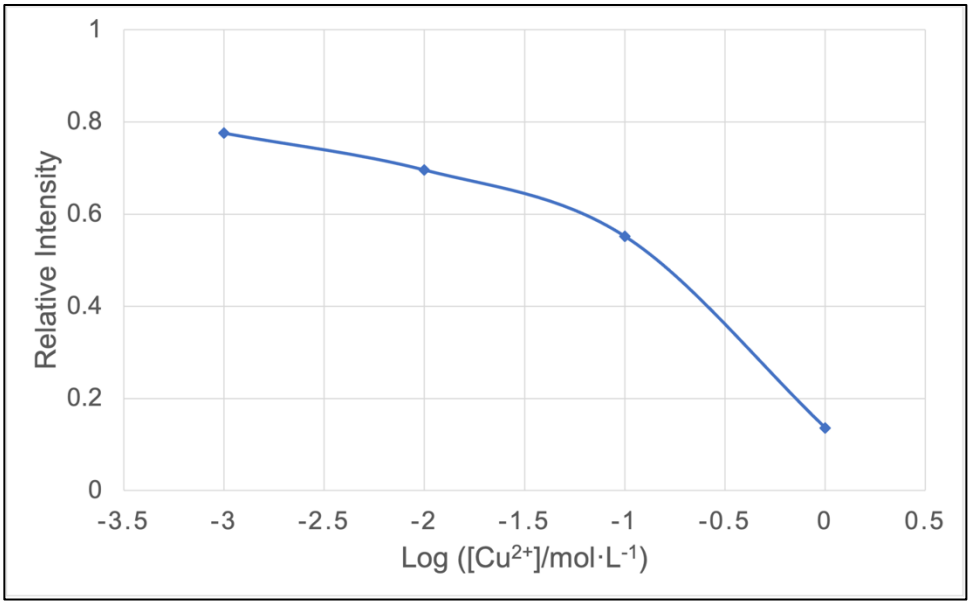

Figure 6.12: Variation of relative intensity of FITC in solution as a function of $CuSO_4$ concentration.

6.4.3 Fe^{3+} Ion Detection

Drops were placed on the microscope coverslip from the prepared $0.00002\ \mathrm{M}$, $0.0002\ \mathrm{M}$, $0.002\ \mathrm{M}$, and $0.2\ \mathrm{M}\ FeCl_3$ solutions in the Fe^{3+} ion detection experiments with the nanosensor. The microscope camera captured the fluorescence activities of the FITC functionalized nanosensor probe for different Fe^{3+} ion concentrations. The captured images show that the intensities of the bright fluorescence spot appeared to decline for higher concentrations (Figure 6.13).

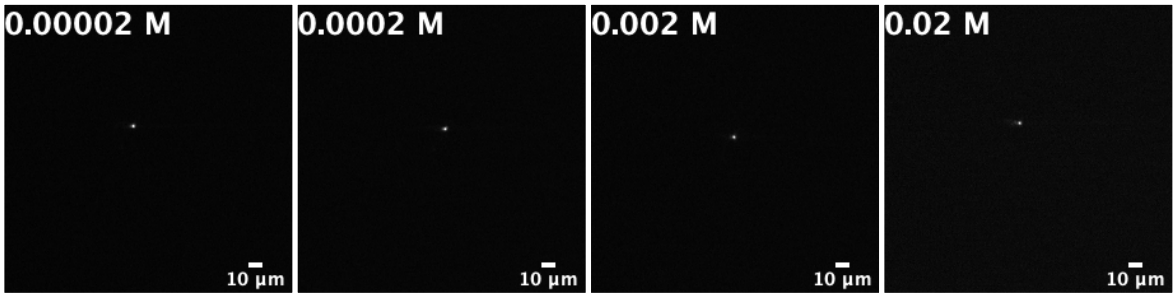

Figure 6.13: Images of the fluorescing nanosensor probe immersed in the drops of $FeCl_3$ solutions having different concentrations captured in fluorescence mode.

With the MATLAB function "*integInten*", integrated intensities were calculated from these images and integrated intensity values found for a cutoff distance of 20 pixels from the brightest intensity pixel were used for plotting the graph. When the logs of these integrated intensity values were plotted against the logs of Fe^{3+} ion concentrations, it was found that the trend showed a decrease in intensities with an increase in Fe^{3+} concentration (Figure 6.14).

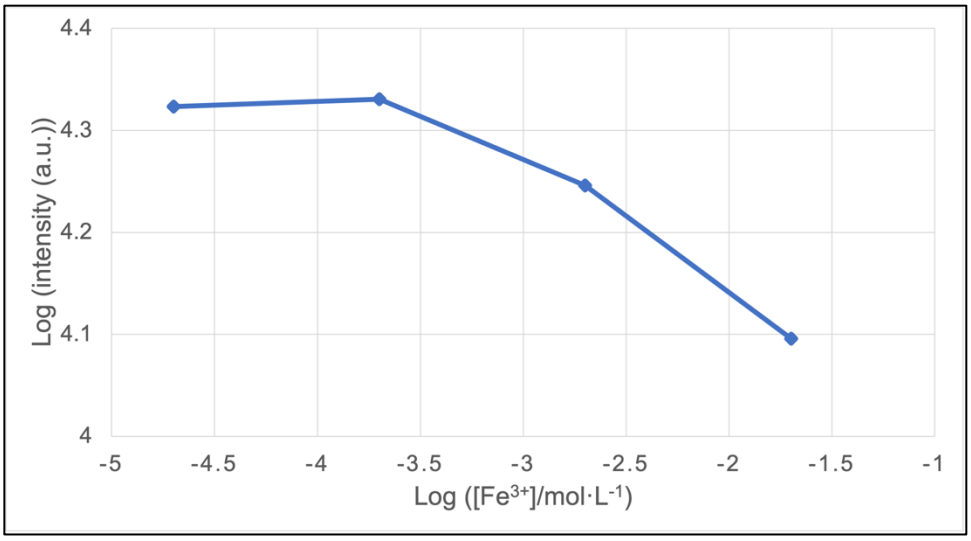

Figure 6.14: Variation of integrated intensity of FITC on the nanosensor probe as a function of $\mathrm{FeCl_3}$ concentration.

$200\ \mu\mathrm{L}$ of prepared FITC stock solution was thoroughly mixed with $2.5\ \mathrm{mL}$ of ultrapure water contained in each of the 3 cuvettes. The FITC solution in each cuvette showed approximately the same relative fluorescence intensities. Then $100\ \mu\mathrm{L}$ of prepared $0.00002\ \mathrm{M}$, $0.0002\ \mathrm{M}$, and $0.002\ \mathrm{M}$ $\mathrm{FeCl_3}$ solutions were thoroughly mixed with FITC solution of the corresponding cuvette. Next, we measured the relative fluorescence intensities of the solutions with the fluorescence spectrometer having excitation wavelength at $500\ \mathrm{nm}$. The peak fluorescence intensity of each solution was taken and plotted against the logs of $\mathrm{Fe^{3+}}$ ion concentrations of the solutions (Figure 6.15). The plot showed a decreasing trend of fluorescence intensities with increasing concentration. This trend was also seen in the $\mathrm{Fe^{3+}}$ ion detection experiment with the nanosensor which signified the nanosensor appropriately detected the change in $\mathrm{Fe^{3+}}$ ion concentration.

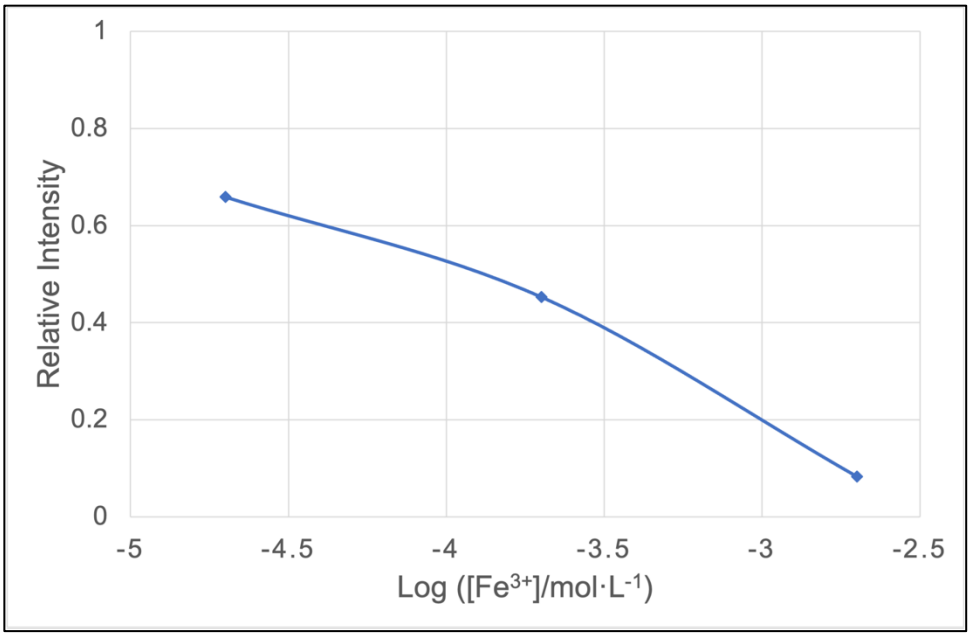

Figure 6.15: Variation of relative intensity of FITC in solution as a function of $\mathrm{FeCl_3}$ concentration.

6.5 Concluding Remarks

The pH detection experiment did not show a gradual increase of the fluorescence intensity with increasing pH, which could be due to fast photobleaching of the FITC molecules at the tip of nanosensor probe in pH solutions. However, both the experiments for detecting $\mathrm{Cu^{2+}}$ and $\mathrm{Fe^{3+}}$ ions using the nanosensor showed a clear trend of decreasing fluorescence intensity with increasing concentration. Metal ions can quench fluorescence, which leads to lower intensity of fluorescence.

References

(1) Javaid, M.; Haleem, A.; Singh, R. P.; Rab, S.; Suman, R. Exploring the Potential of Nanosensors: A Brief Overview. *Sens. Int.* **2021**, *2*, 100130. https://doi.org/10.1016/j.sintl.2021.100130.

(2) Abdel-Karim, R.; Reda, Y.; Abdel-Fattah, A. Review—Nanostructured Materials-Based Nanosensors. *J. Electrochem. Soc.* **2020**, *167* (3), 037554. https://doi.org/10.1149/1945-7111/ab67aa.

CHAPTER 7

Conclusions

7.1 Summary and Conclusions

The mechanism of the etching of bare SiO_2 structures by HF is not fully understood because many variables that influence the etching process are still unknown. The mechanism becomes even more complex when optical fibers are etched with an intact polymer jacket and a sealed bottom end. The MST etching experiments for fabricating NSOM probes uncovered some new information about the etching process of optical fibers that has not been published in any previous literature. In the case of the etching of optical fibers, most literature suggested that the variation of cone angles with etching time would follow an exponential plateau curve. Rather, it was found with the MST etching experiments that the variation of cone angles over time looks more like a damped oscillating curve. We suggest that the Shrinking Core Model (SCM) is a possible mechanism for the etching process of optical fibers. A multiphysics simulation in COMSOL® was developed for the etching of optical fibers based on the suggested mechanism. The simulation gave results for the variation of cone angles with etching time that were comparable to that of the MST etching experiments, which therefore supports our proposed mechanism for the etching process.

Many articles suggest that the initial tip is formed above the top interface of the bulk HF inside the polymer jacket with the sealed-tube etching method. However, our MST etching experiments revealed that the initial tip was in fact formed below the top interface of the bulk HF inside the polymer jacket tube. There is a likelihood that the wicking inside the polymer jacket plays a role in the sealed-tube etching process of optical fibers and that the height of the wicking liquid front may rise with increasing etching time.

This assumption is based on the observation that continued etching of optical fibers was spotted beyond the maximum height of wicking found by a wicking simulation in COMSOL®.

On a related note, the NSOM probes were functionalized with FITC to develop a fluorescent nanosensor. The nanosensor was successful in detecting the change in different metal ion concentrations but had difficulty in detecting the change in pH values in a small drop of sample solution. Developing fluorescent nanosensors with a photostable pH sensitive fluorescent molecule instead of FITC could provide better results in detecting pH change in small sample solution drops. The nanosensor experiments indicate that the nanosensor can be used for non-destructive localized sensing in an *in situ* or possibly *in vivo* setup.

7.2 Future Directions

For the future, we expect this research to continue to advance the ongoing work and to explore new avenues of study. NSOM probes are usually fabricated from conventional single-mode optical fibers. Photonic Crystal Fibers (PCF) are optical fibers based on the properties of photonic crystals. PCFs have very tiny and closely spaced air holes which go through the whole length of the fiber. This allows PCFs to confine light in hollow cores or to have confinement characteristics not possible with conventional optical fibers. Therefore, PCFs can provide single-mode guidance over very wide wavelength regions (UV to IR), have exceptionally high nonlinearity, and feature numerical apertures

(NA) ranging from very low to very high (about 0.9). Due to these unique advantages, fabricating NSOM probes from photonic crystal fibers is a direction for future research.

However, the COMSOL® simulation model that was developed to simulate MST etching was based on the etching of conventional optical fibers with the assumption of a first-order reaction kinetics. In the simulation model, deformation of the boundaries was determined by a normal velocity calculated using the overall reaction equation of SiO_2 etching by HF, and the polymer jacket in the model was not defined using "*Porous Media*" module. All these assumptions were made to simplify the model and avoid too many complexities for the simulation. Future work will include developing an etching simulation model incorporating the deformation of the boundaries from the product formation by the actual reaction kinetics and the addition of porous media properties for the polymer jacket.

Lastly, after achieving the initial goal of developing a nanosensor, the next step will be enhancing the nanosensor for usage in a new field of sensing applications. Therefore, future study includes determining dissolved O_2 concentration in water using a nanosensor, which is developed by attaching metal nanoparticles to NSOM probes that are modified with sensor molecules and are separated by a dielectric spacer layer.

Appendix

Cone Angle Dataset

Dataset containing 26 datapoints of cone angles with their corresponding etching times described in Chapter 4.

Table A: Cone angles with their corresponding etching times of all NSOM probes fabricated using MST etching method.

Etching Time (min)	Cone Angle (°)
160	7.8
180	12.9
210	20.8
225	19.2
232.5	21.7
240	23.3
247.5	20.2
255	20.6
270	21.0
300	21.7
330	19.2
360	17.9
375	16.6
390	19.5
405	14.1
420	18.9
450	19.7
465	16.5
480	23.4
495	15.2
510	18.1
540	16.1
570	15.3
600	17.4
660	15.9
720	15.4

Muhmmad Nazmul Hussain

University of Wisconsin-Milwaukee
Department of Chemistry and Biochemistry
3210 N Cramer St
Milwaukee, WI 53211
Email: hussain4@uwm.edu

Education

University of Wisconsin-Milwaukee, Milwaukee, WI
PhD in Physical Chemistry and Nanotechnology
Areas of Concentration or Major: Physical Chemistry
Dissertation/Thesis: “Study of the Chemical Fabrication Process of NSOM Probes and the Modification of the Probe Surface”

University of Dhaka, Dhaka, Bangladesh
Bachelor of Science (Honors) in Chemistry
Areas of Concentration or Major: Chemistry (BS in Chemistry)

Awards

- UWM Graduate Student Travel Award, Graduate School, University of Wisconsin-Milwaukee, Milwaukee, WI, September 2019
- Moczynski Outstanding Teaching Assistant Award, Chemistry and Biochemistry Department Awards Day, University of Wisconsin-Milwaukee, Milwaukee, WI, April 2014
- UWM Chancellor's Award, Chemistry and Biochemistry Department, University of Wisconsin-Milwaukee, Milwaukee, WI, August 2013 – May 2018

Professional Skills

Technical:

- UV-Visible Spectroscopy
- Infrared Spectroscopy
- Fluorescence Spectroscopy
- Chemical Etching of Optical Fibers
- Nanofabrication
- Atomic Layer Deposition
- Near-field Scanning Optical Microscopy (NSOM)
- Scanning Electron Microscopy (SEM)
- Atomic Force Microscopy (AFM)
- Raman Microscopy
- Fluorescence Microscopy
- High Performance Liquid Chromatography (HPLC)
- Mass Spectrometer
- Nuclear Magnetic Resonance Spectroscopy
- Laser Systems
- Metal Deposition
- Nanosensors

Software:

- COMSOL
- MATLAB
- SOLIDWORKS
- National Instruments LabVIEW
- ImageJ
- Autodesk Fusion 360

Experience

Research:

- Fall 2013 – Present
  Research Assistant
  Department of Chemistry and Biochemistry

University of Wisconsin-Milwaukee

Teaching:

- Spring 2020 – Spring 2022
  Teaching Assistant
  Department of Chemistry and Biochemistry
  University of Wisconsin-Milwaukee
  Course: CHEM 103 (Discussion) – Survey of Biochemistry

- Fall 2019
  Teaching Assistant
  Department of Chemistry and Biochemistry
  University of Wisconsin-Milwaukee
  Course: CHEM 100 (Discussion) – Chemical Science

- Spring 2018 – Spring 2019
  Teaching Assistant
  Department of Chemistry and Biochemistry
  University of Wisconsin-Milwaukee
  Course: CHEM 103 (Discussion) – Survey of Biochemistry

- Fall 2017
  Teaching Assistant
  Department of Chemistry and Biochemistry
  University of Wisconsin-Milwaukee
  Course: CHEM 103 (Lab) – Survey of Biochemistry

- Spring 2017
  Teaching Assistant
  Department of Chemistry and Biochemistry
  University of Wisconsin-Milwaukee
  Course: CHEM 103 (Discussion) – Survey of Biochemistry

- Fall 2016
  Teaching Assistant
  Department of Chemistry and Biochemistry
  University of Wisconsin-Milwaukee
  Course: CHEM 102 (Discussion and Lab) – General Chemistry I

- Summer 2016
  Teaching Assistant
  Department of Chemistry and Biochemistry
  University of Wisconsin-Milwaukee

Course: CHEM 105 (Discussion and Lab) – General Chemistry for Engineering

- Spring 2016
  Chemistry Supplemental Instructor (CSI)
  Department of Chemistry and Biochemistry
  University of Wisconsin-Milwaukee
  Course: CHEM 101 – Chemical Science for Nurses, and CHEM 103 – Survey of Biochemistry

- Fall 2015
  Teaching Assistant
  Department of Chemistry and Biochemistry
  University of Wisconsin-Milwaukee
  Course: CHEM 342 (Lab) – Introductory Organic Chemistry Laboratory

- Summer 2015
  Teaching Assistant
  Department of Chemistry and Biochemistry
  University of Wisconsin-Milwaukee
  Course: CHEM 344 (Lab) –Organic Chemistry Laboratory

- Spring 2015
  Teaching Assistant
  Department of Chemistry and Biochemistry
  University of Wisconsin-Milwaukee
  Course: CHEM 103 (Discussion and Lab) – Survey of Biochemistry

- Fall 2014
  Teaching Assistant
  Department of Chemistry and Biochemistry
  University of Wisconsin-Milwaukee
  Course: CHEM 342 (Lab) – Introductory Organic Chemistry Laboratory

- Summer 2014
  Teaching Assistant
  Department of Chemistry and Biochemistry
  University of Wisconsin-Milwaukee
  Course: CHEM 103 (Discussion and Lab) – Survey of Biochemistry

- Spring 2014
  Teaching Assistant
  Department of Chemistry and Biochemistry
  University of Wisconsin-Milwaukee
  Course: CHEM 100 (Discussion) – Chemical Science

- Fall 2013
  Teaching Assistant
  Department of Chemistry and Biochemistry
  University of Wisconsin-Milwaukee
  Course: CHEM 100 (Discussion) – Chemical Science

International Conferences

Poster Presentations:

- "Simulating Wet Etching of Optical Fiber to Fabricate NSOM Probe", M. N. Hussain, X. S. Udad, J. C. Woehl, COMSOL Conference, October 7-8, 2020
- "Simulating Chemical Etching of Optical Fiber to create NSOM Probe using COMSOL", M. N. Hussain, X. S. Udad, E. C. Edwards, J. C. Woehl, COMSOL Conference, Boston, MA, October 2-4, 2019

National Conferences

Poster Presentations:

- "Time-dependent study of NSOM Probes Forged Chemically and its Surface Functionalization for Sensing Applications", M. N. Hussain, X. S. Udad, E. C. Edwards, J. C. Woehl, SciX Conference, Palm Springs, CA, October 13-18, 2019

Regional Conferences

Poster Presentations:

- "Study of the Chemical Fabrication Process of NSOM Probes and the Modification of its Surface for Sensing Applications", M. N. Hussain, X. S. Udad, E. C. Edwards, J. C. Woehl, ACS Great Lakes Regional Meeting, Lisle, IL, May 1-4, 2019

Departmental Symposiums

Poster Presentations:

- "Study of the Chemical Fabrication Process of NSOM Probes and the Modification of its Surface for Sensing Applications", M. N. Hussain, J. C. Woehl, Chemistry and Biochemistry Department Awards Day, University of Wisconsin-Milwaukee, Milwaukee, WI, April 26, 2019
- "Study of the Chemical Fabrication Process of NSOM Probe and the Modification of its Surface", M. N. Hussain, J. C. Woehl, Chemistry and Biochemistry Department Awards Day, University of Wisconsin-Milwaukee, Milwaukee, WI, May 22, 2018

Services & Activities

- Wisconsin Science Olympiad, **Event Supervisor** (Division C), hosted by UW-M, April 2017 & April 2018
- UW-M Chemistry and Biochemistry Graduate Student Council, **Officer**, August 2015 – July 2017
- **Mentor** for new teaching assistants in the Department of Chemistry and Biochemistry, Fall 2014, Fall 2015, and Fall 2016
- **Volunteer** for UW-M Fall Welcome events, Fall 2014, Fall 2015, and Fall 2016